

UNIVERSIDADE DE SÃO PAULO
ESCOLA DE ENGENHARIA DE LORENA

LEONARDO SHOJI AOTA

Microstructure of AISI 316L austenitic stainless steel processed by laser powder-bed fusion with different scanning strategies and its evolution upon annealing and thermomechanical processing

Microestrutura do aço inoxidável austenítico 316L processado via fusão a *laser* em leito de pó com diferentes estratégias de escaneamento e a sua evolução após recozimento e processamento termomecânico

Lorena

2021

LEONARDO SHOJI AOTA

Microstructure of AISI 316L austenitic stainless steel processed by laser powder-bed fusion with different scanning strategies and its evolution upon annealing and thermomechanical processing

Dissertation presented to the Escola de Engenharia de Lorena of Universidade de São Paulo to obtain the title of Master of Science from the Programa de Pós-Graduação em Engenharia de Materiais in the field of Advanced and Conventional Materials.

Advisor: Prof. Dr. Hugo R. Z. Sandim

Revised version

Lorena

2021

NÃO AUTORIZO A REPRODUÇÃO E DIVULGAÇÃO TOTAL OU PARCIAL DESTE TRABALHO, POR QUALQUER MEIO CONVENCIONAL OU ELETRÔNICO, SERÁ DISPONIBILIZADO AUTOMATICAMENTE APÓS 2 ANOS DA PUBLICAÇÃO

Ficha catalográfica elaborada pelo Sistema Automatizado
da Escola de Engenharia de Lorena,
com os dados fornecidos pelo(a) autor(a)

Aota, Leonardo Shoji
Microstructure of AISI 316L austenitic stainless steel processed by laser powder-bed fusion with different scanning strategies and its evolution upon annealing and thermomechanical processing / Leonardo Shoji Aota; orientador Hugo Ricardo Zschommler Sandim - Versão Corrigida. - Lorena, 2021.
140 p.

Dissertação (Mestrado em Ciências - Programa de Pós Graduação em Engenharia de Materiais na Área de Materiais Convencionais e Avançados) - Escola de Engenharia de Lorena da Universidade de São Paulo.
2021

1. Additive manufacturing. 2. Recrystallization. 3. Microstructural evolution. 4. Plastic deformation. 5. Aisi 316l austenitic stainless steel. I. Título. II. Sandim, Hugo Ricardo Zschommler, orient.

LEONARDO SHOJI AOTA

Microestrutura do aço inoxidável austenítico 316L processado via fusão a *laser* em leito de pó com diferentes estratégias de escaneamento e a sua evolução após recozimento e processamento termomecânico

Dissertação apresentada a Escola de Engenharia de Lorena da Universidade de São Paulo para a obtenção do título de Mestre em Ciências do Programa de Pós-Graduação em Engenharia de Materiais na área de Materiais Convencionais e Avançados.

Orientador: Prof. Dr. Hugo R. Z. Sandim

Versão Corrigida

Lorena

2021

NÃO AUTORIZO A REPRODUÇÃO E DIVULGAÇÃO TOTAL OU PARCIAL DESTE TRABALHO, POR QUALQUER MEIO CONVENCIONAL OU ELETRÔNICO, SERÁ DISPONIBILIZADO AUTOMATICAMENTE APÓS 2 ANOS DA PUBLICAÇÃO

Ficha catalográfica elaborada pelo Sistema Automatizado
da Escola de Engenharia de Lorena,
com os dados fornecidos pelo(a) autor(a)

Aota, Leonardo Shoji
Microstructure of AISI 316L austenitic stainless steel processed by laser powder-bed fusion with different scanning strategies and its evolution upon annealing and thermomechanical processing / Leonardo Shoji Aota; orientador Hugo Ricardo Zschommler Sandim - Versão Corrigida. - Lorena, 2021.
140 p.

Dissertação (Mestrado em Ciências - Programa de Pós Graduação em Engenharia de Materiais na Área de Materiais Convencionais e Avançados) - Escola de Engenharia de Lorena da Universidade de São Paulo.
2021

1. Additive manufacturing. 2. Recrystallization. 3. Microstructural evolution. 4. Plastic deformation. 5. Aisi 316l austenitic stainless steel. I. Título. II. Sandim, Hugo Ricardo Zschommler, orient.

To all educators and researchers for their effort in providing knowledge and, consequently, changing the World into a better place.

Acknowledgments

To FAPESP for the financial support provided through both the Master (Grant 2018/23582-9) and Research Internship Abroad (Grant 2019/19942-0) scholarships;

To Prof. Dr. Hugo Ricardo Zschommler Sandim for the valuable discussions and academic orientations throughout this work;

To Prof. Dr.-Ing. habil. Dierk Raabe from Max-Planck-Institut für Eisenforschung (MPIE) for the opportunity of performing a research internship and for the valuable discussions and advices during my stay;

To Prof. Dr. Kahl Dick Zilnyk for the valuable discussions and advices, as well as for the aid in obtaining scanning electron microscopy images at the Instituto Tecnológico Aeronáutico (ITA);

To Dr. Isnaldi Rodrigues de Souza Filho (MPIE) for the valuable discussions, as well as for the support during my stay at the MPIE, and for the initial EBSD measurement and ECCI images;

To Dr. Cauê Corrêa da Silva for the kind help in performing extra EBSD measurements and for the support during my stay at the MPIE;

To Monika Nellessen, Katja Angenendt, Christian Bross and Heidi Bögershausen for their kind assistance in metallography- and scanning electron microscopy-related techniques at MPIE;

To Prof. Dr. rer. nat Eric Aime Jäggle (MPIE) and Dr. Priyanshu Bajaj (MPIE) for processing the material used in this study;

To Dr. Zhongji Sun, Dr. Supriya Nandy, and Dr. Stefan Zaefferer for their kind help in performing cross correlation (CC-EBSD) measurements and ECCI images;

To Prof. Dr. Haroldo Cavalcanti Pinto (EESC-USP), Dr. Alberto Cury Nassour (EESC-USP) and Dr. Benjamin Breitbach (MPIE) for their kind help on XRD and residual stresses measurements;

To PPGEM and EEL-USP employees for their support during my studies and the experimental measurements;

To Mr. Ronildson Monteiro da Aparam South América (Timóteo – MG) for providing the chemical composition analyses in this material;

To my family and friends for their unconditional support.

*“Educar é crescer. E crescer é viver.
Educação é, assim, vida no sentido mais
autêntico da palavra.”*

Anísio Teixeira

ABSTRACT

AOTA, L. S. Microstructure of AISI 316L austenitic stainless steel processed by laser powder-bed fusion with different scanning strategies and its evolution upon annealing and thermomechanical processing. 2021. 140 p. Dissertation (Master of Science) – Escola de Engenharia de Lorena, Universidade de São Paulo, Lorena, 2021.

Metallic materials processed by laser powder-bed fusion (LPBF) have unique microstructures inherited from out-of-equilibrium solidification and complex thermal history. This work reports the possibility of changing the microstructure during LPBF and post-processing of 316L stainless steel. By controlling the process parameters, namely the scanning strategy, we demonstrate the possibility of creating patterned microstructures in this steel. Changing the scanning strategy also affects the residual stresses as well as the defect substructure caused by the high cooling rates. We explore the microstructure/residual stresses relationship to find alternatives to reduce the residual stresses by controlling the microstructure. Upon post-processing annealing, recrystallization nucleation occurs in a non-uniform manner throughout the patterned microstructure, allowing for a linear grain impingement in its early stages, as revealed by applying the microstructural path method (MPM). The active recrystallization mechanisms are revealed and their influence on the non-homogeneous nucleation and recrystallization kinetics is discussed, as well as the possibility of creating engineered microstructures by LPBF processing. Recrystallization nuclei number density is the main factor responsible for the difference in the recrystallization kinetics between different scanning strategies, while particle pinning is responsible for a sluggish kinetics in both cases. The unique microstructures produced by LPBF were cold rolled down to $\epsilon = 1$, resulting in intense twinning and shear banding. The latter is unusual for such strain in wrought-processed austenitic stainless steels. Upon annealing, the cold-rolled samples show abnormal grain growth, while this phenomenon is absent when annealing is applied directly after LPBF. Abnormal grain growth is triggered by an initial size advantage for $\langle 110 \rangle \parallel \text{ND}$ grains along particle-depleted regions. These findings allow us for gaining insight on the control of LPBF-processed microstructures through LPBF-processing and post-processing.

Keywords: Additive manufacturing. Recrystallization. Microstructural evolution. Plastic deformation. AISI 316L austenitic stainless steel.

RESUMO

AOTA, L. S. Microestrutura do aço inoxidável austenítico 316L processado via fusão a laser em leito de pó com diferentes estratégias de escaneamento e a sua evolução após recozimento e processamento termomecânico. 2021. 140 p. Dissertação (Mestrado em Ciências) – Escola de Engenharia de Lorena, Universidade de São Paulo, Lorena, 2021.

Materiais metálicos processados por fusão a laser em leito de pó (LPBF) possuem microestruturas únicas obtidas pela rápida solidificação e história térmica complexa. Este trabalho reporta a possibilidade de mudar a microestrutura durante LPBF e pós-processamento de um aço inoxidável 316L. Controlando a estratégia de escaneamento, demonstramos a possibilidade de criar microestruturas padronizadas neste aço. A estratégia de escaneamento altera as tensões residuais e a subestrutura de defeitos causadas pelas altas taxas de resfriamento. Nós exploramos a relação entre microestrutura e tensões residuais a fim de encontrar alternativas de reduzir as tensões residuais por meio do controle microestrutural na condição como processado. Após recozimento, a nucleação da recristalização ocorre de maneira não uniforme ao longo da microestrutura padronizada, obtendo-se um *clusters* lineares de grão recristalizados durante os primeiros momentos, como demonstrado pelo método do caminho microestrutural (MPM). Os mecanismos de recristalização são revelados e a sua influência na nucleação não uniforme e na cinética de recristalização são discutidos, assim como a possibilidade de criar microestruturas engenheiradas por LPBF. A densidade superficial de grãos recristalizados é o principal fator responsável pela diferença na cinética de recristalização entre diferentes estratégias de escaneamento, enquanto o travamento de contornos por partículas é responsável pela cinética lenta de recristalização em ambos os casos. A microestrutura única produzida por LPBF foi submetida a laminação a frio ($\epsilon = 1$), resultando em intensa formação de maclas de deformação e bandas de cisalhamento. Durante o recozimento, as amostras laminadas a frio mostram crescimento anormal de grãos, provocado por uma vantagem inicial de tamanho de grãos $\langle 110 \rangle$ || ND em regiões pobres em partículas. Estes achados permitem o desenvolvimento no controle de microestruturas processadas por LPBF.

Palavras-chave: Manufatura aditiva. Recristalização. Evolução microestrutural. Deformação plástica. Aço inoxidável austenítico AISI 316L.

LIST OF FIGURES

Figure 1 – Feedstock addition possibilities in additive manufacturing.	28
Figure 2 – Different additive manufacturing methods based on laser beam consolidation.	29
Figure 3 – (a) Satellite particles on a particle surface. (b) Oxide layer and chemical heterogeneity in a recycled powder. (c) Graphic representation of magnetic particle clustering. All these factors harm the use of recycled powders.....	34
Figure 4 – Illustration of liquid flow forming inner pores in simulations. The red line represents the melting point of the material. Above this line, the material is found in the liquid state, while below it the material is found in the solid state.....	36
Figure 5 – Inert gas flow simulation, indicated by arrows and their velocity, as shown by the lateral color scale, and the laser plume flow, indicated by the background colors and their velocity, based on the bottom color scale.	37
Figure 6 – Main process parameters in laser powder-bed fusion.	38
Figure 7 – (a) Molten pools in AISI 316L steel. (b) Epitaxial grains between molten pools and the cellular structured highlighted in the inset. (c) Cellular structure observed by TEM. (d) Nanometric oxides observed by TEM (transmission electron microscopy).....	40
Figure 8 – Difference between solidification and dislocation cells. In (a), dislocation cells are found in the interior of solidification cells. Chromium segregation is visible at solidification cell walls. In (b), dislocation cells and molybdenum segregation at cell boundaries are visible and coincident.	41
Figure 9 – Molten pool shape effect on the grain orientation for (a) low volumetric energy density and (b) high volumetric energy density. CLM: crystallographic lamellar microstructure.	44
Figure 10 – Residual stresses formation mechanisms: (a) thermal gradient mechanism and (b) cooling down mechanism.	46
Figure 11 – Dislocation boundaries formed upon straining up to (a) low-to-moderate strains and (b) large strains.....	49
Figure 12 – (a) Dislocation slip along bands (40% cold-rolling reduction) and (b) mechanical twinning (60% cold-rolling reduction) upon deformation in an AISI 316L steel.	51

Figure 13 – (a) Shear bands in AISI 316L in a coarser scale and (b) different subgrain morphologies developed in the center and along regions near the shear band boundary.....	52
Figure 14 – Abnormal grain growth in AISI 370 austenitic stainless steel annealed at 1130°C for 30 min.....	55
Figure 15 – Microstructural evolution in AISI 316L processed by laser powder-bed fusion at 1200°C for (a) 0 min (as-built), (b) 30 min, (c) 1 h and (d) 2 h. The pole figure direction is [110].....	56
Figure 16 – (a) and (b) Scanning electron microscopy images from the powder batch used for processing samples.	58
Figure 17 – (a) AconityMINI laser powder-bed fusion machine used for processing the parts and (b) computer, with an operational software coupled to the machine.	59
Figure 18 – (a) Employed scanning strategies, namely 0R and 90R. (b) Processing routine for the annealed samples and for cold-rolled and annealed samples. Both sets of samples were obtained from the middle section of a LPBF AISI 316L stainless steel.....	59
Figure 19 – (a) Optical microscopy image and (b) image following the application of the threshold function to quantify porosity.....	61
Figure 20 – (a) Unidirectional scan IPF maps for the (a1) SD x TD, (a2) BD x TD and (a3) BD x SD cross sections. Directions on the IPF are parallel to the BD. (b) Kernel average misorientation for the (b1) SD x TD, (b2) BD x TD and (b3) BD x SD cross sections.....	66
Figure 21 – 90°-rotation IPF maps for the (a1) SD x TD and (a2) BD x TD cross sections. Kernel average misorientation maps for the (b1) SD x TD and (b2) BD x TD cross sections. The IPF indicates directions parallel to BD. Only two cross sections were investigated since the lateral BD x TD and BD x SD cross sections are equivalent due to the 90° rotation between layers.....	66
Figure 22 – Pole figures for (a1) all data, (a2) coarse grains and (a3) fine grains in the unidirectional scan. Pole figures for (b1) all data, (b2) coarse grains and (b3) fine grains in the 90°-rotation scan. (1,2,3).....	68
Figure 23 – Differences in dislocation structures in the (a) last consolidated layer and (b) second last consolidated layer for the 90R sample. The building direction is vertical for both images. ρ : dislocation density (m^{-2}).....	69

Figure 24 – ECCI images from the bulk in (a) 0R and (b) 90R samples. (a2) and (b2) show higher magnification images from regions highlighted by rectangles in (a1) and (b1), respectively. Images were taken from SD (parallel to the scale bar) x TD (perpendicular to the scale bar) cross sections. ECCI: electron channeling contrast imaging; SD: scanning direction; TD: transverse direction. White arrows indicate oxides along dislocation cell boundaries. Orange dashed lines indicate dislocation cell boundaries.70

Figure 25 – Total dislocation, GND and SSD density for (a) average values from the specimens, (b) cell interior, (c) cell wall and (d) low angle boundaries. The low angle boundaries dislocation density was estimated based on (MONTEIRO et al., 2020). GND: geometrically necessary dislocations; SSD: statistically stored dislocations; LAB: low angle boundaries.70

Figure 26 – (a) SE image from the etched sample. (b) Highlighted region in (a) along a melt pool boundary, shown by ECCI. (c) Total GND density from the region highlighted by a black rectangle in (b). BD is parallel to the scale bar in all images. The white arrow indicates a LAB, while the dashed white line indicates a dislocation cell boundary. SE: secondary electrons; ECCI: electron channeling contrast imaging; GND: geometrically necessary dislocations. BD: building direction. LAB: low angle boundary.71

Figure 27 – Residual stresses analyzed on the top cross section in the as-built condition and after electropolishing. σ_{SD} : residual stresses along the scanning direction; σ_{TD} : residual stresses along the transverse direction; σ_{45} : shear residual stresses measured at 45° from the scanning or transverse direction; S_{11} and S_{22} : principal stresses. $\Delta\phi$: angle between the S and P systems, i.e., angle between the SD-TD measurement frame and the coordinate system of principal stresses.73

Figure 28 – Total GND density and residual stresses measured by CC-EBSD from the same region shown in Figure 6. BD is parallel to the scale bar. The color scale bar for the GND density and Von Mises stress is shown beside the map. For all others residual stress maps, the larger color scale on the right side is used. GND: geometrically necessary dislocations; CC-EBSD: cross-correlation electron backscatter diffraction; BD: building direction.74

Figure 29 – GND density map and the indicated misorientation profile (dashed in blue) for the 0R specimen in (a) a coarse scale CC-EBSD map with step size of 500 nm and a (b) fine scale CC-EBSD map (step size: 50 nm). These maps were

obtained from the 0R specimen. It shows dislocation cells as incidental dislocation boundaries and LAB as geometrically necessary boundaries due to the cumulative misorientation. GND: geometrically necessary dislocations; CC-EBSD: cross correlation – electron backscatter diffraction; LAB: low angle boundaries. 76

Figure 30 – (a) Solidification cells from the last consolidated layer. (b) Enlarged view in cyan from (a). Note that solidification cell boundaries, highlighted by white arrows, are visible, while dislocation cells are not observed. A few dislocations accumulate at solidification cell walls when only a single layer is consolidated. This non-uniform distribution of SSD aids the formation of dislocation cells upon intrinsic heat treatment (see schematics in Figure 30)..... 78

Figure 31 – Schematics of the dislocation structure evolution in LPBF alloys. (a) Solidification cells show solute segregation and oxide nanoparticles along their walls. (b) The constrained expansion and shrinkage create statistically stored dislocations (SSD) and slightly reduces the residual stresses. (c) Upon intrinsic heat treatment, more SSDs are nucleated and pinned by oxide nanoparticles and solute drag along solidification cell walls, resulting in the coincidence of dislocation and solidification cells. Geometrically necessary dislocations redistribute stresses due to the heterogeneous distribution of SSDs. The nucleation of dislocations and the formation of dislocation cells relieve residual stresses..... 78

Figure 32 – IPF maps for the recrystallized grains in (a) unidirectional and (b) 90° rotation scans for different annealing times at 1150°C. Recrystallized grains are defined here to have a grain orientation spread (GOS) smaller or equal to 2°. The volume fraction of recrystallized grains is also shown. These values are calculated based on the average values from all investigated cross sections (3 for the unidirectional scan and 2 for 90°-rotation). 81

Figure 33 – IPF from the BD x TD cross section for the unidirectional scan at different annealing times (1150°C). 82

Figure 34 – IPF for the BD x SD cross section for the unidirectional scan at different annealing times (1150°C). 82

Figure 35 – IPF for the side cross section for the 90°-rotation sample annealed at 1150°C for different times. 83

Figure 36 – JMAK plot for all cross sections from the unidirectional and 90°-rotation scans. 83

Figure 37 – (a) Grain contiguity, (b) p parameter and (c) q parameter from the microstructural path method indicating the clustering degree in recrystallization nuclei. All data was obtained from 3 different cross sections for the unidirectional scan, while 2 different cross sections were used for the 90° rotation.	84
Figure 38 - Average growth rate from experimental and Cahn-Hagel methods for the (a1) unidirectional scan and (a2) 90°-rotation. Average grain size obtained experimentally and estimated based on the Cahn-Hagel method for the (b1) unidirectional scan and (b2) 90°-rotation.....	85
Figure 39 - (a) Size and volume percentage of oxide particles and (b) Recrystallization grains density for both scanning strategies, unidirectional and 90°-rotation scans. The values from (b) are the average from 3 cross sections for the unidirectional scan, while 2 cross sections were analyzed for the 90°-rotation.	89
Figure 40 - EDS elemental maps from the (a) as-built condition showing Mo segregation. (b) EDS after annealing at 1150°C/15 min showing no signs of elemental segregation in the austenite. (c) Scheil-Gulliver simulation showing the Mo microsegregation profile inside a solidification cell. The schematic representing the solidification cells is given with its size. The red curve in the inset represents the calculated Mo microsegregation profile (d) DICTRA simulation showing the Mo segregation profile after different annealing times at 1150°C.....	90
Figure 41 - Pole figures for the recrystallized grains in the (a) unidirectional scan and (b) 90°-rotation scan.....	92
Figure 42 – Grain boundary character distribution and recrystallized fraction for the (a1) unidirectional scan, (a2) 90°-rotation scan and the grain boundary character distribution considering only the recrystallized partition for the (b1) unidirectional scan and the (b2) 90°-rotation scan.....	93
Figure 43 - (a) Image quality map interposed with boundaries. Red circles indicate regions where twinning occurred to create grains with new mobile boundaries. (b) ECCI from a twinning event from the orange circle in (a) highlighted by an orange circle. (c) Suggested mechanism for recrystallization starting at recovery to SIBM and twinning to create more boundaries with high mobility. In (c), bold blue lines represent less recovered cell walls compared to the thin lines.....	95
Figure 44 - (a) ECCI image showing heterogeneous particle size and spatial distribution; (b) ECCI image showing the alignment of particles (within the red rectangle) due to a boundary decoration. When Zener pinning decreases by particle	

coarsening, the boundary continues to move and leaves behind a well-patterned distribution of previously boundary-pinned particles; (c) Stop-and-go mechanism caused by the pinning and subsequent coarsening of particles (red) until the moving boundary (green) is released. In (c), bold black lines represent thicker cell walls, while thinner black lines represent recovered cell walls. Note the disappearance of finer oxides due to the Ostwald ripening mechanism..... 97

Figure 45 – Inverse pole figure (IPF) from the longitudinal cross section (RD x ND) for the (a1) 0R and (a2) 90R samples. The orientations shown by the IPF are related to the rolling direction (\parallel RD). ODF figures for the (b1) 0R and (b2) 90R samples. 98

Figure 46 - Defect population and substructure created by cold-rolling in LPBF AISI 316L specimens employing the (a) 0R and (b) 90R scanning strategies. Figures A2 and B2 are magnifications from the marked area by red and green in Figure A1 and Figure B1, respectively. Note the intense shearing and twinning..... 99

Figure 47 - (a) Disturbances in the first set of shear bands due to the growth of the second set of shear bands in cold-rolled LPBF AISI 316L stainless steel. (b) Deformation sequence schematics based on the experimental results. (c) Substructure details from the shear bands showing fine lath subgrains and a twinned matrix in between shear bands. Note the change in the oxide shape resulting from shear..... 102

Figure 48 - IPF for the (a1) 63CR-0R and (a2)63CR-90R specimens. Note the presence of abnormal grains, as well as recrystallized and fine grains. ODF for the (b1) 63CR-0R and (b2) 63CR-90R specimens..... 103

Figure 49 – Micrographs showing the spatial distribution of particles and their size difference depending on the microstructural site for the (a) fine grains, (b) recrystallized grains and (c) abnormal grains..... 104

Figure 50 - (a) Average particle size, (b) volume percentage and (c) nearest neighbor distance for the second-phase particles found in (1) fine, (2) recrystallized and (3) abnormal grains. Values from the recrystallized grains were obtained in the vicinity of abnormal grains. 107

Figure 51 - (a) Correlated misorientation angle distribution and (b) uncorrelated misorientation angle distribution for abnormal and matrix grains, as well as for two fiber textures. ODF for the (c) matrix grains and (d) abnormal grains..... 110

Figure 52 – Average grain size for different fiber textures in the (a1) 63CR-0R and (a2) 63CR-90R specimens. Volume fraction of fiber textures for the (b1) 63CR-0R and (b2) 63CR-90R specimens. Only recrystallized grains from the “matrix” were considered, i.e., abnormal and fine grains were not accounted in this quantification.....111

Figure 53 - Abnormal grains from sample (a) 63CR-0R annealed at 1150°C/1 h and (b) 63CR-90R annealed at 1150°C/15 min. The orange squares show regions with low particle density where AGG may have started.....111

Figure 54 - Grain size distribution for the (a1) for fiber textures usually forming abnormal grains. Note the inset showing the presence of a few extremely large $\langle 110 \rangle \parallel$ ND grains. (a2) fiber textures which rarely form abnormal grains. (b1) Boundaries and (b2) IPF map from the 63CR-0R sample annealed at 1150°C/2 h showing examples of abnormal grains, mainly from the $\langle 110 \rangle \parallel$ ND fiber.....112

Figure 55 - (a) Twin boundary fraction for cold-rolled and annealed AISI 316L processed by LPBF. (b1) Boundary maps for the 63CR-0R sample annealed at 1150°C for 4 h. Insets from figure (b1) are found as red square, showing (b2) recrystallized grains and black square showing (b3) abnormal grains. Note the formation of island grains in (b3).....114

LIST OF TABLES

Table 1 – Relationship between texture and process parameters. All texture components are related to the build direction (BD).....	45
Table 2 – Chemical composition of AISI 316L stainless steel powder and processed parts, as well as the nominal composition given by the ASTM A240 standard.....	57
Table 3 – Cell wall and interior fractions and the cell size for the 0R and 90R specimens, as measured by ECCI. ECCI: electron channeling contrast imaging; LAB: low angle boundaries.....	69
Table 4 - Dislocation density for 0R and 90R samples as measured by ECCI and XRD (Williamson-Smallman method). Stacking faults (intrinsic and extrinsic) and twinning probabilities are obtained from XRD data based on the Warren method.	99
Table 5 – Relative frequency of abnormal grains from a determined fiber texture. The angular deviation from the ideal fiber is smaller than 10°.....	108

LIST OF ACRONYMS

3-D	Three dimensional
AGG	Abnormal grain growth
AM	Additive manufacturing
BD	Building direction
CAD	Computer aided design
CC-EBSD	Cross correlation-electron backscatter diffraction
CI	Confidence index
CT	Coherent twins
DDW	Dense dislocation wall
EBM	Electron beam melting
EBSD	Electron backscatter diffraction
ECCI	Electron channeling contrast imaging
EDS	Energy dispersive spectroscopy
EEL-USP	Escola de Engenharia de Lorena – Universidade de São Paulo
EESC-USP	Escola de Engenharia de São Carlos – Universidade de São Paulo
EIGA	Electrode-induced gas atomization
FAPESP	Fundação de Amparo à Pesquisa do Estado de São Paulo
FEG	Field emission gun
FEM	Finite element method
GND	Geometrically necessary dislocations
GOS	Grain orientation spread
HAB	High angle boundaries
HIP	Hot isostatic pressing
HR-TEM	High-resolution-transmission electron microscopy
IPF	Inverse pole figure
ITA	Instituto Tecnológico de Aeronáutica
JMAK	Johnson-Mehl-Avrami-Kolmogorov
KAM	Kernel average misorientation
LAB	Low angle boundaries

LD	Loading direction
LMD	Laser metal deposition
LPBF	Laser powder-bed fusion
MAUD	Materials Analysis Using Diffraction
MG	Minas Gerais
MMC	Metal matrix composite
MPIE	Max-Planck-Institut für Eisenforschung
MPM	Microstructural path method
ND	Normal direction
ODF	Orientation distribution function
PPGEM	Programa de Pós-Graduação em Engenharia de Materiais
RD	Rolling direction
SD	Scanning direction
SF	Stacking fault
SFE	Stacking fault energy
SIBM	Strain-induced boundary migration
TD	Transverse direction
TEM	Transmission electron microscopy
EV	Volumetric energy density
XRD	X-ray diffraction

LIST OF SYMBOLS

δ -ferrite	Delta-ferrite
ε	True strain
$\langle \varepsilon_{hh}^2 \rangle^{1/2}$	Effective microstrain
λ	Wavelength (nm)
σ_{45}	Residual stress at $\varphi = 45^\circ$
σ_{SD}	Residual stress at $\varphi = 0^\circ$
σ_{TD}	Residual stress at $\varphi = 90^\circ$
σ_{vm}	Von Mises stress
b	Burgers vector
$C_{\beta\beta}$	Contiguity
d	Laser beam diameter
D_{eff}	Effective crystallite size
E_v	Volumetric energy density
h	Hatch spacing
l	Layer thickness
N_v	Recrystallized grains density
P_α	Probability of stacking fault formation
P_β	Probability of twinning
q	Laser power
R	Correlation coefficient
S_v	Density of boundaries separating recrystallized from non-recrystallized grains
v	Scanning speed
X_v	Recrystallized fraction

TABLE OF CONTENTS

1 Introduction	27
2 Aims, objectives and justifications.....	30
3 Literature review.....	31
3.1 Austenitic stainless steels	31
3.2 Powder feedstock employed in laser powder-bed fusion (LPBF)	32
3.3 Physical phenomena in the laser-particle interaction	35
3.4 Process parameters	37
3.5 AISI 316L microstructure processed by laser powder-bed fusion	39
3.6 Influence of scanning strategy on both texture and microstructure in AISI 316L steels processed by LPBF.....	43
3.7 Scanning strategy effects on the residual stresses of LPBF-processed metallic alloys.....	46
3.8 Plastic deformation in AISI 316L	48
3.8.1 Microstructural evolution and deformation heterogeneity	48
3.8.2 Conventional thermomechanical processing.....	50
3.8.3 Laser powder-bed fusion processing	53
3.9 Annealing of AISI 316L steel	54
3.9.1 Wrought-processed.....	54
3.9.2 LPBF-processed	56
4 Materials and methods.....	57
4.1 Pre-alloyed AISI 316L powder.....	57
4.2 LPBF processing.....	58
4.3 Cold-rolling.....	59
4.4 Heat treatment	60
4.5 Metallographic preparation.....	60
4.6 Scanning electron microscopy (SEM)	61
4.7 X-ray diffraction (XRD)	61

4.7.1 Dislocation density and stacking fault probability	61
4.7.2 Residual stresses.....	63
4.8 Electron backscatter diffraction (EBSD).....	64
5 Results and discussion	64
5.1 As-built microstructures	64
5.1.1 Dislocation density and spatial distribution	68
5.1.2 Residual stresses.....	72
5.1.2.1 Macroscopic (type I) residual stress.....	72
5.1.2.2 Intragranular (type III) residual stresses.....	74
5.1.3 Misorientations.....	75
5.1.4 – Residual stresses and dislocation structures	75
5.1.5 – Theories for the dislocation character and dislocation structure evolution during LPBF	77
5.2 – Annealed condition	81
5.2.1 Differences in microstructure and recrystallization kinetics.....	86
5.2.2 Factors influencing the recrystallization kinetics	88
5.2.3 Recrystallization mechanisms.....	93
5.3 Cold rolling after LPBF processing.....	97
5.3.1 The influence of two different starting microstructures obtained by LPBF in cold rolling.....	100
5.4 Annealing of cold-rolled AISI 316L.....	102
5.4.1 Abnormal grain growth (AGG)	104
5.4.1.1 Roughening transition	104
5.4.1.2 Second-phase particles	105
5.4.1.3 Texture.....	107
6 Conclusions	115
References	117

1 Introduction

Additive manufacturing started in 1980 when the first consolidation of photopolymers in a three-dimensional (3D) configuration via ultraviolet light was reported (DEBROY *et al.*, 2018). Since then, many energy sources have been used to consolidate 3D parts, starting from different feedstocks. With the evolution of energy sources and computation, a transition between prototyping to functional parts processing was observed (HERZOG *et al.*, 2016).

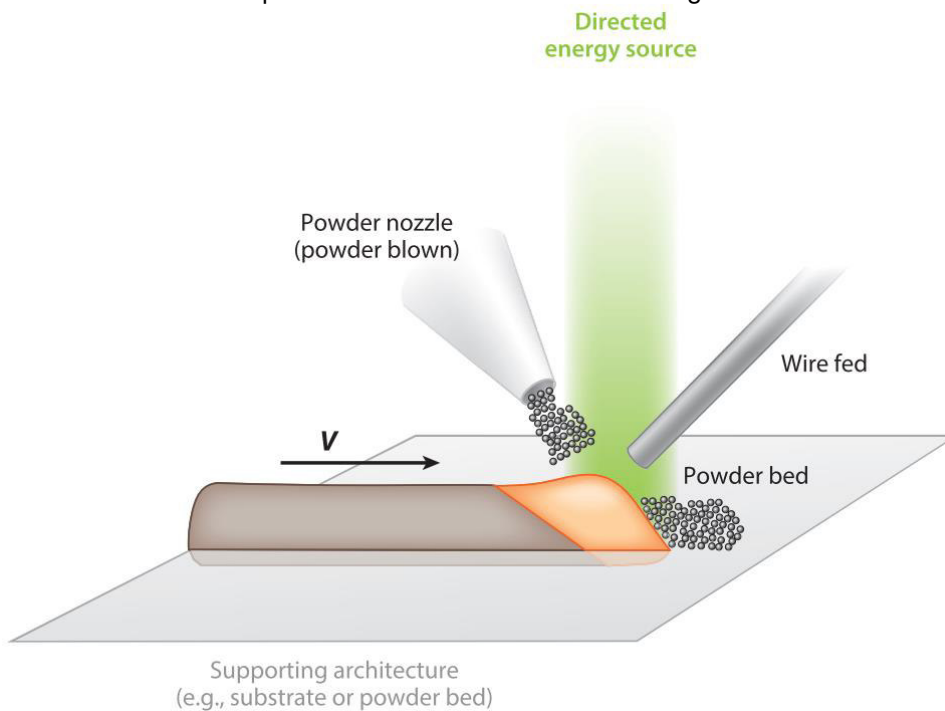
Differently from conventional manufacturing methods, based on the material's subtraction from a part having larger dimensions, additive manufacturing is based on the addition and consolidation of small portions of feedstock, powder or wire, in a layer-by-layer manner (HERZOG *et al.*, 2016). Additive manufacturing has the advantage of producing parts with complex geometries hardly attained by conventional methods (GU *et al.*, 2012; HERZOG *et al.*, 2016). The first step to produce a part is the creation of a CAD (computer aided design) model from the object, which is virtually divided in thin layers with a defined laser or electron beam scanning path. This file is transferred to the additive manufacturing machine, where the consolidation is performed layer by layer until the desired dimensions are achieved (GIBSON; ROSEN; STUCKER, 2015; GU *et al.*, 2012).

For the material consolidation, an electron or laser beam are used as energy sources, mainly for metals and alloys. The energy source may either melt or sinter the powder feedstock. Figure 1 shows the possible feedstock input, such as powder-bed, wire deposition or powder deposition (COLLINS *et al.*, 2016).

Additive manufacturing methods are classified depending on the combination of feedstock and energy source. Figure 2 shows this classification for different additive methods based on laser consolidation. In sintering, partial melting takes place, normally from a low melting point component (liquid phase sintering). In selective laser melting or laser powder-bed fusion (LPBF), the feedstock is deposited as a powder-bed, while, in laser metal deposition, powder is deposited through a nozzle (GU *et al.*, 2012).

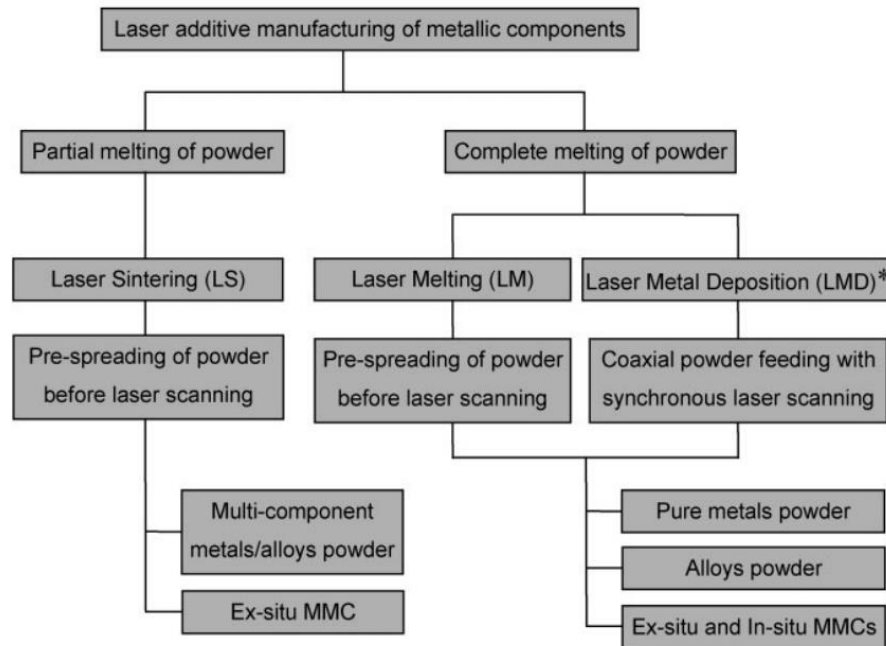
Another energy source largely employed is the electron beam. Electrons are accelerated and transform their kinetic energy into thermal energy when they hit the target with high conversion efficiency. In electron beam melting (EBM), a powder-bed is used, similarly to the LPBF. Alloys processed with this method are those highly reactive in oxygen- and/or nitrogen-containing environments, since EBM is performed in high vacuum (HERZOG *et al.*, 2016). In this technique, the powder bed is usually preheated.

Figure 1 – Feedstock addition possibilities in additive manufacturing.



Source: adapted from (COLLINS *et al.*, 2016)

Figure 2 – Different additive manufacturing methods based on laser beam consolidation.



Source: Adapted from (GU *et al.*, 2012)

In LPBF, melting occurs in small molten pools, resulting in high cooling rates around 10^4 K/s (PAULY *et al.*, 2018). As a result, a peculiar and anisotropic microstructure is formed due to the directional heat extraction, which creates thermodynamically out-of-equilibrium microstructures. In most cases, epitaxial grains are grown beyond the molten pool due to the partial re-melting from adjacent laser tracks and layers (THIJS *et al.*, 2010).

Austenitic stainless steels from the 300 series show a combination of moderate mechanical strength and high corrosion resistance in several environments, which explains their broad use in chemical, oil, gas, food-processing, and nuclear industries (MAJUMDAR *et al.*, 2005). Most of the works in this steel by additive manufacturing focuses on the mechanical properties (BAHL *et al.*, 2019; BOES *et al.*, 2019; CARLTON *et al.*, 2016; LIVERANI *et al.*, 2017; SUN; HAGIHARA; NAKANO, 2018; XUE *et al.*, 2010). However, only a few studies investigate the texture developed in AISI 316L steels (BAHL *et al.*, 2019; CASATI; LEMKE; EVANI, 2016; NIENDORF *et al.*, 2013; RIEMER *et al.*, 2014). The work from Yan, Xiong and Faierson (2017) superficially investigates the microstructure evolution upon annealing, and the corresponding texture changes, in the temperature range of 800-1100°C for 1 h. No earlier studies have been reported regarding the thermomechanical processing of AISI 316L produced by LPBF.

2 Aims, objectives and justifications

The aim of this Dissertation is understanding the aspects and the underlying mechanisms related to laser powder-bed fusion and several possibilities regarding post processing to optimize the microstructure from 3-D printed parts by adjusting process parameters and post-processing routines. Therefore, we underline the following research objectives:

1 - Understanding the mechanism of dislocation cell formation in the as-built microstructure:

- Perform an in-depth characterization of the dislocation structures in terms of spatial distribution, size and dislocation density;
- Investigate the interplay between residual stresses and dislocation cell formation;
- Suggest a mechanism for dislocation cell formation.

2 – Understanding the recrystallization evolution and the related mechanisms upon annealing:

- Assess the nucleation clustering of recrystallized grains;
- Quantify the recrystallization kinetics and investigate possible differences in kinetics due to the employed scanning strategy;
- Understand the active recrystallization mechanisms, their interplay, and the impact on the overall recrystallization kinetics;
- Investigate the possibility of creating engineered grain structure through partial recrystallization.

3 – Understand the microstructural evolution upon hybrid manufacturing (LPBF followed by cold-rolling and annealing):

- Understand the active deformation mechanisms upon cold-rolling in such unique microstructure;
- Evaluate the main factors influencing the grain evolution upon annealing, especially regarding abnormal grain growth.

3 Literature review

3.1 Austenitic stainless steels

In 1821, P. Berthier observed the enhancement of corrosion resistance by adding chromium to iron. In 1906, L. Guillet studied the properties of steels in the Fe-Cr-Ni system. In 1909, Portevin and Giesen published papers on martensitic and austenitic stainless steels, respectively. Monnartz showed in 1911 that the remarkable corrosion resistance in stainless steels resulted from the addition of ~12% (wt.%) of chromium. In the same year, Dantsizen and Becket, both employees from United Steels, discovered ferritic stainless steels. Brearley discovered martensitic stainless steels in 1912, the same year when Strauss and Maurer discovered austenitic and martensitic grades in the German company Krupp Stahl. Such steels were intensely produced by Krupp Stahl (Germany), Thomas Firth & Sons Ltd (England) and Firth-Sterling (United States of America) (PADILHA, 2002). Currently, these steels have many applications, from household items to critical components in nuclear fission reactors (GUPTA; BIRBILIS, 2015).

The flexibility in applications is justified by the excellent corrosion resistance, good weldability and moderate mechanical properties (BADDOO, 2008; PADILHA; PLAUT; RIOS, 2003). The moderate mechanical properties originate from several hardening mechanisms including alloying and thermomechanical processing (PADILHA; RIOS, 2002). The corrosion resistance comes from the addition of at least 11wt.% of chromium, creating passive chromium oxide nanolayers (GUPTA; BIRBILIS, 2015; LO; SHEK; LAI, 2009). The addition of higher contents of chromium increases the corrosion resistance due to the gradual replacement of the original oxide layer by a passive chromium oxide layer (GUPTA; BIRBILIS, 2015).

Stainless steels are classified in six classes: ferritic, austenitic, martensitic, duplex, precipitation-hardened (PH) and, more recently, austenitic with partial substitution of nickel by manganese or by nitrogen (LO; SHEK; LAI, 2009). The austenitic grades respond for two thirds of the yearly global production of stainless steels (PADILHA; RIOS, 2002). These steels retain the austenitic phase at room temperature. This effect results from the addition of 8-14% (wt.%) nickel in this alloy, combined with the presence of manganese and small amounts of nitrogen and carbon, acting as austenite stabilizers (MARÉCHAL, 2011).

In this class of stainless steels, the 304 and 316 are the most used worldwide, also with their low-carbon versions, 304L and 316L. The reduction in the carbon content reduces the formation of chromium carbides, which would locally reduce the chromium content, consequently diminishing the corrosion resistance from austenitic stainless steels (GUPTA; BIRBILIS, 2015).

The 316L austenitic stainless steels usually shows small amounts of delta ferrite resulting from the solidification. The addition of 2.5% (wt.%) of molybdenum in this material improves the corrosion and creep resistance (CHOWDHURY; DAS; DE, 2005). The high contents of nickel and molybdenum increase the stacking fault energy (SFE) for this material, which is around 40-60 mJ/m², depending on the chemical composition (LO; SHEK; LAI, 2009). The SFE from this steel processed by laser metal deposition was reported as 32.8 mJ/m² (WOO *et al.*, 2020). Therefore, this steel is in the limit between low and intermediate SFE materials. The stacking fault energy directly affects the plastic deformation mechanisms. For example, a higher propensity of dislocation slip as the main deformation mechanism is found for intermediate and high SFE, while mechanical twinning and transformation induced plasticity are more frequent for low-SFE materials (HUMPHREYS; HATHERLY, 2004a).

3.2 Powder feedstock employed in laser powder-bed fusion (LPBF)

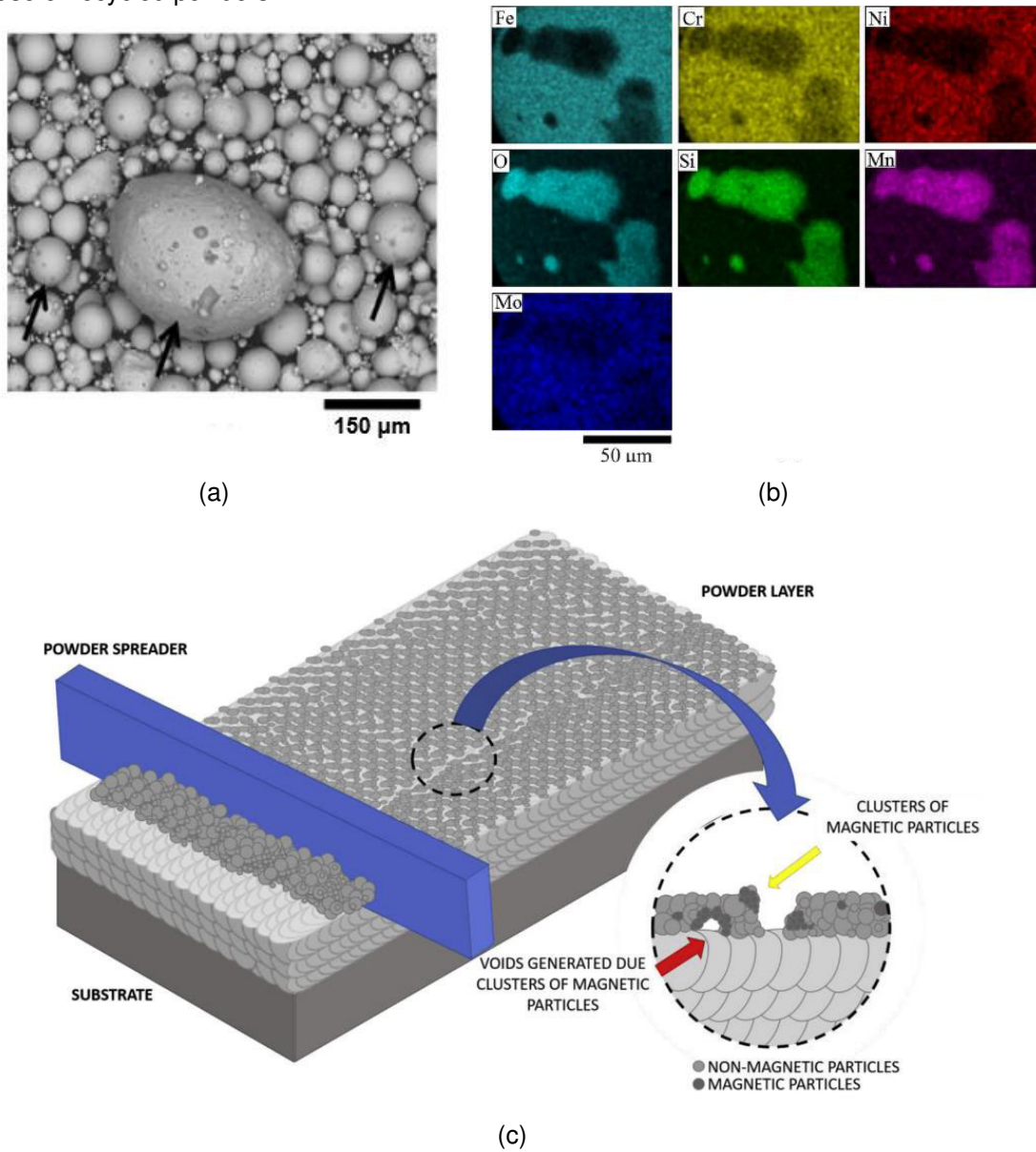
Usually, pre-alloyed powder feedstock is usually employed (HAYES *et al.*, 2009), i.e., particles already have the desired chemical composition. A part is shaped until a billet with desired geometry is obtained. This billet is melted and atomized in vacuum for reactive and refractory alloys or metals (GE *et al.*, 2012), or under inert gas atmosphere, usually argon. This method is called electrode-induced gas atomization (EIGA). The atomization is performed by heating the tip from the billet when applying an oscillating electromagnetic field. The material is melted and goes down due to gravity, in form of droplets, until an inert atmosphere chamber, where it is hit by an inert gas flow. Such process results in fine and spherical droplets, giving rise to the final powder following solidification (CHEN *et al.*, 2016; GRIGORIEV *et al.*, 2017; HUA *et al.*, 2009; VORA *et al.*, 2015; ZHOU *et al.*, 2018).

The EIGA process is used for additive manufacturing due to the need of using powders containing both spherical morphology and low amount of surface defects, such as satellite particles, shown in Figure 3a. This combination of smooth surface and spherical morphology is desired due to the better flowing (DEBROY *et al.*, 2018; ENGELI *et al.*, 2016), mainly at powder-bed techniques, allowing for a more uniform particle distribution.

For each method, there is an ideal particle size range. In LPBF, this range is between 15 and 45 μm . However, dense parts are also obtained by using different particle size ranges by adjusting process parameters (KARLSSON *et al.*, 2013; SPIERINGS; LEVY, 2009). Spierings e Levy (2009) highlight that some properties are different between parts produced from different size fractions. One example is the lower superficial roughness for the finer fraction of powder (SPIERINGS; LEVY, 2009).

Powder recycling, although theoretically justified, is not viable in practical terms. Using recycled powder, as well as using powder stored for long times, could create defects in the final part (LEUNG *et al.*, 2019; PINTO *et al.*, 2020; SIMONELLI *et al.*, 2015). Recycled powder shows higher chemical heterogeneity, including an eventual thicker oxidation layer when compared to the virgin powder. This occurs due to the formation of coarser laser spatter, which solidify at lower cooling rates than particles produced by EIGA (SIMONELLI *et al.*, 2015), as shown in Figure 3b. The lower cooling rate could also form δ -ferrite particles in AISI 316L powder, harming the particle flowability due to the magnetic behavior of this ferromagnetic phase (PINTO *et al.*, 2020). Figure 3c schematically shows the formation of magnetically-induced particle clusters and the associated defects created, such as voids in the powder-bed. The formation of laser spatter and the superficial oxidation are explained in more details in the next section.

Figure 3 – (a) Satellite particles on a particle surface. (b) Oxide layer and chemical heterogeneity in a recycled powder. (c) Graphic representation of magnetic particle clustering. All these factors harm the use of recycled powders



Source: Adapted from (a), (b) (SIMONELLI *et al.*, 2015) e (c) (PINTO *et al.*, 2020)

3.3 Physical phenomena in the laser-particle interaction

Laser powder-bed fusion is a process based on the interaction between the laser beam with a powder-bed, transforming it into a liquid phase, and further solidification. All these stages take place in a short time interval, where several physical phenomena occur and interact with each other.

The employed laser beam has a Gaussian energy distribution. The laser power that effectively penetrates the powder-bed depends on the particle roughness, reflectivity, material and size distribution (GU *et al.*, 2012; GUSAROV *et al.*, 2009; GUSAROV; KRUTH, 2005; HEELING; CLOOTS; WEGENER, 2017). Given the ongoing phase transformations, thermophysical properties, such as specific heat, specific mass, thermal conductivity, viscosity and surface tension are varied in a non-monotonic way (ANTONY; ARIVAZHAGAN; SENTHILKUMARAN, 2014; KHAIRALLAH *et al.*, 2016; KHAIRALLAH; ANDERSON, 2014).

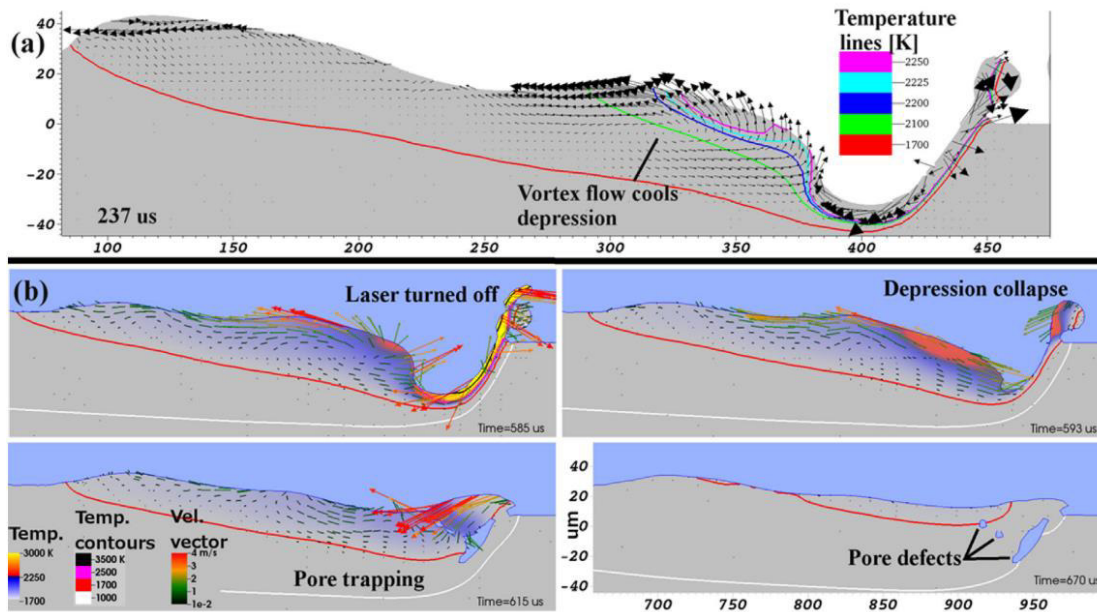
When the powder and the underlying layers reach the melting point, a molten pool is created, where the Marangoni effect acts. This effects allows for a liquid flow from regions at higher temperature to the lower ones due to the surface tension gradient (KHAIRALLAH *et al.*, 2016; KHAIRALLAH; ANDERSON, 2014; LY *et al.*, 2017; ZHAO *et al.*, 2017). As a result, the molten pool height is increased given the intensification in the liquid flow, maximizing heat and mass transfer, besides the ejection of laser spatter from low viscosity regions. Without the Marangoni effect, no laser spatter would be formed, since the intense flow aids the liquid ejection (KHAIRALLAH *et al.*, 2016; LY *et al.*, 2017; ZHAO *et al.*, 2017).

Laser spatter consist in liquid metal following ejected from the molten pool, which later solidifies as coarser particles. This phenomenon creates chemically heterogeneous particles and different phase composition when compared to the virgin powder (PINTO *et al.*, 2020; SIMONELLI *et al.*, 2015). Additionally, part of the coarse particles may arise from fast sintering promoted by the laser beam rather than laser spatter.

A higher oxygen content may also modify the surface tension coefficient from negative to positive, which would change the flow direction from the Marangoni effect, producing spatter (LEUNG *et al.*, 2019). Recoil pressure creates a force in the liquid surface which opposes to the force exerted by the material evaporation, resulting in a liquid surface depression.

This force aids the formation of spatter and increases the molten pool height (KHAIRALLAH *et al.*, 2016; LY *et al.*, 2017). Combined to the Marangoni effect, the recoil pressure assists cooling due to the evaporation and thermal radiation losses. Another possible effect is the generation of inner pores caused by the intense liquid flow (KHAIRALLAH *et al.*, 2016), as shown in Figure 4.

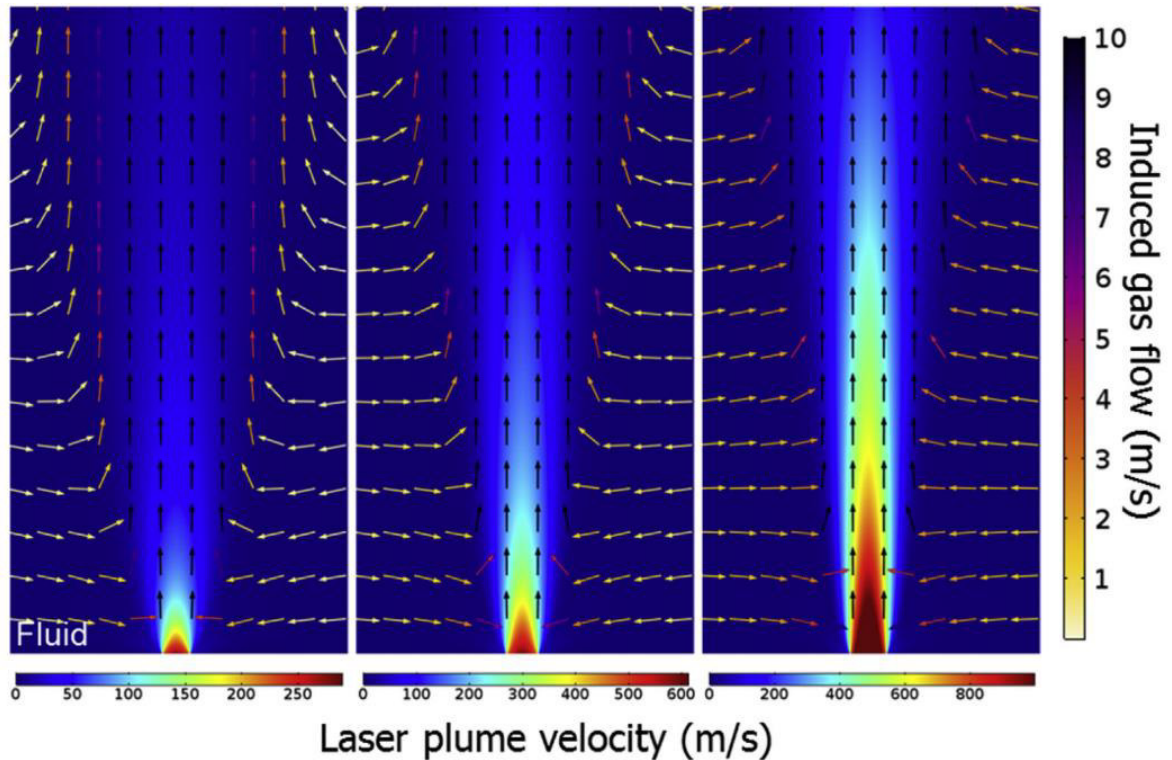
Figure 4 – Illustration of liquid flow forming inner pores in simulations. The red line represents the melting point of the material. Above this line, the material is found in the liquid state, while below it the material is found in the solid state.



Source: Adapted from (KHAIRALLAH *et al.*, 2016)

Laser plume is the mix of plasma and evaporated material, created by the laser scanning. It can reach upwards velocities of up to 800 m/s. As a result, a low-pressure region forms above the liquid surface, attracting the inert gas atmosphere to this region. The inert gas drags particles from the powder-bed to the laser plume, creating particle-poor regions. This effect is called denudation (BIDARE *et al.*, 2018). Figure 5 shows the simulation of inert gas flow and laser plume. These particles are lifted by the laser plume, melted and expelled. Often, two or more particles may be joined, creating coarser particles (BIDARE *et al.*, 2018). The interaction between these phenomena defines the conditions under which the material solidifies, impacting the final microstructure. To change the way these phenomena act, it is necessary to change the conditions that lead to its occurrence. Therefore, to control the microstructure, we must understand the influence of LPBF process parameters on the solidification condition.

Figure 5 – Inert gas flow simulation, indicated by arrows and their velocity, as shown by the lateral color scale, and the laser plume flow, indicated by the background colors and their velocity, based on the bottom color scale.



Source: adapted from (BIDARE *et al.*, 2018)

3.4 Process parameters

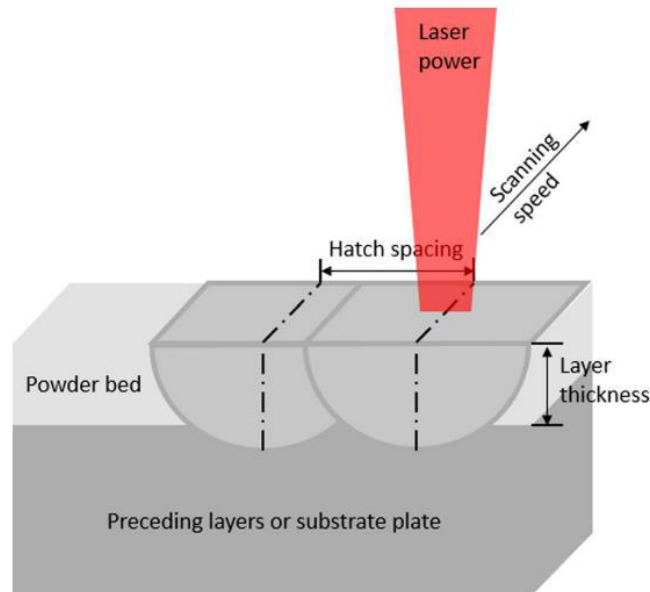
In LPBF, there are six main process parameters. The laser power (q) defines the energy quantity deposited in an area by time unit. The scanning speed (v) is the velocity with which the laser moves in the x-y plane. Hatch spacing (h) is the distance between two adjacent laser tracks. Layer height or layer thickness (l) is the powder layer height. The laser beam diameter (d) is the diameter corresponding to a 20% (d_{20}) intensity of laser power. Figure 6 summarizes these parameters. The scanning strategy is another important parameter, which defines the laser path in each layer.

Although it is not a process parameter itself, the volumetric energy density (E_v) is a frequently employed parameter. It reflects the provided energy amount per volume. This parameter, a thermodynamic quantification, does not reflect all the phenomena taking place during melting (SCIPIONI BERTOLI *et al.*, 2017), as the ones cited in Section 3.3 but it is used to resume all process parameters. Although limited, there is no other parameter used to effectively replace it. The volumetric energy density is calculated based on Equation 1:

$$E_V = \frac{q}{v l d} \quad (1)$$

where E_V is the volumetric energy density (J/m^3), q is the laser power (W), v is the scanning speed (m/s), l is the layer height (m), and d is the laser beam diameter (m).

Figure 6 – Main process parameters in laser powder-bed fusion.



Source: Adapted from (YAP *et al.*, 2015).

The first studies in additive manufacturing sought the ideal parameters to produce dense parts (>99%) by melting single track layers (MAJUMDAR *et al.*, 2005) or 3-D parts (CARTER *et al.*, 2016; KARLSSON *et al.*, 2013; MORGAN; SUTCLIFFE; O'NEILL, 2004; SPIERINGS; LEVY, 2009), with the aim of understanding the microstructure development.

Further studies sought for the optimal process conditions considering mechanical (BAI *et al.*, 2017; CHERRY *et al.*, 2014; LIVERANI *et al.*, 2017; SAEDI *et al.*, 2018) and physical properties, such as surface roughness (CHERRY *et al.*, 2014; KRUTH *et al.*, 2004) and residual stresses (ALI; GHADBEIGI; MUMTAZ, 2018; KRUTH *et al.*, 2012), etc. Several works also investigate the influence of certain process variables on the solidification microstructure, such as texture and grain morphology (DEHOFF *et al.*, 2015; WANG; BEESE, 2017; XU *et al.*, 2017).

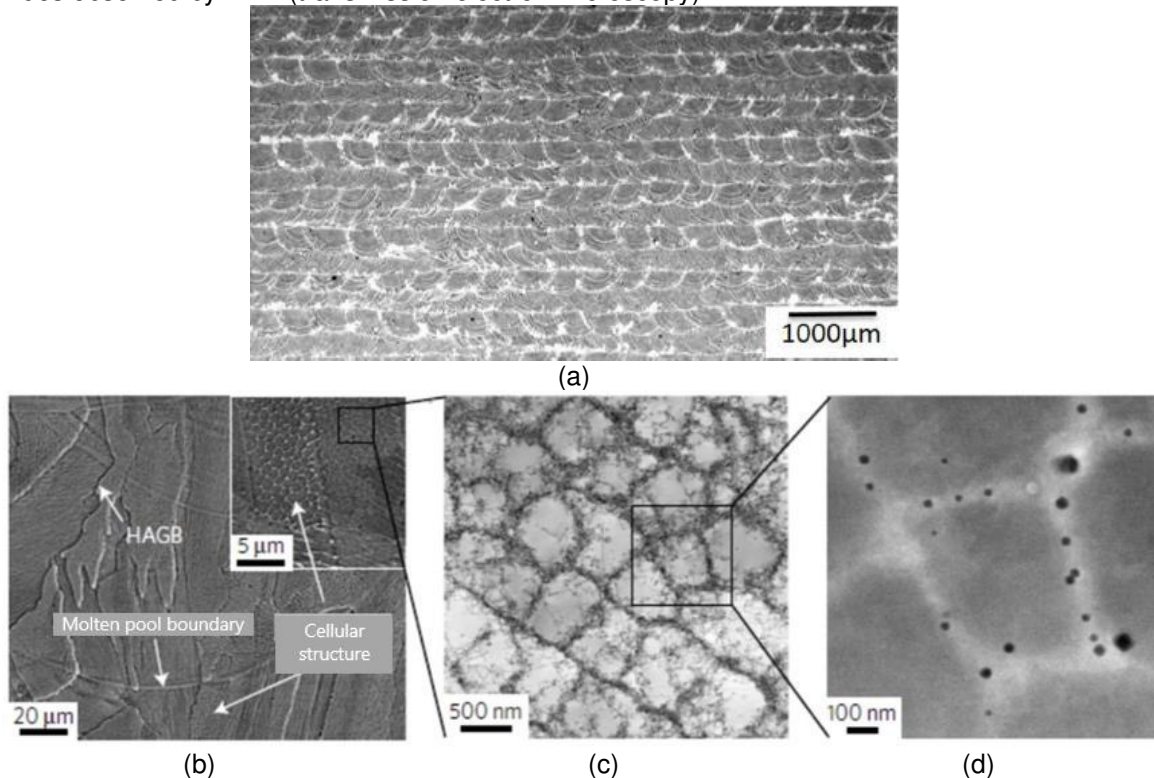
An in-depth review regarding the relationship between mechanical or physical properties and microstructure in AISI 316L steels processed by LPBF is given in the following Section 3.5.

3.5 AISI 316L microstructure processed by laser powder-bed fusion

The LPBF-processed AISI 316L steel shows a characteristic microstructure resulting from the imposed sequential thermal cycles. The molten pools are solidified in a hemispherical morphology (MONTERO-SISTIAGA *et al.*, 2018; YANG *et al.*, 2017), as shown in Figure 7a. In this figure, the scanning strategy is identified based on the molten pool pattern, where a 90° rotation between layers is used. In Figure 7b, grains crossing the molten pool boundaries are observed. This occurs due to the epitaxial growth, frequently observed in additive manufacturing, resulting from the heat flow directionality and the partial re-melting of previously consolidated layers (KRAKHMALEV *et al.*, 2018; THIJS *et al.*, 2013).

Within each grain, equiaxed dislocation cells are found, as shown in Figure 7c, resulting from the high cooling rates during solidification (KRAKHMALEV *et al.*, 2018; PACE *et al.*, 2017; WANG *et al.*, 2017; ZHONG *et al.*, 2017). However, some divergence is found regarding the origin of such cellular structures. Some authors claim that solidification cells are not dislocation cells, given the observation of molybdenum segregation at coarser solidification walls (2 μm), while dislocation cells are found in a finer scale between 0.2 and 0.5 μm (SMITH *et al.*, 2019), as shown in Figure 8a. In this point of view, solidification cells promote micro-segregation along their interfaces, while dislocation cells are formed due to the dynamic deformation imposed during cooling, given a lower yield stress at high temperatures (BIRNBAUM *et al.*, 2019).

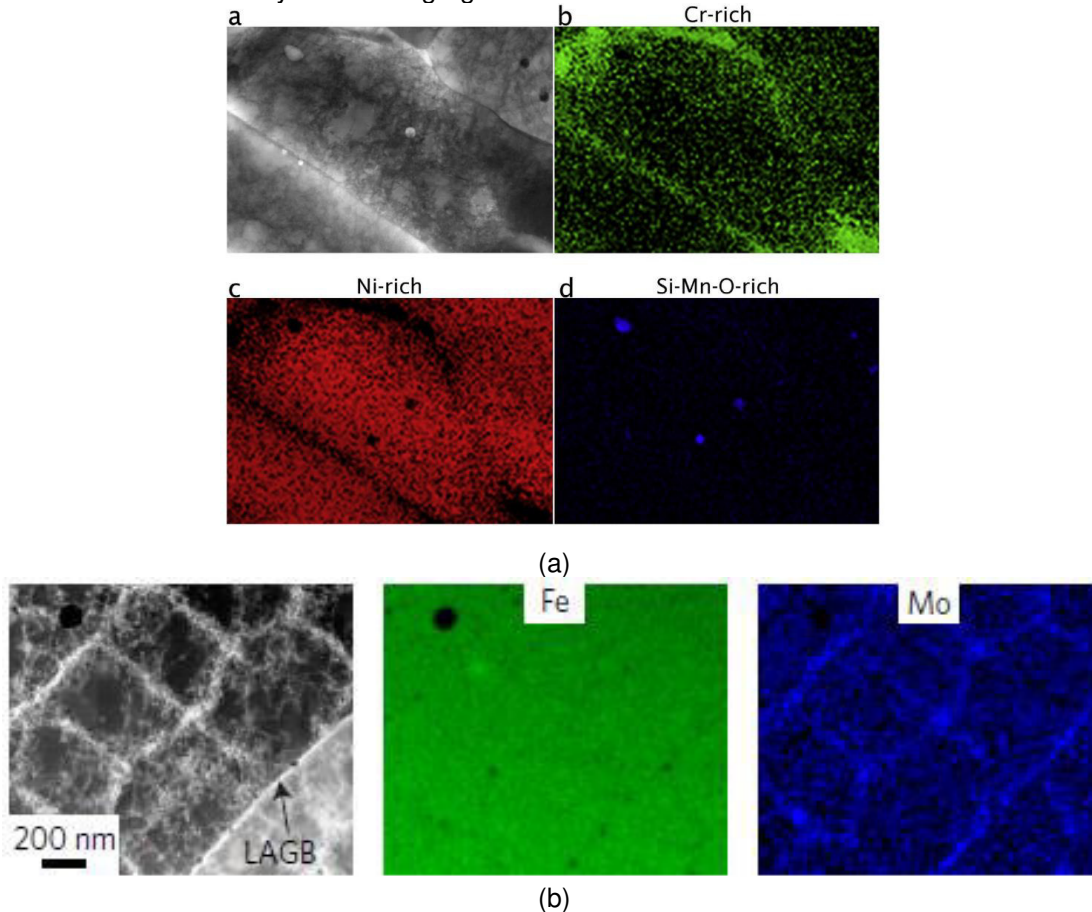
Figure 7 – (a) Molten pools in AISI 316L steel. (b) Epitaxial grains between molten pools and the cellular structure highlighted in the inset. (c) Cellular structure observed by TEM. (d) Nanometric oxides observed by TEM (transmission electron microscopy).



Source: Adapted from (a) (YANG *et al.*, 2017), (b), (c) e (d) (WANG *et al.*, 2017)

Most of the published works claim that solidification cells coincide with dislocation cells whose size vary between 0.2-0.8 μm, evidencing molybdenum segregation at cell walls (KRAKHMALOV *et al.*, 2018; MONTERO-SISTIAGA *et al.*, 2018; PACE *et al.*, 2017; WANG *et al.*, 2017; ZHONG *et al.*, 2017), as shown in Figure 8b. In this theory, the increase in dislocation density takes place due to molybdenum segregation at these interfaces, given the lattice parameter difference between regions enriched in molybdenum and the matrix (SAEIDI *et al.*, 2015a). A strong argument is the alignment of <100> directions with the growth direction of such cells. This direction is known as the fast growing direction in the solidification of cubic metals (MONTERO-SISTIAGA *et al.*, 2018). A more recent study reveal the formation of dislocation cells by the cyclic heating and cooling of a molten pool in a constrained region (BERTSCH *et al.*, 2020).

Figure 8 – Difference between solidification and dislocation cells. In (a), dislocation cells are found in the interior of solidification cells. Chromium segregation is visible at solidification cell walls. In (b), dislocation cells and molybdenum segregation at cell boundaries are visible and coincident.



Source: Adapted from (a) (SMITH *et al.*, 2019) e (b) (WANG *et al.*, 2017)

Besides dislocation cells, nanosized oxide particles are noticed mainly along cell walls, as shown in Figure 7d and 8d. The nature of these oxides is also controversial. Based on TEM (transmission electron microscopy) studies, iron, chromium, and manganese enrichment were found for these oxides (KRAKHMALEV *et al.*, 2018). Based on EDS measurements, Zhong *et al.* (2016) argue that such oxides are Si-enriched. Saeidi *et al.* (2015a, 2015b) claim, based on EDS from high resolution TEM, that such particles are amorphous silicates enriched in chromium. Wang *et al.* (2017) argue, based on EDS from TEM, that such silicates are actually enriched in manganese. Chen *et al.* (2019b) observed the precipitation of Mn-rich silicates following annealing at 400°C for 1 h. A specific characterization study of such nanoparticles by TEM indicates that these particles are rhodonite (MnSiO_3) (YAN *et al.*, 2018; YAN; XIONG; FAIERSON, 2017).

Following annealing at 1200°C for 1 h, these particles get enriched in chromium and transform into a spinel-like structure (MnCr_2O_4) acquiring a prismatic shape (YAN *et al.*, 2018). Similar findings were reported by Pinto *et al.* (2019) after investigating samples annealed for long times (48 h) at 1150°C.

The unique microstructure obtained by this processing leads to superior yield stress, ductility and tensile strength when compared to the conventionally processed counterpart (WANG *et al.*, 2017; YIN *et al.*, 2019). Some studies report a lower ductility due to the presence of pores (BAHL *et al.*, 2019; BOES *et al.*, 2019; LIVERANI *et al.*, 2017). The improved mechanical performance occurs due to the unique microstructure and substructure previously cited: high dislocation density forming cells, nanosized oxides and chemical segregation along dislocation cell walls (BAHL *et al.*, 2019; BOES *et al.*, 2019; LIVERANI *et al.*, 2017; SMITH *et al.*, 2019; WANG *et al.*, 2017; YIN *et al.*, 2019).

A strong microstructural anisotropy is found in terms of texture and grain morphology due to the epitaxial growth (THIJS *et al.*, 2013). This results in anisotropic mechanical properties, such as a higher mechanical strength perpendicular to the build direction (BD) (MOWER; LONG, 2016; THIJS *et al.*, 2013; WANG; PALMER; BEESE, 2016). This is explained based on two factors: the epitaxial grain's morphology creates a higher quantity of boundaries perpendicular to the BD (WANG; PALMER; BEESE, 2016). The second factor is texture, since slip systems are not favorably oriented regarding the load direction when it is applied perpendicular to the BD (THIJS *et al.*, 2013).

There is still a third factor that affects mechanical properties in LPBF alloys. When the load is applied along the BD, the elongation is often low and the material fractures with a brittle character (MOWER; LONG, 2016). This brittle fracture occurs due to the presence of pores and unmelted powder particles between the molten pools (DAI *et al.*, 2018; MOWER; LONG, 2016).

The microstructure also varies from the bottom to the top of the part. This occurs due to the difference in thermal history and cooling condition, where cooling is more intense at the bottom. As a result, a higher quantity of oxides (ZHONG *et al.*, 2016) and a higher dislocation density (SMITH *et al.*, 2019) are found near the bottom, resulting in higher mechanical strength. For maraging steels, more precipitates are also found at the bottom due to the more intense re-heating caused by the laser when scanning subsequent layers (KÜRNSTEINER *et al.*, 2017).

3.6 Influence of scanning strategy on both texture and microstructure in AISI 316L steels processed by LPBF

In Section 3.5, general microstructure features in LPBF-processed AISI 316L steels were discussed. Process parameters directly affects the obtained microstructure, mainly texture and grain-related parameters. Therefore, understanding the effect of process parameters, including the scanning strategy, on the texture is vital to control the process.

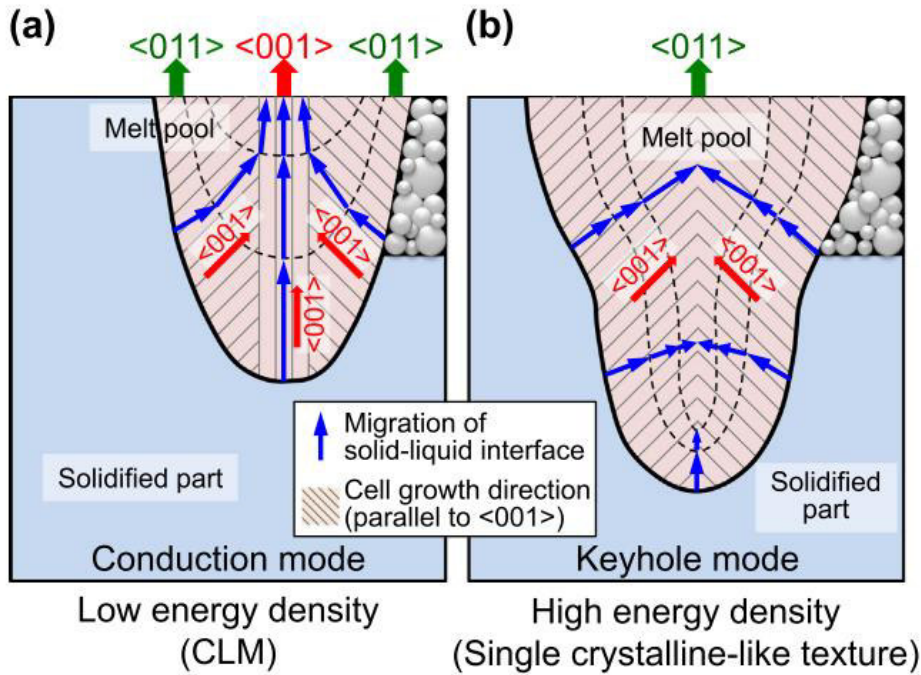
Increasing the laser power from 400 W to 1000 W, and using a 90° rotation between layers, leads to a transition in terms of texture and its intensity. The main texture component is Goss {110}<100> at 400 W, with a lower intensity of the Cube {100}<100> texture that arises at 1000 W due to the more intense epitaxial growth (BISWAS *et al.*, 2019).

By using a bidirectional scan with a 67° rotation between layers and changing the laser power from 380 to 950 W, while keeping the E_v near 104 J/mm³, a transition from a strong <100> || BD for a laser power of 380 W to a lower intensity <110> || BD for the higher laser power is found. This is explained based on the change in molten pool geometry, which changes not only the favorable growth direction, but allows the nucleation of equiaxial grains at the molten pool top, as shown by Monte Carlo simulations (SUN *et al.*, 2018).

From a bidirectional scan with a 67° rotation between layers and E_v of 104 J/mm³, besides pre-heating at 200°C, a higher quantity of $\Sigma 3$ and $\Sigma 9$ boundaries is found without a strong orientation (LALEH *et al.*, 2019). With the same scanning strategy, Bahl *et al.* (2019) found a change in texture when processing 7 x 7 x 2 mm³ rectangles built horizontally (2 mm is the height, parallel to BD) and vertically (7 mm is the height). In the horizontally processed sample, a strong <110> || BD fiber is found with a varying texture along the height. Evidences of a weak Rotated-Goss {110}<110> are also found. The sample processed vertically shows a weak texture with two fiber components: <110> || SD and <100> || SD.

For a bidirectional scan without rotation between layers, a lamellar microstructure is found with Goss {110}<100> growing epitaxially from the molten pool center sidelines, while Rotated-Cube {100}<110> is found along the centerline. A single crystal-like sample is obtained at high E_v . The change in texture is explained based on the molten pool shape (SUN *et al.*, 2019a), as seen in Figure 9.

Figure 9 – Molten pool shape effect on the grain orientation for (a) low volumetric energy density and (b) high volumetric energy density. CLM: crystallographic lamellar microstructure.



Source: Adapted from (SUN *et al.*, 2019a)

Employing a bidirectional scan with rotation of 0, 45 and 90° between layers, a comparison between high and low laser power was made. For larger rotations, a weaker texture is obtained, while simultaneously grains become finer (MONTERO-SISTIAGA *et al.*, 2018). Changing the laser power and the volumetric energy density, with a bidirectional strategy combined to 90° rotation between layers, a transition from $\langle 100 \rangle \parallel \text{BD}$ for the 380 W laser power (102 J/mm³) to a $\langle 110 \rangle \parallel \text{BD}$ when applying a 320 W laser power (86 J/mm³) was observed. For lower laser power, 260 (70 J/mm³) and 200 W (54 J/mm³), a random texture was observed (CHOO *et al.*, 2019).

Comparing the influence of a 90° rotation between layers and using a E_v of 91 J/mm³, a reduction in the Goss $\{110\}\langle 100 \rangle$ texture was observed for this rotation, promoting the emergence of a weak Cube $\{100\}\langle 100 \rangle$ texture component. When increasing the laser power, but reducing the scanning speed and keeping an E_v of 94 J/mm³, an intensification of the Goss $\{110\}\langle 100 \rangle$ texture was observed (ANDREAU *et al.*, 2019). Table 1 summarizes all parameter combinations and the resulting texture discussed on this section.

Table 1 – Relationship between texture and process parameters. All texture components are related to the build direction (BD).

Source	Volumetric energy density - E_v (J/mm ³)	Scanning strategy	Laser power (W)	Texture	Observations
(ANDREAU <i>et al.</i> , 2019)	91	Bidirectional scan	175	Goss {110}<001>	
(ANDREAU <i>et al.</i> , 2019)	94	Bidirectional scan	400	Goss {110}<001>	Stronger intensity than 175 W
(SUN <i>et al.</i> , 2019a)	-	Bidirectional scan	-	Rotated cube {100}<011> prevails, Goss {110}<001> along molten pool centerline	Low E_v
				Rotated Cube {100}<011>	High E_v
(LALEH <i>et al.</i> , 2019)	104	Bidirectional scan with a 67° rotation between layers	150	Random	Pre-heating at 200°C and high fraction of $\Sigma 3$ and $\Sigma 9$ boundaries
(BAHL <i>et al.</i> , 2019)	-	Bidirectional scan with a 67° rotation between layers	195	<011> BD with Goss {110}<001> <001> SD and <011> SD	BD is the shortest dimension SD is the shortest dimension
(SUN <i>et al.</i> , 2018)	104	Bidirectional scan with a 67° rotation between layers	380	<001> BD	(SUN <i>et al.</i> , 2018)
			950	<011> BD	-
(BISWAS <i>et al.</i> , 2019)	-	90° rotation between layers	400	Goss {110}<001>	-
			1000	Cubo {100}<001>	-
(CHOO <i>et al.</i> , 2019)	54	Bidirectional scan with a 90° rotation	200	Random	-
(CHOO <i>et al.</i> , 2019)	70	Bidirectional scan with a 90° rotation	260	Random	-
(CHOO <i>et al.</i> , 2019)	86	Bidirectional scan with a 90° rotation	320	<011> BD	-
(ANDREAU <i>et al.</i> , 2019)	91	Bidirectional scan with a 90° rotation	175	Goss {110}<001> e Cubo {100}<001>	Weaker texture compared to the non-rotated sample
(CHOO <i>et al.</i> , 2019)	102	Bidirectional scan with a 90° rotation	380	<001> BD	-

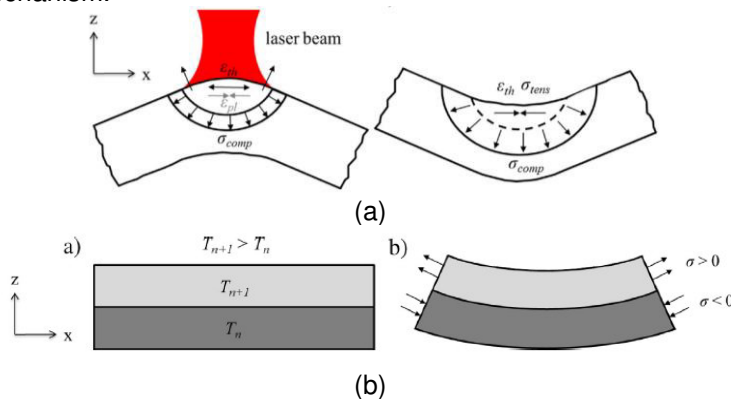
Source: Author

3.7 Scanning strategy effects on the residual stresses of LPBF-processed metallic alloys

Residual stresses are classified based on their length scale. Type-I stresses act on a macroscopic scale, creating global distortions in the component. Most of the stresses reported in AM are from type-I. Type-II stresses are microscopic and act in the grain scale, being frequently called as intergranular stresses. Such stresses arise from plasticity difference between neighboring grains. Type-III stresses occur at the atomic scale or intragranular scale, such as those arising from a vacancy formation (BARTLETT; LI, 2019). There are two models to explain the formation of residual stresses in LPBF-processed materials.

According to the thermal gradient mechanism, the material expands due to the heat input from the laser. However, this expansion is limited by the low temperature neighborhood, creating elastic compressive stresses in the heat affected zone. When exceeding the yield stress at high temperature, such stresses are relieved by plastic straining. When cooling, tensile stresses are generated in the plastically deformed area, warping the material, as shown in Figure 10a (SIMSON *et al.*, 2017). In the cooling down mechanism, the melted top has a higher temperature than the bottom layer. When cooling and solidifying the upper layer, it contracts more intensely than the underlying layer. Given the connection between such layers, this contraction is inhibited, creating tensile stresses in the upper layer in the same time that compressive stresses are created in the bottom layer, as shown in Figure 10b (SIMSON *et al.*, 2017).

Figure 10 – Residual stresses formation mechanisms: (a) thermal gradient mechanism and (b) cooling down mechanism.



Source: Adapted from (SIMSON *et al.*, 2017)

The complex thermal cycle along with high cooling rates results in strong residual stresses. Such stresses could be high enough to generate cracks in processed parts (CHAUVET *et al.*, 2018). Therefore, many methods were suggested to reduce residual stresses by tailoring process parameters, such as powder-bed pre-heating, reduction of laser power, and changes in scanning strategies (KRUTH *et al.*, 2012).

Many factors make the residual stress measurements complex for LPBF parts. Two factors are highlighted: the complex and non-uniform microstructure, as well as the experimental inaccuracy. The microstructure varies depending on the localization and significant variations in residual stresses are found, as the ones observed along the building direction (MISHUROVA *et al.*, 2019; STRANTZA *et al.*, 2019; YADROITSEV; YADROITSAVA, 2015).

The experimental inaccuracies arise from the available measurement techniques and the type of measured residual stresses. The residual stresses are partially relieved when the part is removed from the baseplate (BARTLETT; LI, 2019). Such stresses are measured by the deflection method, but it does not take into account the stored residual stresses in the part following the removal (ROBINSON *et al.*, 2018).

Given the two factors mentioned above, a significant difference in the experimental results is observed regarding the influence of process parameters on residual stresses. For example, shorter scan length, below 10 mm, reduces the residual stresses (KRUTH *et al.*, 2012; PARRY; ASHCROFT; WILDMAN, 2019). Such stresses are lower when measured perpendicular to the SD (KRUTH *et al.*, 2012; ROBINSON *et al.*, 2018; SIMSON *et al.*, 2017). Analyzing the sample lateral surface, residual stresses are higher along the BD (SIMSON *et al.*, 2017).

Island scanning strategies reduce residual stresses, but the island size does not affect it in Ti-6Al-4V alloy (KRUTH *et al.*, 2012). Another fact was the reduction in residual stresses when a 90° rotation between layers was employed (ALI; GHADBEIGI; MUMTAZ, 2018). Island scanning strategies had significant effect on residual stresses reduction and uniformization in AISI 316L steel (ROBINSON *et al.*, 2018). Residual stresses distribution is a critical factor that is not captured in many measurements due to experimental limitations. Parts with complex geometries have a more heterogeneous distribution of residual stresses, mainly in regions where a localized overheating is found (PARRY; ASHCROFT; WILDMAN, 2019).

By employing the finite element method (FEM), it has been observed that residual stresses are higher along sample edges, with tensile nature, while stresses are compressive in the center (AHMAD *et al.*, 2018; GANERIWALA *et al.*, 2019). Comparing the residual stress distribution between unidirectional and 90°-rotation scans, it was observed that the residual stress magnitude is not significantly changed. However, the strategy with the 90° rotation yields a more homogeneous stress distribution given the produced thermal history (PARRY; ASHCROFT; WILDMAN, 2016).

3.8 Plastic deformation in AISI 316L

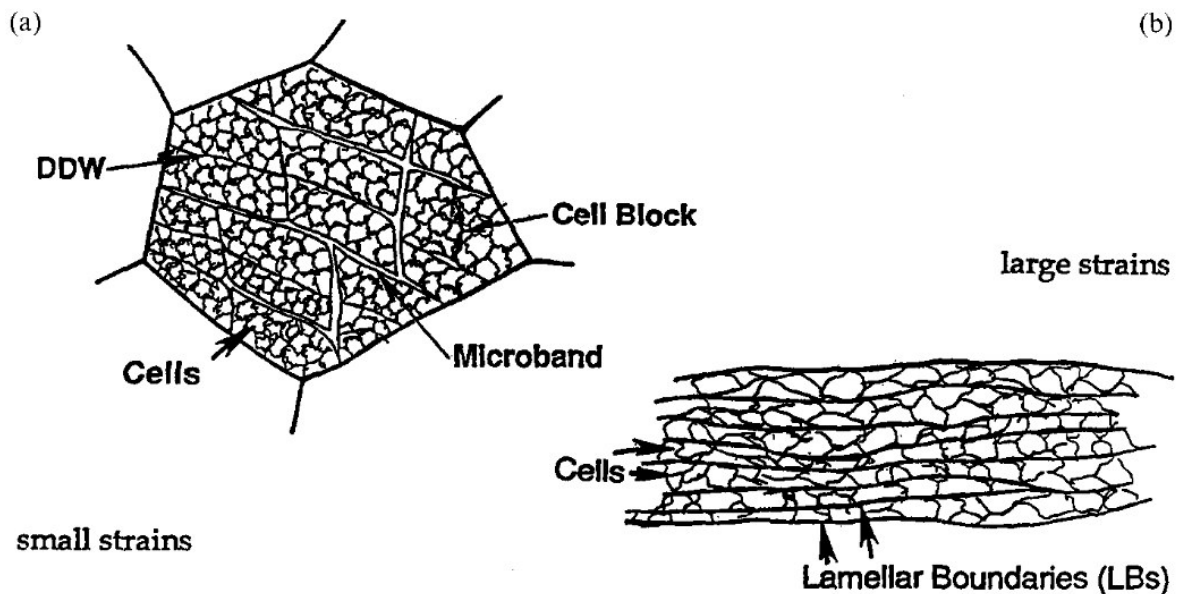
3.8.1 Microstructural evolution and deformation heterogeneity

The first polycrystal deformation model was proposed by Sachs (1928), which suggests that grains in a polycrystal deform as independent single crystals. However, this model does not attend the requirement of deformation continuity between adjacent grains (HANSEN, 1990), the so-called strain compatibility. In 1938, Taylor published his model assuming that all grains in a polycrystal are subjected to the same strain. Obtaining this macroscopic uniform strain requires the simultaneous activation of at least five independent slip systems, according to the Von Mises criterion (HANSEN, 1985). Later on, Kocks and Canova suggested that deformation continuity could be maintained by less than five independent slip systems for grains with special morphologies or at special sites, such as near grain boundaries. Deformation compatibility is kept along grain boundaries and not simultaneously throughout the grain. As a result, the yield stress is lowered (HANSEN, 1990). This variation in the number of active slip systems for each region of the grain, ultimately results in a heterogeneous plastic behavior. During deformation, dislocations move, multiply and annihilate in order to lower the stored energy in the form of defects, creating low energy dislocation structures (HANSEN, 1990; KUHLMANN-WILSDORF, 1999a, 1999b). Upon deformation, a lower number of slip systems is activated than the theoretically predicted, favoring the grain subdivision in small elements through dislocation structures (HANSEN, 1990).

Dislocation structures are classified as the ones formed at low-to-moderate and at large strains. For the first case, incidental dislocation boundaries, or dislocation cells, form by dislocation trapping (KUHLMANN-WILSDORF; HANSEN, 1991). Cells form cell blocks where the same slip systems were activated. Cell blocks are separated from other blocks subjected to different slip system activation by geometrically necessary boundaries, identified as dense dislocation walls (DDW) or microbands (HANSEN, 1990; HUGHES; HANSEN, 1997). Figure 11a shows the boundaries formed up to moderate straining. DDWs give rise to first-generation microbands. Microbands possess a higher dislocation density than DDW and arise from a different combination of slip systems (HANSEN, 1990). Increasing strain, the number of DDWs and microbands increases, as well as their intersection. A decrease in cell size is observed, as well as the increase in the boundary misorientation. Second generation microbands appear due to localized shearing (HANSEN, 1990).

At large strains, high angle boundaries tend to align with the deformation direction. Prior cell block structures are replaced by a lamellar structure. Lamellar boundaries are separated by relatively equiaxial subgrains (HUGHES; HANSEN, 1997), as Figure 11b shows.

Figure 11 – Dislocation boundaries formed upon straining up to (a) low-to-moderate strains and (b) large strains.



Source: Adapted from (HUGHES; HANSEN, 1997)

Grain subdivision is mediated by the formation of thicker dislocation walls, resulting in orientation spreading. The activation of different slip systems in each region from the crystal results in their rotation towards different orientations. The ambiguity of slip systems to unstable orientations could lead to divergent rotations (HUGHES; HANSEN, 1997).

In this way, texture and the microscopic deformation mechanisms interact to define the final microstructure and orientation. Upon deformation, regions with different slip systems could rotate towards different orientations. Such orientations could be more or less stable regarding deformation. This will, in turn, generate variable levels of grain subdivision and final orientations.

3.8.2 Conventional thermomechanical processing

The deformation behavior from a material is closely related to its stacking fault energy (SFE). From the SFE, it is possible to determine which deformation mechanisms are activated so that both microstructure and texture may be predicted with accuracy (RAVI KUMAR *et al.*, 2005). Lower SFEs hinder the dislocation movement, resulting in the gradual replacement of slip by mechanical twinning or strain-induced phase transformations (LO; SHEK; LAI, 2009).

AISI 316L has a SFE of 32.8 mJ/m² (WOO *et al.*, 2020), which classifies it as low-SFE material. Low-SFE materials deform mainly by twinning due to the restricted dislocation mobility. Materials with similar SFE and crystal structure exhibit similar plastic behavior, regardless of the chemical composition. For FCC materials with low or medium SFE, a Brass {110}<112> texture is observed after large straining (ODNOBOKOVA *et al.*, 2017). Initially, the emergence of a Brass {110}<112> texture was credited to mechanical twinning. However, other study indicate the great effect of micro-shear bands on the intensification of this texture component (EL-DANAF *et al.*, 2000).

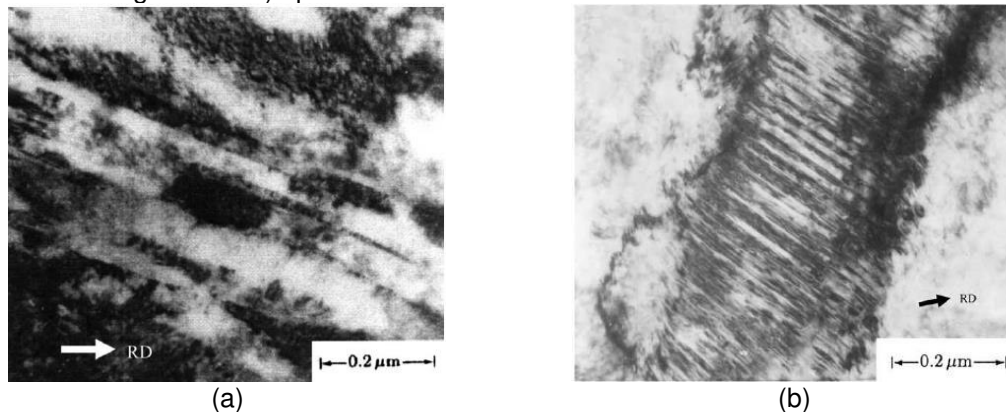
For wrought-processed AISI 316L, deformation occurs mainly through dislocation slip in bands up to 40% of cold rolling reduction, as seen in Figure 12a. From 60% of reduction, mechanical twinning is activated as an extra mechanism to accommodate the deformation, as shown in Figure 12b (CHOWDHURY; DAS; DE, 2005). In some cases, strain-induced martensite act as another alternative plasticity mechanism (ODNOBOKOVA; BELYAKOV; KAIBYSHEV, 2015).

Woo *et al.* (2020) observed SFE variations depending on the material deformation. However, this value was obtained from the stacking fault formation probability upon straining, indicating that microstructural evolution during deformation enables the formation of more twins. Up to 40% of deformation, Copper $\{112\}\langle 111\rangle$, Brass $\{110\}\langle 112\rangle$ and Goss $\{110\}\langle 100\rangle$ texture components are observed. By increasing the applied deformation, the Brass component is intensified, while Goss and twin-Cu $\{552\}\langle 225\rangle$ are intensified in a lower amount. The texture transition is mediated by mechanical twinning (CHOWDHURY; DAS; DE, 2005; HIRSCH; LÜCKE; HATHERLY, 1988).

The $\{111\}$ component is intensified due to the local deformation along shear bands (CHOWDHURY; DAS; DE, 2005; HIRSCH; LÜCKE; HATHERLY, 1988). A similar texture evolution was found in other works, with a strong Brass texture after deformation (NEZAKAT *et al.*, 2014; RAVI KUMAR *et al.*, 2005).

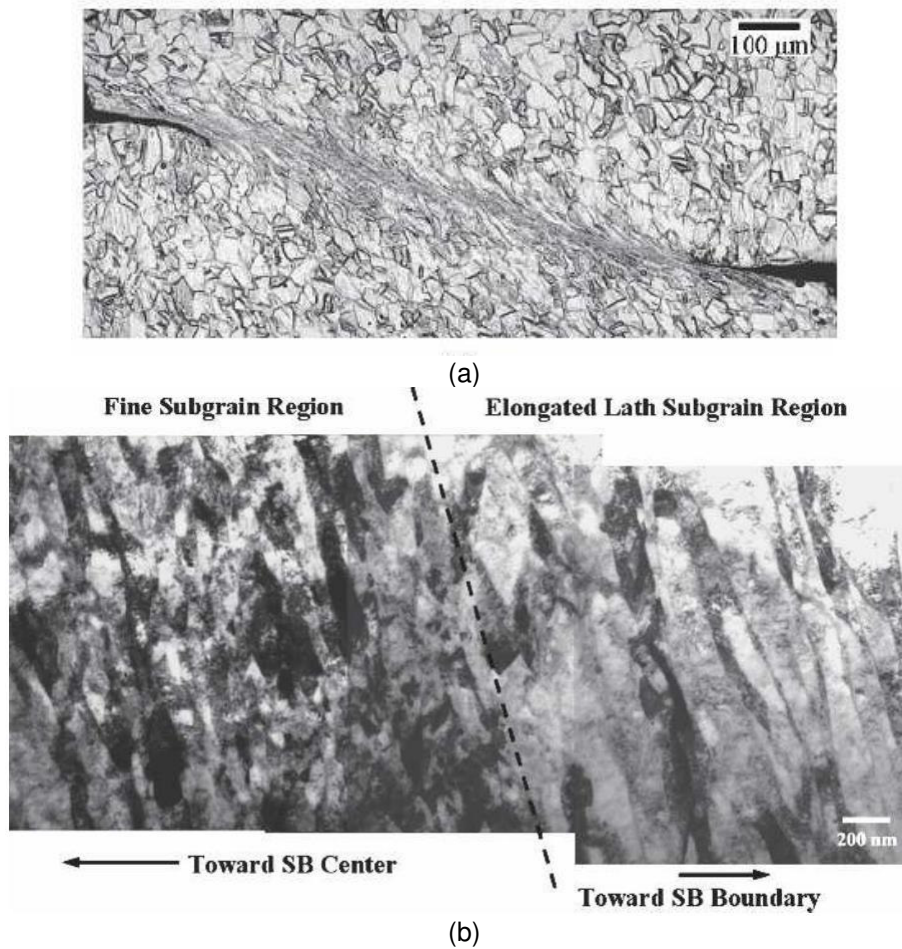
The number of mechanical twins depends not only on the applied strain, but the deformation mode. Biaxial deformation produces a higher quantity of $\Sigma 3$ boundaries, followed by planar and uniaxial loadings. This ability to produce more $\Sigma 3$ is accounted to the higher Taylor factor for the biaxial loading (MISHRA; NARASIMHAN; SAMAJDAR, 2007). Sinha *et al.* (2015) reported the formation of mechanical twins in grains showing low Taylor factor and related the twinning activation with internal stresses developed upon straining. Grains with higher internal stresses promoted mechanical twinning. Grain size is also an important factor to promote mechanical twinning. Coarser grains facilitate this phenomenon (EL-DANAF; KALIDINDI; DOHERTY, 1999).

Figure 12 – (a) Dislocation slip along bands (40% cold-rolling reduction) and (b) mechanical twinning (60% cold-rolling reduction) upon deformation in an AISI 316L steel.



Source: Adapted from (CHOWDHURY; DAS; DE, 2005)

Figure 13 – (a) Shear bands in AISI 316L in a coarser scale and (b) different subgrain morphologies developed in the center and along regions near the shear band boundary.



Source: Adapted from de (a) (XUE; GRAY, 2006a) e (b)(XUE; GRAY, 2006b).

The formation of adiabatic shear bands is observed in cases of extensive mechanical loads. This deformation mechanism is studied by specific compression split-Hopkinson bar, where a hat-shaped specimen is used. This mechanical test applied extensive shearing, where deformation is concentrated along shear bands. This results in a flowing aspect when observing the microstructure of these bands in a coarser scale (XUE; GRAY, 2006a), as shown in Figure 13a. Within these bands, a fine substructure is found, composed of equiaxed subgrains along the shear band center and elongated subgrains along regions near the shear band boundary. The shear bands grows from the center to its edges (XUE; GRAY, 2006b).

3.8.3 Laser powder-bed fusion processing

The initial texture from samples processed by LPBF directly affects its behavior upon plastic deformation. One specimen with strong $\langle 110 \rangle$ texture parallel to the tensile direction resulted in many twins due to its higher Taylor factor, differently from the $\langle 100 \rangle$ orientation (SUN *et al.*, 2018).

During tensile tests in AISI 316L processed by LPBF, intense twinning was observed in grains with $\langle 111 \rangle$ directions parallel to the loading direction (LD), while $\langle 100 \rangle$ grains showed intense dislocation slip (BAHL *et al.*, 2019; PHAM; DOVGYY; HOOPER, 2017). Mechanical twins were observed in deformation as low as 3% in tensile tests. High angle boundaries are apparently the nucleation sites of such twins. Mobile dislocations at this deformation are trapped by dislocation cell walls and subsequently released at higher strains (WANG *et al.*, 2017).

In single-crystal-like samples, $\langle 100 \rangle$, $\langle 110 \rangle$ and $\langle 111 \rangle$ parallel to the loading direction were produced. Samples with $\langle 111 \rangle \parallel$ LD showed higher mechanical strength (841 MPa), while the $\langle 110 \rangle \parallel$ LD showed higher ductility. For the $\langle 100 \rangle$ and $\langle 110 \rangle \parallel$ LD, a strong dislocation activity was observed, although the $\langle 110 \rangle \parallel$ LD direction presented a crystal rotation towards directions near the $\langle 111 \rangle$, promoting mechanical twinning, since $\langle 111 \rangle \parallel$ LD are characterized by intense twinning (WANG *et al.*, 2019).

Only a single study comparing different scanning strategies and their influence on the deformation behavior was found in the literature. However, no detailed microstructural characterization is provided, which would allow at understanding the deformation mechanism and texture evolution upon straining for this material (SALMAN *et al.*, 2019). In a split-Hopkinson bar test, no difference in terms of nanoindentation testing was observed between conventionally processed AISI 316L and their LPBF-processed counterparts, although the initial microstructure were expressively different (WEAVER; LIVESCU; MARA, 2020).

3.9 Annealing of AISI 316L steel

3.9.1 Wrought-processed

Several phenomena take place upon annealing in an alloy following processing, mainly those involving plastic deformation. Among the most studied phenomena in a single-phase alloy are recovery, recrystallization and grain growth (normal or abnormal). Recovery occurs based on either defect annihilation or rearrangement, such as vacancies, dislocations and stacking faults, without the movement of high angle boundaries (PADILHA; PLAUT; RIOS, 2003). Given the motion of lattice defects, mainly dislocations, SFE plays a key role, with a high SFE favoring recovering kinetics.

Although recrystallization and recovery are concurrent phenomena disputing the same thermodynamic potential, i.e., the elastic energy stored in lattice defects, recovery is precursor of recrystallization. Recovery, mainly subgrain growth, allows for the formation of high angle boundaries, ultimately resulting in recrystallization nuclei (HUMPHREYS; HATHERLY, 2004a). Recrystallization nuclei may be formed through recovery from the deformed structure or could previously exist in the deformed matrix. These nuclei sweep the deformation microstructure through the movement of mobile high angle boundaries (DILLAMORE; KATOH, 1974).

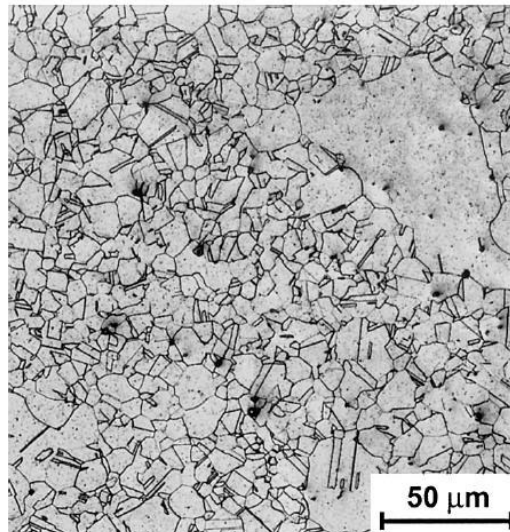
In the past, the recrystallization kinetics was discussed based on two theories: the oriented nucleation and oriented growth. In the first, it is suggested that nuclei from determined orientations are nucleated first and determine the final texture. For the second, grains with a favorable orientation will have a growth advantage and dominate the final texture (LEE, 1995). Recrystallization nucleation takes place at regions of both higher energy and curvature, conditions found along grain boundaries. One point in favor of the idea that nuclei previously exist in the deformed matrix, or their formation through recovery, is a similar orientation between recrystallized grains and the surrounding matrix (HUTCHINSON, 1989).

Recrystallization in AISI 316L steel deformed up to 95% thickness reduction shows preferential nucleation along shear bands, subsequently consuming the matrix. These are favorable sites due to the higher elastic stored energy. With the progress of recrystallization, annealing twins form and weaken the texture, producing an almost random texture (CHOWDHURY *et al.*, 2006).

Materials with higher SFE do not show profound twinning and a remaining orientation inherited from the deformed state or the promotion of other texture components, such as Cube $\{100\}\langle 100\rangle$, is observed upon annealing (RIDHA; HUTCHINSON, 1982).

Following recrystallization, grain growth may take place either normally or abnormally. Both phenomena arise from the need to reduce the surface energy. In normal grain growth (NGG), grains grow in a uniform way, maintain the log-normal grain size distribution. In abnormal grain growth (AGG), some grains grow faster than other, as shows Figure 14, resulting in a bimodal grain size distribution.

Figure 14 – Abnormal grain growth in AISI 370 austenitic stainless steel annealed at 1130°C for 30 min.



Source: Adapted from (PADILHA; PLAUT; RIOS, 2003)

AGG occurs when some grains show a growth advantage, as shown by the phase field simulation (LIU; MILITZER; PEREZ, 2019a). This advantage could be obtained by some effect related to texture, second phase particles, and grain boundary faceting (HUMPHREYS; HATHERLY, 2004a), besides solute drag as the boundary sweeps the microstructure (KIM; PARK, 2008).

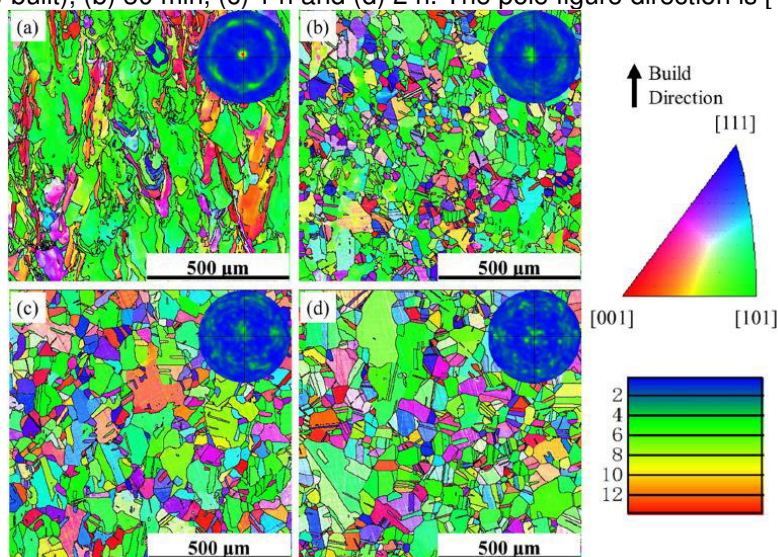
The high angle boundary character is extremely important for the mobility of such defects, allowing the accelerated growth of a few grains. This advantage through texture explains the growth of some texture components, such as Goss $\{110\}\langle 100\rangle$ in electrical steels given the higher probability of such grains presenting high-mobility boundaries surrounding them (HAYAKAWA; SZPUNAR, 1997).

3.9.2 LPBF-processed

Following annealing at 1050°C for 30 min, incomplete recrystallization was reported for AISI 316L steel. Nanometric oxides enriched in O, Al, Mn and Si were found prior to the annealing. Such oxides shrank upon annealing, although the author did not provide an explanation for this phenomenon (KONG *et al.*, 2018). When the material was subjected to hot isostatic pressing (HIP) at 1150°C for 4 h and 1000 bar, followed by an annealing at 1066°C for 1 h, a partially recrystallized microstructure was observed.

The same routine was followed in another study for obtaining a fully-recrystallized microstructure (LOU; ANDRESEN; REBAK, 2018). The same alloy processed by LMD showed complete recrystallization after annealing at 1060°C for 1 h (GRAY *et al.*, 2017). Partially recrystallized microstructures were also observed after annealing at 1070°C for 2 h (BLINN *et al.*, 2018). Annealing at lower temperatures is usually applied to relieve residual stresses, while retaining the cellular structure. Such treatments must be performed up to 400°C for 1 h for this goal (CHEN *et al.*, 2019b). Figure 15 shows the microstructural evolution upon annealing at 1200°C for different times. Observe the microstructural coarsening and texture weakening, likely due to the formation of annealing twins. After 2 h of annealing, the recrystallization is apparently completed (YAN *et al.*, 2018).

Figure 15 – Microstructural evolution in AISI 316L processed by laser powder-bed fusion at 1200°C for (a) 0 min (as-built), (b) 30 min, (c) 1 h and (d) 2 h. The pole figure direction is [110].



Source: Adapted from (YAN *et al.*, 2018)

4 Materials and methods

4.1 Pre-alloyed AISI 316L powder

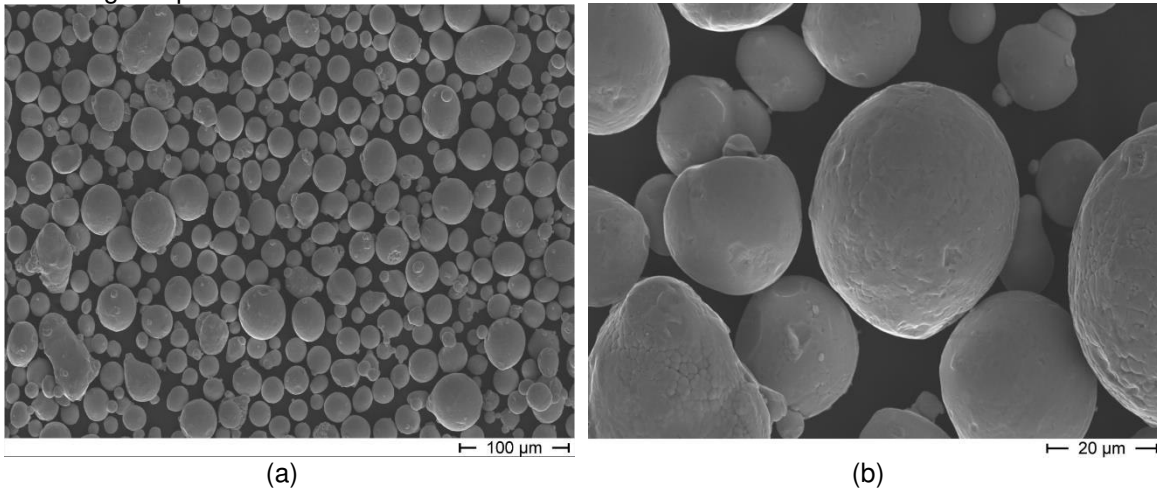
The powder used in this work was obtained from LPW Technology (Carpenter Additive) and shows an original particle size range between 15-45 μm . The powder was used around 20 times prior to the processing. Sieving (< 53 μm) was performed to remove coarser particles formed from laser spatter (SIMONELLI *et al.*, 2015). The chemical composition from the powder and the LPBF-processed part is shown in Table 2. For the LPBF-processed samples, the S content was determined by combustion and infrared radiation detection. The nitrogen content was determined via melting and inert gas drag. For the oxygen, measurements from the absorption of infrared radiation by the CO and CO₂ compounds are employed, while for nitrogen the analysis is performed by thermal conductivity. The employed equipments were Leco CS844 (S) and Leco ON736 (O and N). Remaining elements were determined by optical emission spectroscopy (OES) using the Thermo Scientific ARL-8860 spectrometer. The particle morphology was observed by scanning electron microscopy (SEM) in a CamScan microscope. Figure 16 shows the spherical and relatively smooth surface of such particles, with a few satellites attached to the surface formed during atomization.

Table 2 – Chemical composition of AISI 316L stainless steel powder and processed parts, as well as the nominal composition given by the ASTM A240 standard.

	Fe	Cr	Ni	Mo	Mn	Si	N	O	S	P
AISI 316L ASTM A- 240	Bal.	16-18	10-14	2-3	2	0.75	< 0.10	-	< 0.03	< 0.04
AISI 316L powder batch	Bal.	18.10	12.70	2.32	0.95	0.56	0.11	0.3	<0.01	<0.01
LPBF- processed AISI 316L parts	Bal.	18.02	12.23	2.32	0.87	0.65	0.09	-	<0.01	0.01

Source: Author

Figure 16 – (a) and (b) Scanning electron microscopy images from the powder batch used for processing samples.



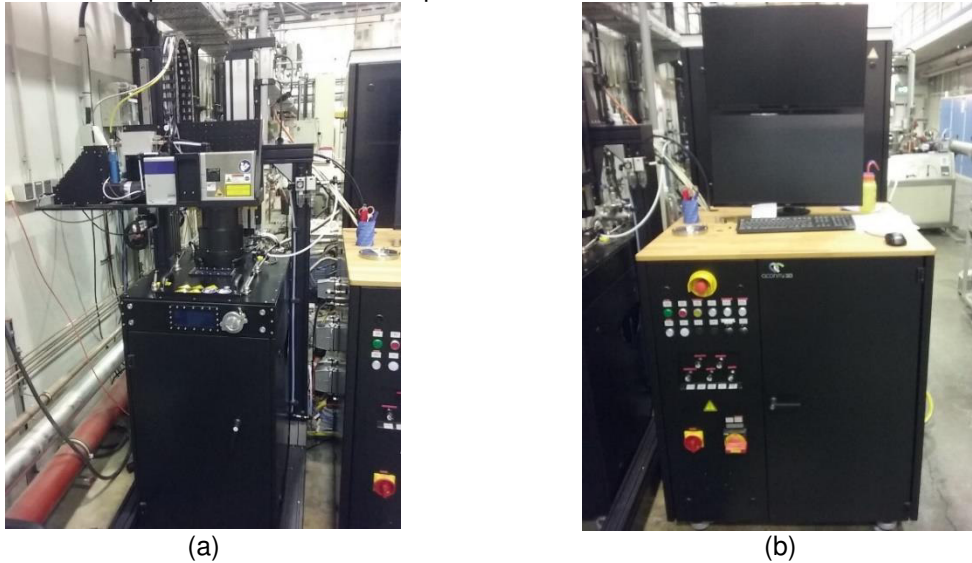
Source: Author

4.2 LPBF processing

15-mm-edge cube-shaped AISI 316L austenitic stainless-steel parts were processed with dimensions of $15 \times 15 \times 15 \text{ mm}^3$ by LPBF in an AconityMINI machine equipped with a Nd laser source ($\lambda = 1070 \text{ nm}$). Argon atmosphere is used with a residual oxygen content for processing within protected chamber. Figure 17 shows the employed LPBF machine from Max-Planck-Institut für Eisenforschung (Düsseldorf, Germany). All cubes were processed onto an AISI 316L baseplate, kept at a constant temperature of 25°C . The recoating process between the consolidation of each layer takes around 30 s. The selected process parameters were a laser power of 225 W, scanning speed of 1 m/s, layer height of $30 \mu\text{m}$, laser beam diameter of $90 \mu\text{m}$ and hatch spacing equal to $80 \mu\text{m}$. Such process parameters were selected based on a previous optimization study (AOTA et al., 2020).

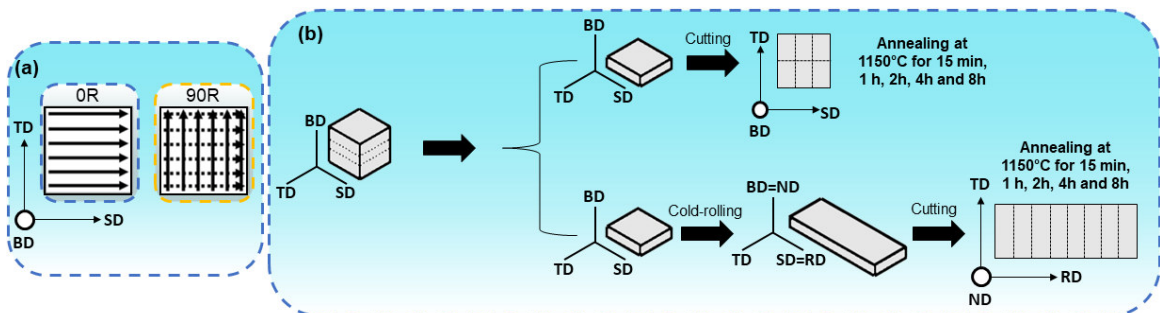
Four cubes (two for each strategy) were processed in a batch, employing two different scanning strategies, namely unidirectional scan (0R) and 90° rotation scan (90R), as shown in Figure 18a. No offset between layers is used. Following processing, samples were removed from the baseplate and cut in layers along the BD, as shown in Figure 18b through electrical discharge machining. The middle sections were used for comparative studies, since the microstructure does not vary significantly when samples from the same height are compared.

Figure 17 – (a) AconityMINI laser powder-bed fusion machine used for processing the parts and (b) computer, with an operational software coupled to the machine.



Source: Author

Figure 18 – (a) Employed scanning strategies, namely 0R and 90R. (b) Processing routine for the annealed samples and for cold-rolled and annealed samples. Both sets of samples were obtained from the middle section of a LPBF AISI 316L stainless steel.



Source: Author

4.3 Cold-rolling

Slabs, from both scanning strategies, with approximately 3.4 mm were cold rolled in multiple passes to 63% reduction in thickness ($\epsilon = 1.0$, real deformation) in a two-high rolling mill from Fenn installed at DEMAR-EEL-USP. The cold-rolling direction was along the initial scanning direction, where $BD \parallel ND$, as shown in Figure 18b.

4.4 Heat treatment

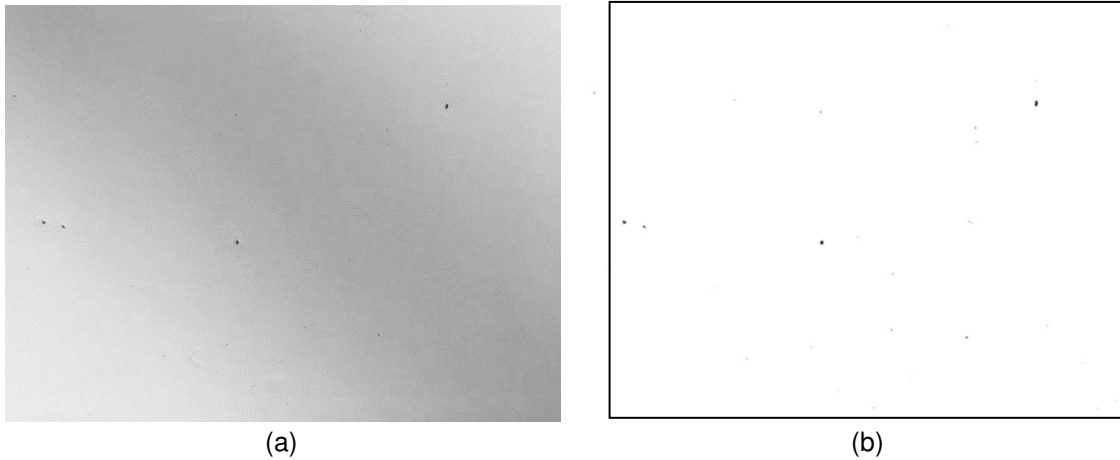
Samples in the as-built condition from both scanning strategies were cut in 6 parts with an ISOMET 2000 cutting machine. The cold-rolled samples were cut in several pieces with the same machine.

All samples were annealed under vacuum (in quartz tubes) at 1150°C for 15 min, 1, 2, 4 and 8 h counted after a pre-soaking time of 4 min in a Lindberg Blue tubular furnace installed at DEMAR-EEL-USP to evaluate the microstructural evolution. This temperature was chosen based on previous experiments (PINTO, 2019) due to two main reasons: at this temperature, (1) a single-phase austenitic matrix is thermodynamically stable; (2) the driving pressure for recrystallization is high enough to promote such solid state transformation. At lower temperatures, the recrystallization kinetics is sluggish or recrystallization do not occur. At higher temperatures, grain growth takes place.

4.5 Metallographic preparation

All samples were embedded in conductive bakelite resin. Grinding was performed up to #1200, followed by polishing in diamond suspension (3 μm). A second polishing step was performed using colloidal silica (0.04 μm). A final polishing step was performed by using a vibratory polisher (Vibromet) for 8 h at an amplitude of 60%. This last polishing step removes microstrains from previous polishing steps. Relative density was measured by using the threshold function from the ImageJ software in images acquired by optical microscopy, shown in Figure 19. In this method, the area fraction of pores (black dots in Figure 19b) can be quantified. Oxide nanoparticles are not observed in optical microscopy, which allows only for the detection of pores.

Figure 19 – (a) Optical microscopy image and (b) image following the application of the threshold function to quantify porosity.



Source: Author

4.6 Scanning electron microscopy (SEM)

All samples were investigated in several cross sections in a field emission gun (FEG) Merlin, installed at Max-Planck-Institut für Eisenforschung (MPIE). The electron channeling contrast imaging (ECCI) technique was employed to image lattice defects, as well as the oxides distribution. The issue of microstructure inhomogeneity inherent from LPBF is attenuated by comparing the dislocation structure from several samples. This is done by always investigating equivalent regions in a sample, i.e., $\langle 110 \rangle \parallel$ BD grains within the melt pool (away from the melt pool boundary). Standardless EDS measurements were performed on the same microscope under an acceleration voltage of 10 kV. Cold-rolled samples (63% CR) were also observed in the RD x ND cross sections under the backscattered electrons mode in a tungsten filament VEGA3 TESCAN at the Instituto Tecnológico de Aeronáutica (ITA).

4.7 X-ray diffraction (XRD)

4.7.1 Dislocation density and stacking fault probability

Conventional XRD measurements (θ - 2θ) were performed in a Seifert ID3003 (MPIE) with Co radiation ($\lambda = 0.178897$ nm) and beam size of 1×3 mm² (TD x SD). Measurements were performed for the cold-rolled specimens (RD x TD) cross section and for the SD x TD cross section from the as-built condition.

The acquired diffractograms were analyzed using a Rietveld refinement implemented in the software MAUD (Materials Analysis Using Diffraction) (LUTTEROTTI, 2006; LUTTEROTTI; SCARDI, 1990; SOUZA FILHO *et al.*, 2019). The accumulated microstrain $\langle \varepsilon_{hh^2} \rangle^{1/2}$ and the effective crystallite size (D_{eff}) were obtained based on the size-strain model from Popa, also implemented in MAUD (POPA, 1998). The probability of stacking fault (P_α) and twinning (P_β) formation were defined based on Warren's theory (WARREN, 1990). Stacking faults create peak shifting and symmetrical peak broadening based on the following equation, while twinning causes asymmetrical peak broadening and peak shifting:

$$\Delta(2\theta) = \frac{90\sqrt{3}(P_\alpha)\tan\theta}{\pi^2(u+b)h_0^2} \sum_b (\pm)L_0$$

where $\Delta(2\theta)$ is the peak shift in degrees, $L_0 = h + k + l$, $h_0 = (h^2 + k^2 + l^2)^{1/2}$. The number of broadened and unbroadened peaks are b and u , respectively. $\sum_b (\pm)L_0 / (u+b)h_0^2$ values are constant for different planes and found elsewhere (WARREN; AVERBACH, 1950). The probability is obtained as parameter in MAUD.

By associating the Popa model with the Warren model, an effective crystallite size is obtained, since stacking faults and twins also break coherent domains. The effective crystallite size is given as:

$$\frac{1}{D_{eff}} = \frac{1}{D} + \frac{(1.5P_\alpha + P_\beta)}{(u+b)ah_0^2} \sum_b |L_0|$$

where D is the coherent domain of the $\{hkl\}$ plane. The remaining constants depends on the reflecting plane of the crystal, also found elsewhere (WARREN; AVERBACH, 1950). The obtained microstrain value is used as input in the Williamson-Smallman (WILLIAMSON; SMALLMAN, 1956) equation with the effective crystallite size,

$$\rho = \left(\frac{3K\langle \varepsilon_{hh^2} \rangle}{D_{eff}^2 b^2} \right)^{1/2}$$

where $K = 16.6$, b is the Burgers vector for a FCC crystal.

4.7.2 Residual stresses

Residual stress measurements were performed in the top (SD x TD) cross section for the as-built condition, with and without electrochemical polishing. Electropolishing was performed at 28 V, using an electrolyte composed by 78 ml perchloric acid, 70 mL distilled water, 730 mL ethanol and 100 mL butoxy ethanol (BAHL et al., 2019) up to a removal of an approximately 250 μm thick layer. The X-ray beam ($2 \times 2 \text{ mm}^2$) was positioned at the center of each cross section and it covered around 20 laser tracks. A Cu-K α radiation source was ($\lambda = 0.154059 \text{ nm}$) was employed. The (331) peak was used for residual stresses measurements at roughly 138.2° . The 2θ range varied between 130.7 and 145° . Twenty-one steps were acquired for Ψ angles from -70 to 70° .

Three azimuthal angles φ were recorded: 0 , 45 and 90° , thus allowing for the determination of the biaxial principal stress components. For each φ angle, 21 ψ -tilts were used in the $\sin^2\psi$ analyses between -70 and $+70^\circ$. By assuming a biaxial stress state with unknown principal axes, the stress components σ_{SD} and σ_{TD} were determined based on the following equations (SPIESS et al., 2009; WELZEL et al., 2005):

$$\sigma_\varphi = \sigma_{SD} * \cos 2\varphi + \sigma_{TD} * \sin 2\varphi + \sigma_{shear} * \sin(2\varphi)$$

where:

$$\sigma_\varphi = \frac{1}{1/2s_2(hkl)} \cdot \frac{\partial d(\varphi, \psi)}{\partial \sin^2 \psi}$$

If shear stresses (σ_{shear}) occur in the sample coordinate system (S) given by the SD and TD directions, this indicates that the S-system is rotated with respect to the coordinate system of principal stresses (P) about the $\Delta\varphi$ angle:

$$\Delta\varphi = \frac{1}{2} \arctan\left(\frac{2\sigma_{shear}}{\sigma_{SD} - \sigma_{TD}}\right)$$

The principal stress components are thus given by:

$$\left\{ \begin{array}{l} \sigma_{11}^P = \sigma_{SD} * \cos^2 \Delta\varphi + \sigma_{TD} * \sin^2 \Delta\varphi + \sigma_{shear} * 2 * \sin \Delta\varphi * \cos \Delta\varphi \\ \sigma_{22}^P = \sigma_{SD} * \sin^2 \Delta\varphi + \sigma_{TD} * \cos^2 \Delta\varphi - \sigma_{shear} * 2 * \sin \Delta\varphi * \cos \Delta\varphi \\ \sigma_{12}^P = 0 \end{array} \right.$$

4.8 Electron backscatter diffraction (EBSD)

Electron backscatter diffraction (EBSD) was performed in a JEOL-6500F scanning electron microscope. EBSD maps ($600 \times 1700 \mu\text{m}^2$) were acquired using a step size of 500 nm. For the cold-rolled specimen, a map of $50 \times 100 \mu\text{m}^2$ was acquired with a 50 nm step size. A clean-up procedure involved removing points with confidence index (CI) below 0.1. Texture was calculated based on the discrete binning method using a bin size and Gaussian smoothing of 5° . Cross-correlation EBSD maps were obtained with a step size of 50 nm. Kikuchi diffraction patterns were acquired without binning. Cross correlation EBSD (CC-EBSD) data was treated on the CrossCourt (version 4) software. A point with low kernel average misorientation was chosen as the reference pattern for each grain. A remapping procedure was applied to remove any large rotations between the reference and the obtained diffraction pattern that could lead to inaccuracies on the measured elastic strains (BRITTON; WILKINSON, 2012). Only the austenite was found in all samples.

5 Results and discussion

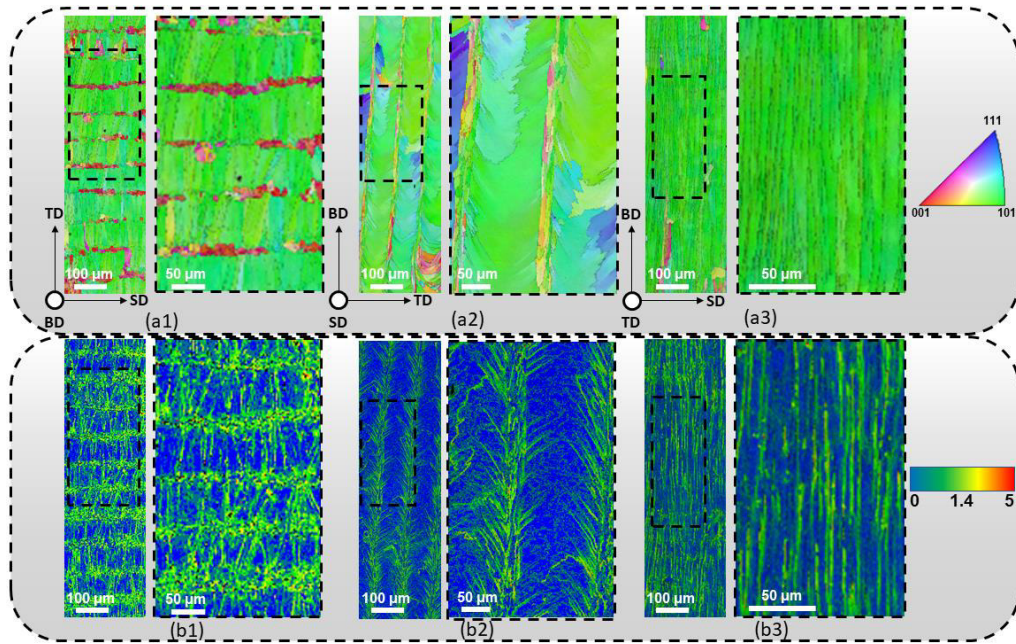
5.1 As-built microstructures

The inverse pole figures (IPF) and KAM maps of as-built microstructures obtained using the unidirectional and 90° -rotation scans are shown in Figures 20 and 21, respectively. The unidirectional scan creates a layered microstructure along the TD, as observed in the SD x TD and BD x TD cross sections in Figures 20a1 and 20a2, respectively. Coarse $\langle 110 \rangle \parallel \text{BD}$ grains alternate with fine $\langle 100 \rangle \parallel \text{BD}$ grains to build up this layered structure. Fine $\langle 100 \rangle \parallel \text{BD}$ grains appear along the center of melt pools, while coarse $\langle 110 \rangle \parallel \text{BD}$ grains lie along with regions where adjacent melt pools overlap each other. A non-uniform spatial distribution of strain or lattice rotation at different locations is shown by the KAM maps in Figure 20b. Lattice rotation arises because of the strain inhomogeneity upon solidification, and thus, geometrically-necessary dislocations (GND) maintain the compatibility of regions with distinct strain levels (HUGHES; HANSEN; BAMMANN, 2003). Regions with higher lattice rotations correspond to regions with a high GND density (SHEN; EFSING, 2018).

Regions with higher GND densities are located along $\langle 100 \rangle \parallel$ BD layers. Nucleation is more likely to occur at these preferential sites. For 90° -rotation between layers, an entirely different microstructure appears (Figure 21a). From the top layer (SD x TD), a chessboard-like pattern can be noticed. Fine grains are located at the borders, while coarse grains lie at the center of the chessboard pattern. A less regular orientation preference is observed for this case, although the $\langle 110 \rangle \parallel$ BD prevails for coarse grains and $\langle 100 \rangle \parallel$ BD orientations are still preferred for fine grains. The side cross section shown in Figure 21a2 illustrates a more random microstructure compared to the one from the unidirectional scan. Figure 21b shows KAM maps for the 90° -rotation between layers scan strategy. The regions showing high lattice rotation (higher dislocation densities), coincide with the melt pool center, i.e., regions of fine $\langle 100 \rangle \parallel$ BD grains. Recrystallization may also start preferentially along these nucleation sites. Observing the side cross section in Figure 21b2, a more even spatial distribution of lattice rotation, and thus the GND density, is found at the mesoscale.

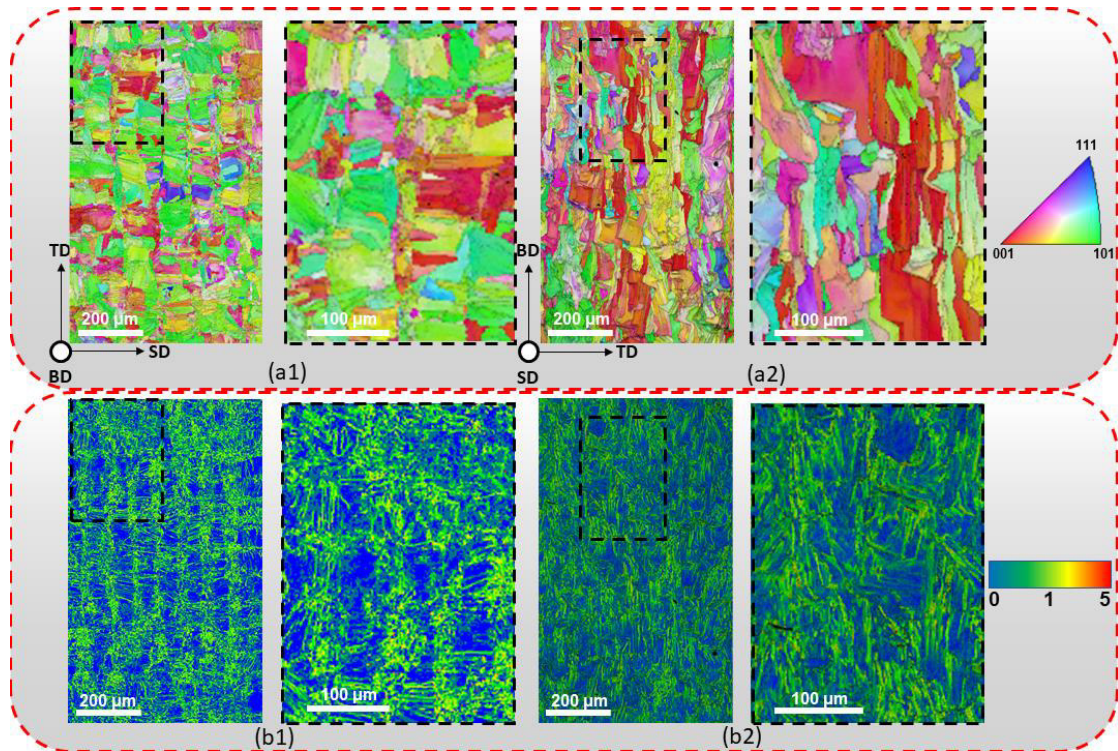
For this scan strategy, only two cross sections were investigated since the lateral cross sections BD x TD and BD x SD are equivalent due to the 90° -rotation between layers. Texture varies with the applied scan strategy. Pole figures from the SD x TD cross section are shown in Figures 22a and 22b for the unidirectional scan and after 90° -rotation between layers, respectively. The unidirectional scan yields a strong Goss $\{110\}\langle 100 \rangle$ texture, as shown in Figure 22a1. However, by observing the microstructure in the as-built condition (see Figure 20a), two different orientation components are found. Grain populations were sorted out by their size, since a bimodal grain size distribution is noticed, as indicated in Figure 22b. Grains coarser than $20 \mu\text{m}$ correspond to the $\langle 110 \rangle \parallel$ BD “coarse” grains, while grains finer than this threshold value are referred as “fine” grains. Their contoured pole figures are shown in Figure 22a2 for the coarse grains and Figure 22a3 for the fine grains. Grains with $\langle 110 \rangle \parallel$ BD correspond to the dominant Goss texture with $\langle 110 \rangle \parallel$ TD and $\langle 100 \rangle \parallel$ SD. Fine grains have different texture components, where a minor Rotated-Cube $\{100\}\langle 110 \rangle$ component is present besides the dominant Goss $\{110\}\langle 100 \rangle$ component, as shown in in Figure 22a3.

Figure 20 – (a) Unidirectional scan IPF maps for the (a1) SD x TD, (a2) BD x TD and (a3) BD x SD cross sections. Directions on the IPF are parallel to the BD. (b) Kernel average misorientation for the (b1) SD x TD, (b2) BD x TD and (b3) BD x SD cross sections.



Source: Author

Figure 21 – 90°-rotation IPF maps for the (a1) SD x TD and (a2) BD x TD cross sections. Kernel average misorientation maps for the (b1) SD x TD and (b2) BD x TD cross sections. The IPF indicates directions parallel to BD. Only two cross sections were investigated since the lateral BD x TD and BD x SD cross sections are equivalent due to the 90° rotation between layers.



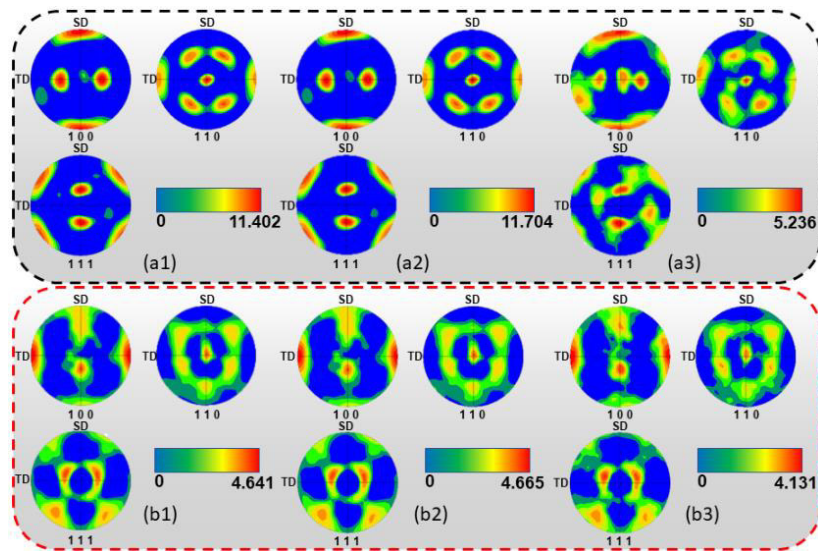
Source: Author

The 90°-rotation scan leads to a weaker global texture than the unidirectional one, as shown in Figure 22b1. Yet, a moderate texture with maximum intensity of 4.641 is found. As in the former case, the coarser grains correspond to the predominant texture by comparing Figures 22b1 and 22b2. In this case, the pole figures show a different orientation. Instead of a well-defined Goss {110}<100> texture, the 90°-rotation scan creates two Goss-like texture components which is rotated by 90° around the BD, resulting in a Goss {110}<100> and a Rotated-Goss {110}<110> texture due to the applied rotation, as each layer produces a Goss texture with the <110> || BD and <100> || SD. The pattern of grains containing a high GND density and the texture can be tailored by using different rotations between layers. The unidirectional scan along the employed process parameters create a layered microstructure consisting of grains with different sizes, shapes and orientations, as shown in Figure 20a. Different orientations are created from the relationship between thermal gradient direction and melt pool shape given the preferential growth of <100> directions in cubic crystals (SUN et al., 2019a), creating a strong Goss texture.

Coarse <110> || BD grains growing from the outer limits of the melt pools are created from regions where the overlap of adjacent melt pools occurs (RODGERS; MADISON; TIKARE, 2017).

The growth of such grains is possible due to the so-called side branching mechanism, which allows for the growth of new cells perpendicularly to the primary cells, while keeping the grain orientation (PHAM *et al.*, 2020) during epitaxial growth. The chessboard pattern shown in Figure 21b results from the previous consolidated layer on the following layer. As grains grow epitaxially during re-melting of layers or tracks (LIU *et al.*, 2019), grains from the previous layer keep growing to the next molten layer. However, the change in thermal gradient direction due to the scanning rotation between layers allow for the growth of a few grains with favorable orientation onto the next layer. Therefore, grain patterning from the previous layer is partially maintained in the next layer. Consolidating a new layer also creates a new pattern due to the growth of favorably oriented grains according to the melt pool shape. The superposition of two linear patterns rotated by 90° between each layer creates the chessboard-like pattern. This rotation is also reflected by the two Goss {110}<100> and Rotated-Goss {110}<110> texture components shown in Figure 22b.

Figure 22 – Pole figures for (a1) all data, (a2) coarse grains and (a3) fine grains in the unidirectional scan. Pole figures for (b1) all data, (b2) coarse grains and (b3) fine grains in the 90°-rotation scan. (1,2,3).



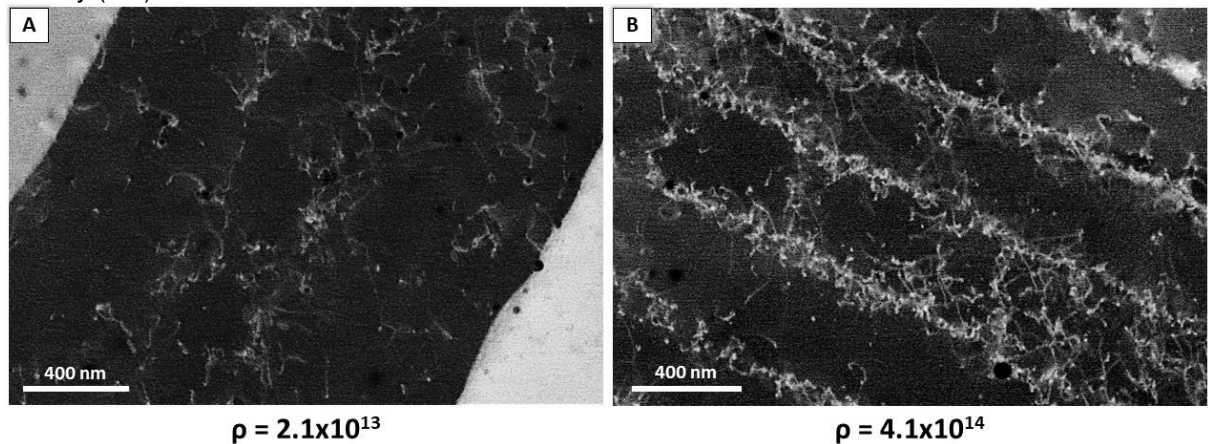
Source: Author

5.1.1 Dislocation density and spatial distribution

Dislocation structures are not found throughout the entire printed part. For example, the last consolidated layer has a low dislocation density ($2.1 \times 10^{13} \text{ m}^{-2}$) and a more random spatial distribution of dislocations (Figure 23a). This layer did not undergo any intense intrinsic heat treatment, since no other layer was consolidated above it. In the second last consolidated layer, the dislocation density is one order of magnitude higher ($4.1 \times 10^{14} \text{ m}^{-2}$) than in the last consolidated layer. Furthermore, a well-defined dislocation cell structure can be identified (Figure 25b). In the following, only features related to the bulk measurements are reported. Figure 24a and 24b show the dislocation structures in the bulk (middle cross section). Oxide particles are mainly located at dislocation cell walls, as shown by white arrows. The average dislocation density is higher in the 0R specimen ($6.7 \times 10^{14} \text{ m}^{-2}$ vs $4.1 \times 10^{14} \text{ m}^{-2}$ for the 90R specimen), Figure 25a, along a more defined dislocation structure, compare Figure 24a2 and 24b2. Both Figures 23 and 24 were obtained from the SD x TD cross section. However, the dislocation cell direction is different in both cases due to the side-branching upon solidification, where new cells grow perpendicular to the original $\langle 100 \rangle$ || BD direction while keeping their original crystallographic orientation (PHAM et al., 2020).

Figure 25 shows the quantification of dislocations as GND, SSD and total dislocation density. The total dislocation density along the dislocation cell walls and cell interior are, respectively, 17% and 100% higher in the 0R sample as compared to the 90R sample. In contrast, the ratio between the SSD and the GND values in the cell interior is 2.5-times higher in 90R sample as compared to 0R sample. The 0R specimen also exhibits a finer cell size (367 ± 41 nm vs 431 ± 49 nm in 90R specimen) and a higher are fraction of cell walls (0.49 vs 0.38 in 90R specimen). Cell walls are highlighted by orange dashed lines in Figure 4a2 and 4b2), shown in Table 3.

Figure 23 – Differences in dislocation structures in the (a) last consolidated layer and (b) second last consolidated layer for the 90R sample. The building direction is vertical for both images. ρ : dislocation density (m^{-2}).



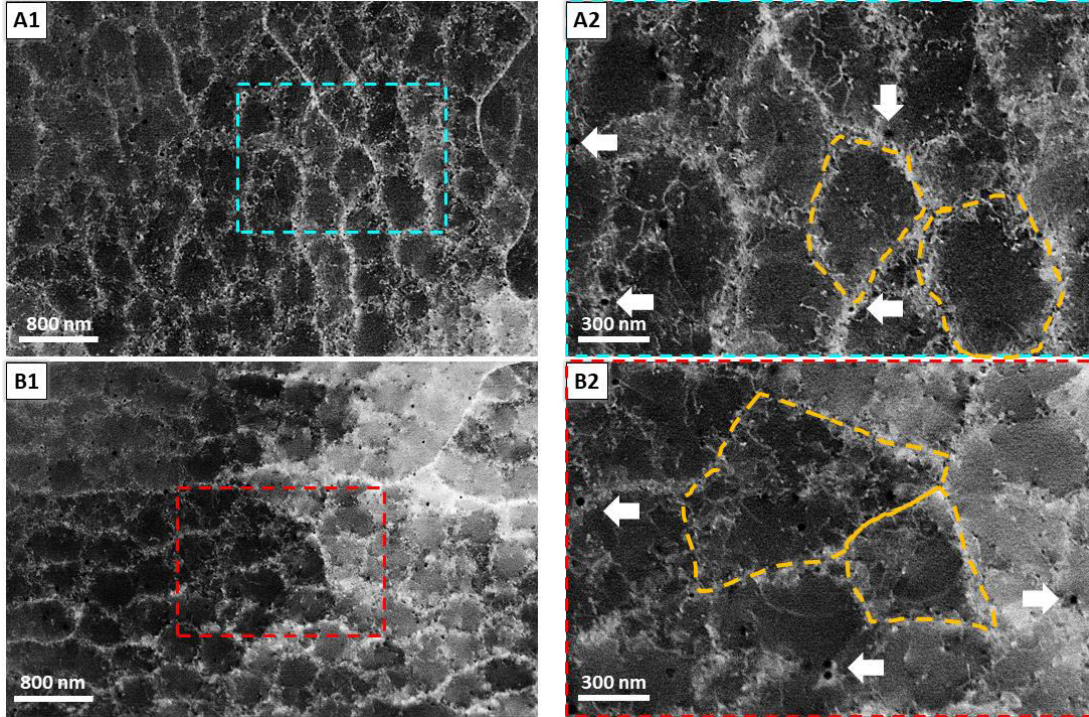
Source: Author

Table 3 – Cell wall and interior fractions and the cell size for the 0R and 90R specimens, as measured by ECCI. ECCI: electron channeling contrast imaging; LAB: low angle boundaries.

Samples	0R	90R
Cell walls fraction	0.49	0.38
Cell interior fraction	0.5	0.59
LAB fraction	0.01	0.03
Cell size (nm)	367 ± 41	431 ± 49

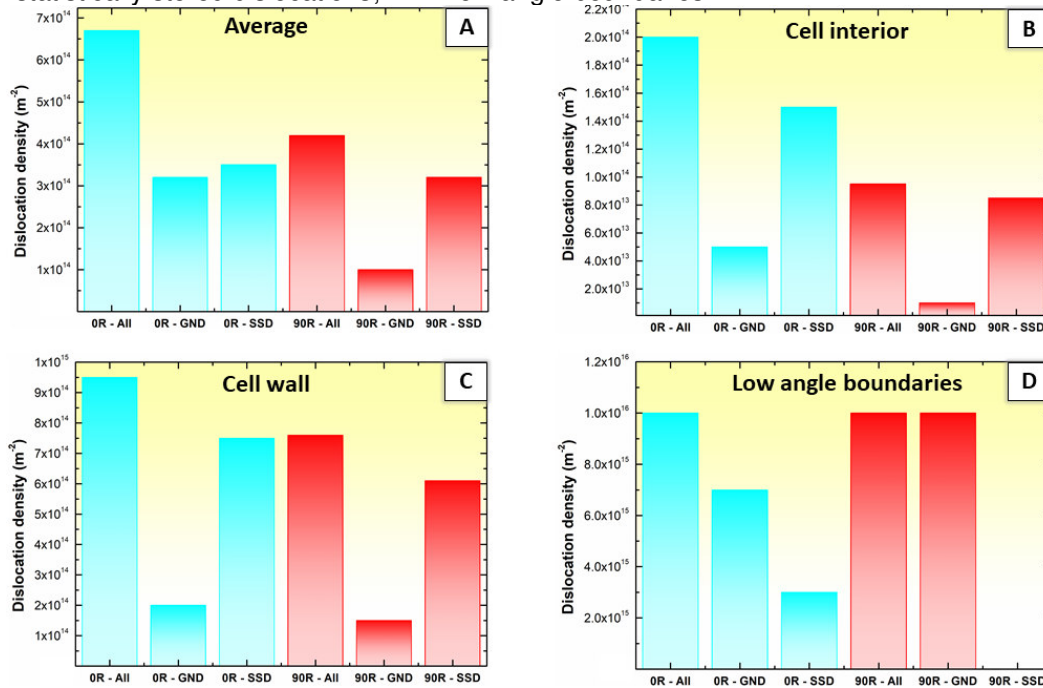
Source: Author

Figure 24 – ECCI images from the bulk in (a) 0R and (b) 90R samples. (a2) and (b2) show higher magnification images from regions highlighted by rectangles in (a1) and (b1), respectively. Images were taken from SD (parallel to the scale bar) x TD (perpendicular to the scale bar) cross sections. ECCI: electron channeling contrast imaging; SD: scanning direction; TD: transverse direction. White arrows indicate oxides along dislocation cell boundaries. Orange dashed lines indicate dislocation cell boundaries.



Source: Author

Figure 25 – Total dislocation, GND and SSD density for (a) average values from the specimens, (b) cell interior, (c) cell wall and (d) low angle boundaries. The low angle boundaries dislocation density was estimated based on (MONTEIRO et al., 2020). GND: geometrically necessary dislocations; SSD: statistically stored dislocations; LAB: low angle boundaries.



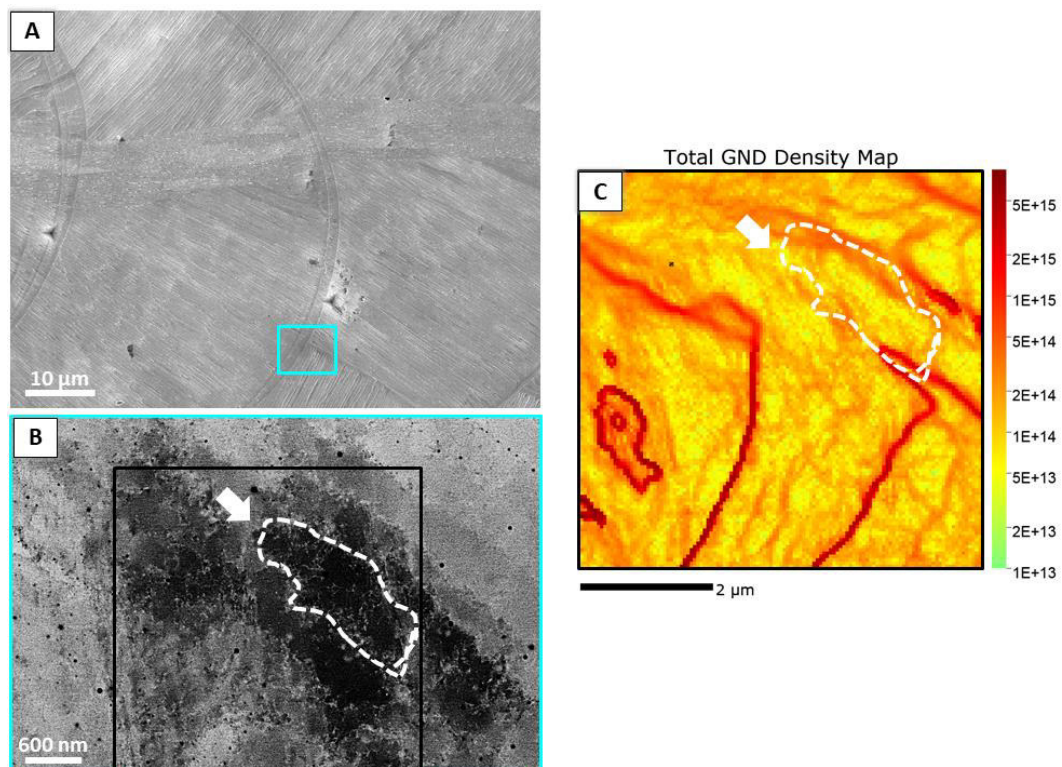
Source: Author

Figure 26 shows an analyzed region along a melt pool boundary for the bulk 0R specimen, as observed in SEI and SE images and the GND density map obtained after remapping. The average GND density for the 0R and the 90R samples is $3.2 \times 10^{14} \text{ m}^{-2}$ and $4.1 \times 10^{14} \text{ m}^{-2}$, respectively, indicating similar GND densities for both scanning strategies, as also reported in Figure 25.

The CC-EBSD maps shows that regions with the highest dislocation density are found along low angle boundaries where the GND density is as high as 10^{16} m^{-2} , Figure 25 and 26c (highlighted by a white arrow). In the same figures, other regions of high GND are found with values around $3 \times 10^{14} \text{ m}^{-2}$, while the lowest density regions have a GND density of $9 \times 10^{13} \text{ m}^{-2}$.

The latter regions are related to dislocation cell interiors (within the white dashed line in Figure 26c), while the regions with high GND density ($3 \times 10^{14} \text{ m}^{-2}$) are around 400 nm apart and coincide with dislocation cell walls (shown by white dashed line in Figure 26c).

Figure 26 – (a) SE image from the etched sample. (b) Highlighted region in (a) along a melt pool boundary, shown by ECCI. (c) Total GND density from the region highlighted by a black rectangle in (b). BD is parallel to the scale bar in all images. The white arrow indicates a LAB, while the dashed white line indicates a dislocation cell boundary. SE: secondary electrons; ECCI: electron channeling contrast imaging; GND: geometrically necessary dislocations. BD: building direction. LAB: low angle boundary.



Source: Author

5.1.2 Residual stresses

Residual stresses are present in several length scales. In this section, we focus on type I and III. Initially, the type I residual stresses are compared between the last consolidated layer and the middle cross section to link the residual stress behavior with the formation of dislocation cells (see Figure 24). These residual stresses are also compared between both scanning strategies to understand the role of dislocation cells in relieving such stresses.

Finally, type-III residual stresses measured by CC-EBSD are shown to understand how residual stress are distributed and correlated to the formation of dislocation cells in LPBF alloys.

5.1.2.1 Macroscopic (type I) residual stress

The difference in residual stresses is created by a dissimilar thermomechanical history. In our study, all process parameters are kept constant except the scanning strategy, i.e., the employed rotation between layers. Figure 28 summarizes the residual stresses (type I - macroscopic) measured on the top cross section in the as-built condition and following electrochemical polishing. Compressive stresses are defined as negative stress value, whereas tensile stresses are defined by positive values.

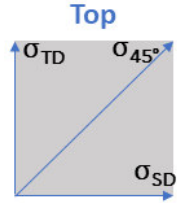
In Figure 27, the residual stresses on the BD top surface are higher along the SD due to a higher constraint from previously solidified material along this direction (KRUTH et al., 2012; STRANTZA et al., 2019). For example, along TD, a powder-bed found aside the melt pool creates weaker constraints and lower cooling rates (PARRY; ASHCROFT; WILDMAN, 2016). According to the thermal gradient mechanism (TGM), the zones heated and molten by the laser shrink and create tensile stresses (MIRKOOHI et al., 2021), observed in Figure 28. Additionally, the residual stresses are higher for the 0R specimen than the 90R scan for both the SD-TD and the principal stresses coordinate systems. In both cases, the direction of the principal stresses deviates from the SD-TD experimental frame by 14-39°. In other words, residual stresses are not the highest along the scanning direction in the BD top surface.

Solidification cells growing from the melt pool sides solidify slightly tilted to both the melt pool center and the scanning direction along the scanning direction (WEI; MAZUMDER; DEBROY, 2015). As seen in Figures 20a and 20b, cells growing from the melt pool side dominate the microstructure. Therefore, the 14-39° deviation of the principal stresses from the scanning direction may arise from the unequal solidification condition along a single track. Since the melt pool is only constrained by the consolidated material at one side (PARRY; ASHCROFT; WILDMAN, 2016), an asymmetry in the residual stress distribution may arise. The tilted solidification cells from the constrained side dominate the residual stresses, resulting in a similarly tilted principal stress direction.

If both sides are surrounded by a powder bed or a consolidated medium, the scanning direction may be the principal stress direction. The use of a bidirectional scan may also aid at balancing the asymmetric distribution of residual stresses, thus leading to $SD \parallel \sigma^{P_{11}}$.

When comparing the stress level between the as-built surface and at 250 μm beneath the surface, the as-built surface shows higher residual stresses than beneath the surface. This effect is more pronounced for the 90R specimen. The electropolished surfaces represent the second last consolidated layer. In this case, the influence of loose powder attached to the as-built surface is discarded, as it would lead to reduced residual stresses in the as-built state (MISHUROVA et al., 2017, 2019), contradicting the observed trend.

Figure 27 – Residual stresses analyzed on the top cross section in the as-built condition and after electropolishing. σ_{SD} : residual stresses along the scanning direction; σ_{TD} : residual stresses along the transverse direction; σ_{45} : shear residual stresses measured at 45° from the scanning or transverse direction; S_{11} and S_{22} : principal stresses. $\Delta\phi$: angle between the S and P systems, i.e., angle between the SD-TD measurement frame and the coordinate system of principal stresses.



	Top			
	0R		90R	
	As-built	Polished	As-built	Polished
σ_{SD} (MPa)	309 ± 20	286 ± 26	345 ± 20	115 ± 16
σ_{TD} (MPa)	201 ± 49	62 ± 19	170 ± 29	89 ± 12
σ_{45} (MPa)	337 ± 23	277 ± 28	306 ± 38	160 ± 16
S_{11} (MPa)	353	326	358	161
S_{22} (MPa)	216	187	311	48
$\Delta\phi$ (°)	28	21	14	39

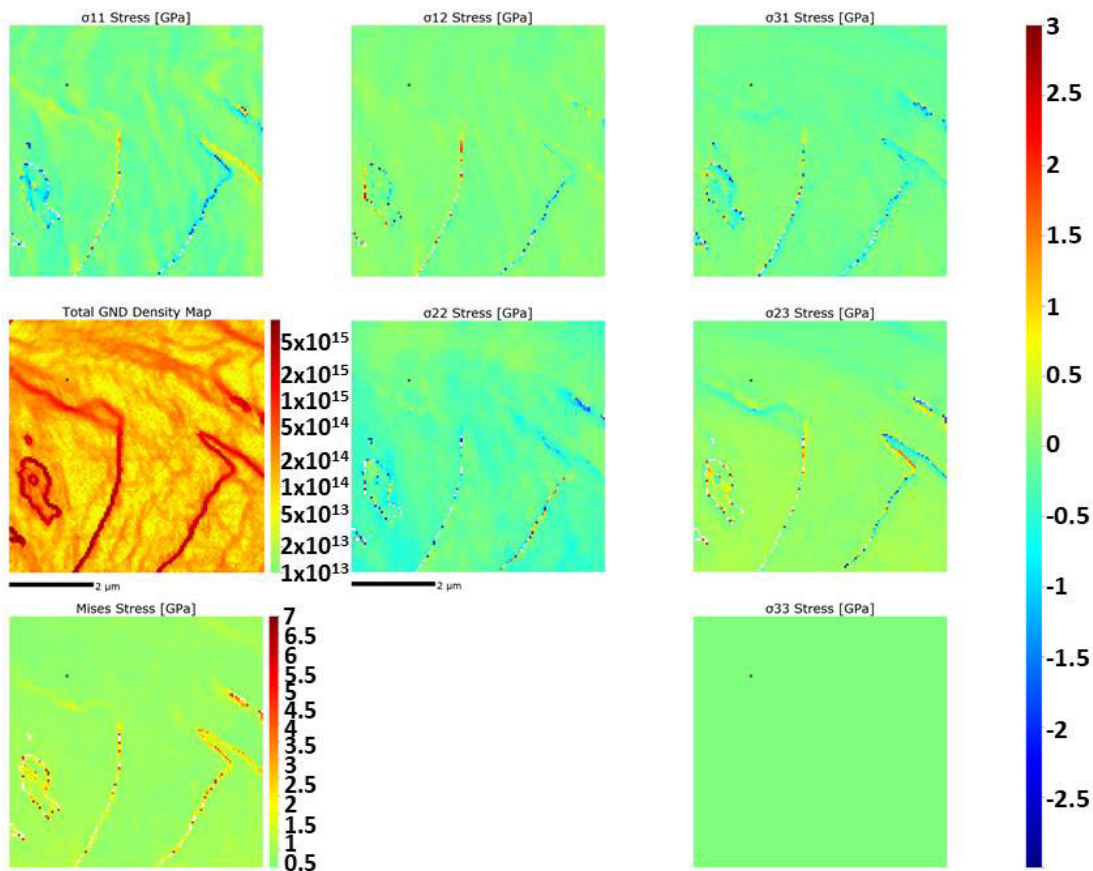
Source: Author

5.1.2.2 Intragranular (type III) residual stresses

Besides the type I residual stresses, type III intragranular residual stresses were analyzed by CC-EBSD, as shown in Figure 28. Observing the σ_{11} and σ_{22} normal stresses, regions presenting compressive and tensile stresses alternate along the measured surface in a lower magnitude (-0.3 GPa vs 0.3 GPa) for a finer scale of around 500 nm. This same trend is found with higher magnitude (-1.5 GPa vs 1.5 GPa) in a coarser scale around 2 μm . The first is related to dislocation cells, while the latter regards to low angle boundaries. Such substructure pattern is created to ensure a compatible deformation between regions with different plastic activity (HANSEN, 1990; MUGHRABI, 2006).

In this case, regions presenting high Von Mises stress coincide with the areas showing high a GND density.

Figure 28 – Total GND density and residual stresses measured by CC-EBSD from the same region shown in Figure 6. BD is parallel to the scale bar. The color scale bar for the GND density and Von Mises stress is shown beside the map. For all others residual stress maps, the larger color scale on the right side is used. GND: geometrically necessary dislocations; CC-EBSD: cross-correlation electron backscatter diffraction; BD: building direction.



Source: Author

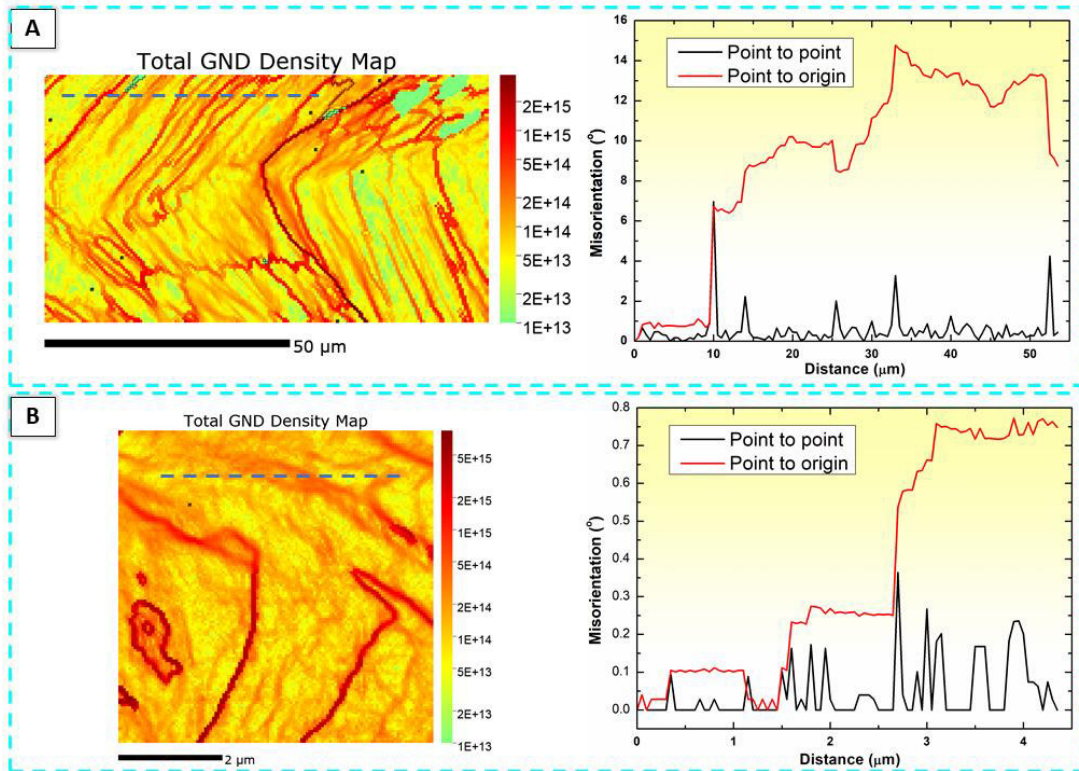
5.1.3 Misorientations

Due to the rapid solidification microstructure and the inherent plastic strain from the constrained solidification, misorientation builds up as the solidified grain grows (POLONSKY et al., 2020). Figure 29a reveals the misorientation profile for the indicated line in a larger map in the BD x TD cross section from the 0R specimen. Figure 29b indicates the same profile in a finer scale in the 0R specimen. The misorientation building as the grain grows is clear in Figure 9a. However, it is not built in a continuous and cumulative manner. By observing Figure 29a and Figure 29b, point-to-origin (blue) misorientation is accumulated around each 2-3 μm , although point-to-point (red) misorientations are found each ~ 300 nm. Point to point misorientation profile in Figure 29b depicts the misorientation values between 0.1 to 0.25 $^\circ$. Considering a dislocation array as being responsible for this misorientation, we calculated the dislocation spacing as 40-100 nm. From ECCI results, we estimated the cell-wall thickness to be around 70 nm. If we now consider a rectangle of 100 nm \times 70 nm, which contains 2 dislocations (average value from intercept number from ECCI images), the GND density becomes $\sim 3 \times 10^{14} \text{ m}^{-2}$. This is similar to the values obtained using CC-EBSD and therefore validates the GND density estimation using this method.

5.1.4 – Residual stresses and dislocation structures

While most of the studies have been focusing on the influence of process parameters on residual stresses induced by thermal shrinkage or cooling (AHMAD et al., 2018; BARTLETT et al., 2018; MUGWAGWA et al., 2019; SIMSON et al., 2017), the residual stress accommodation and relief by the underlying solidification structure is barely considered (NADAMMAL et al., 2017; SERRANO-MUNOZ et al., 2020a, 2020b). Figure 23a and 23b show that the dislocation densities increase from the last consolidated layer ($\rho = 2.1 \times 10^{13} \text{ m}^{-2}$) to the second last consolidated layer ($\rho = 4.1 \times 10^{14} \text{ m}^{-2}$) in the 90R sample. Simultaneously, residual stresses are significantly reduced from the last to the second last consolidated layer (see as-built and polished cross sections in Figure 28). This coincides with dislocation cells becoming more defined (thinner walls and more organized structures) and displaying higher dislocation densities (both overall and at dislocation cell walls).

Figure 29 – GND density map and the indicated misorientation profile (dashed in blue) for the 0R specimen in (a) a coarse scale CC-EBSD map with step size of 500 nm and a (b) fine scale CC-EBSD map (step size: 50 nm). These maps were obtained from the 0R specimen. It shows dislocation cells as incidental dislocation boundaries and LAB as geometrically necessary boundaries due to the cumulative misorientation. GND: geometrically necessary dislocations; CC-EBSD: cross correlation – electron backscatter diffraction; LAB: low angle boundaries.



Source: Author

These observations suggest that the thermal energy provided by the intrinsic heat treatment creates a higher dislocation density. It occurs as a consequence of the relief of thermal stresses created during heating and cooling cycles via plastic strain when the yield stress of the material is surpassed (SABZI et al., 2020; SERRANO-MUNOZ et al., 2020b). The yield stress is dramatically reduced at the processing temperatures typically employed in AM (RAHIMI et al., 2016). This interaction between residual stress relief by plastic strain occurs mainly during the first cycle, when the first layer is deposited onto the previous one, as will be discussed in Section 5.1.5. The relief of residual stresses above the yield stress by plastic strain, where dislocations are nucleated and rearranged, has already been reported in the literature (SERRANO-MUNOZ et al., 2020b; ZHANG et al., 2016). In this case, the effect of plastic strain surpasses the effect of recovery. During further building, dislocation patterns and density remain approximately constant.

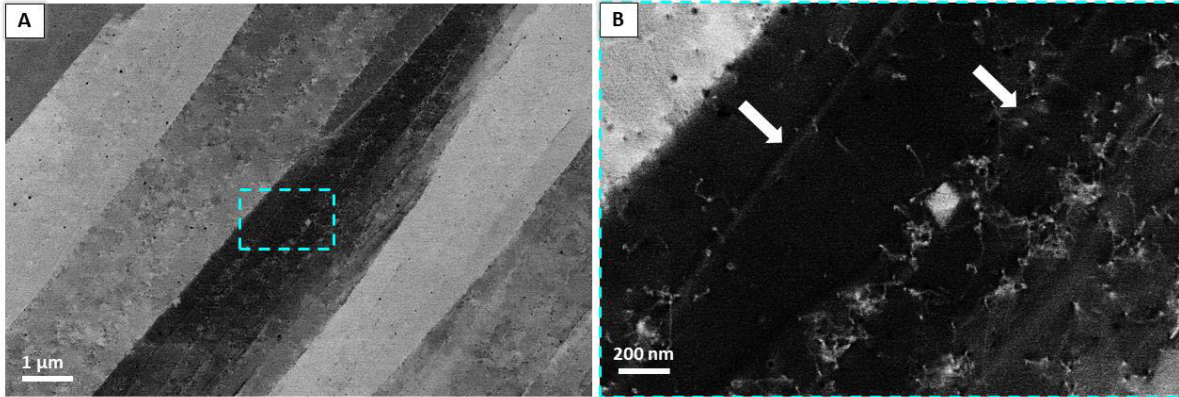
Although our results and discussions on this topic were focused on the 90R sample, the relief of residual stresses by dislocation emission and rearrangement is also valid for the 0R scanning strategy. The same concept can be applied to other single-phase alloys, which do not undergo solid-state phase transformation, and other scanning strategies. When observing the average and local dislocation densities, a higher dislocation density is observed for the 0R specimen in all cases, as well as a finer cell size with higher cell wall fraction. This indicates stronger plastic activity (HANSEN, 1990) when compared to the 90R specimen. A favorable stronger crystallographic texture and coarser grain size (Figure 20a) may also aid plastic deformation in the 0R scan (SERRANO-MUNOZ et al., 2020b). Therefore, given the higher residual stresses formed due to the stronger heat accumulation (ULBRICHT et al., 2020) in the 0R scan, plastic deformation took place more intensively than in the 90R scan. The residual stresses in the 0R specimen are too high to be completely relieved by plastic deformation.

5.1.5 – Theories for the dislocation character and dislocation structure evolution during LPBF

The absence of dislocation cells in the last consolidated layer is observed when compared to the cellular structure found in the second last consolidated layer (Figure 23a and 23b). In fact, solidification cell boundaries are clearly visible in Figure 30 and do not coincide with dislocation cells in the last consolidated layer, whereas they coincide in other layers (Figure 23b and Figure 24).

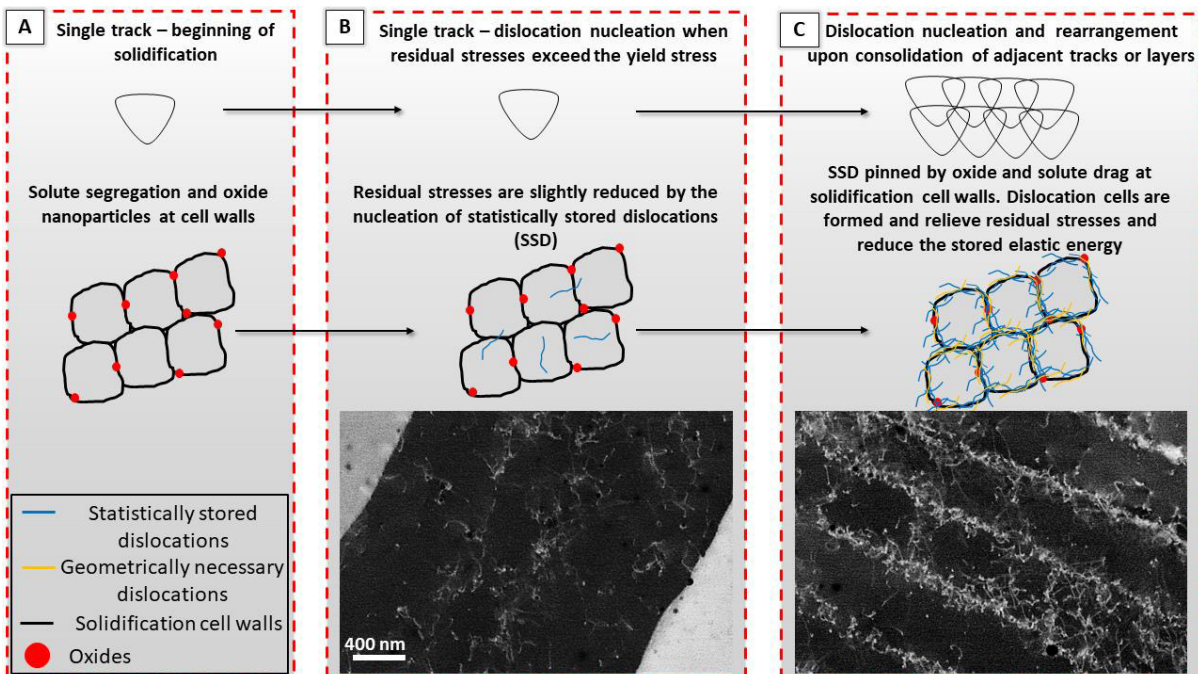
To explain and link this behavior with the solidification structure evolution upon solidification, we adapt the composite model (MUGHRABI, 2001, 2006), where statistically stored dislocations (SSD) are formed due to thermally induced strain in a constrained medium (BERTSCH et al., 2020). A local variation of SSD density arises due to the pinning by oxide particles (VOISIN et al., 2021) and microsegregation (BERTSCH et al., 2020) present along solidification cell walls, resulting in the coincidence of dislocation and solidification cells. This local variation of SSD density creates gradients of local flow stress, which is redistributed by geometrically necessary dislocations (GND) (MUGHRABI, 2001). This behavior is confirmed by the alternating positive and negative residual stress between dislocation cells and across LABs in Figure 29.

Figure 30 – (a) Solidification cells from the last consolidated layer. (b) Enlarged view in cyan from (a). Note that solidification cell boundaries, highlighted by white arrows, are visible, while dislocation cells are not observed. A few dislocations accumulate at solidification cell walls when only a single layer is consolidated. This non-uniform distribution of SSD aids the formation of dislocation cells upon intrinsic heat treatment (see schematics in Figure 30).



Source: Author

Figure 31 – Schematics of the dislocation structure evolution in LPBF alloys. (a) Solidification cells show solute segregation and oxide nanoparticles along their walls. (b) The constrained expansion and shrinkage create statistically stored dislocations (SSD) and slightly reduces the residual stresses. (c) Upon intrinsic heat treatment, more SSDs are nucleated and pinned by oxide nanoparticles and solute drag along solidification cell walls, resulting in the coincidence of dislocation and solidification cells. Geometrically necessary dislocations redistribute stresses due to the heterogeneous distribution of SSDs. The nucleation of dislocations and the formation of dislocation cells relieve residual stresses.



Source: Author

This ensures and aids the compatible deformation of neighboring regions of local different flow stress, i.e., cell wall and cell interior (MUGHRABI, 2001). Such interaction predominantly occurs during the intrinsic heat treatment. This interaction sequence is illustrated in Figure 31.

The SSD density is calculated based on the subtraction of the total dislocation density measured by ECCI by the GND density measured by CC-EBSD. An adequate step size (50 nm) was used in CC-EBSD to ensure the identification of dislocation cells (between 350-450 nm – Table 3). Coarser step sizes would not allow this visualization and would result in a decreased GND density (JIANG; BRITTON; WILKINSON, 2013). Except in the low angle boundaries, SSD densities are usually higher than GND densities. However, GNDs play a key role in creating deformation-induced long-range internal stresses and lattice misorientations (MUGHRABI, 2001). This leads to tension-compression asymmetries, i.e., Bauschinger effect (CHEN et al., 2019c), due to forward and back stresses at cell walls and cell interiors, respectively. The values of the shear stress τ created by dislocation cells are calculated as 132 MPa and 97 MPa for the 0R and 90R specimens, respectively. These values are near the difference of ~60 MPa in yield stress between tension and compression tests in a similar alloy, where different process parameters are employed (CHEN et al., 2019c). In this reference (CHEN et al., 2019c), the employed process parameters should yield lower plastic strain, thereby inducing less defined dislocation cells with lower dislocation densities. This would also result in lower long-range stresses. Therefore, it is likely that dislocation cells are responsible for the tension-compression asymmetry observed in LPBF alloys.

When investigating the origin of dislocations upon mechanical loading of LPBF alloys, they are nucleated at dislocation cell walls (WANG et al., 2017) due to the forward stresses, as predicted by the composite model (MUGHRABI, 2001). Besides, these interfaces are also stress concentration sites (created by pinned dislocations). The local stress is higher than the global value, triggering the earlier plastic activity at these sites. The local flow stresses at cell interiors and walls are calculated and, in both scanning strategies, a ~95 MPa difference in stress is observed between both regions. This clearly indicates the forward stresses created at cell walls. As observed in Figure 29, point-to-origin misorientation is only accumulated after crossing a LAB (between subgrains).

Dislocation cell walls show non-cumulative misorientation up to 0.25° (CIZEK et al., 2004), creating random fluctuations, which suggest that they are incidental dislocation boundaries (IDB) (HUGHES; HANSEN; BAMMANN, 2003; KUHLMANN-WILSDORF; HANSEN, 1991). Such structures play a key role upon solidification, ensuring elastic energy minimization (by reducing dislocation density and organizing such defects) (KUHLMANN-WILSDORF; HANSEN, 1991) and stress redistribution (MUGHRABI, 2001). The second factor is the most important upon additive manufacturing, as the compatible deformation of dislocation cell walls and interiors is ensured, avoiding further stress concentration.

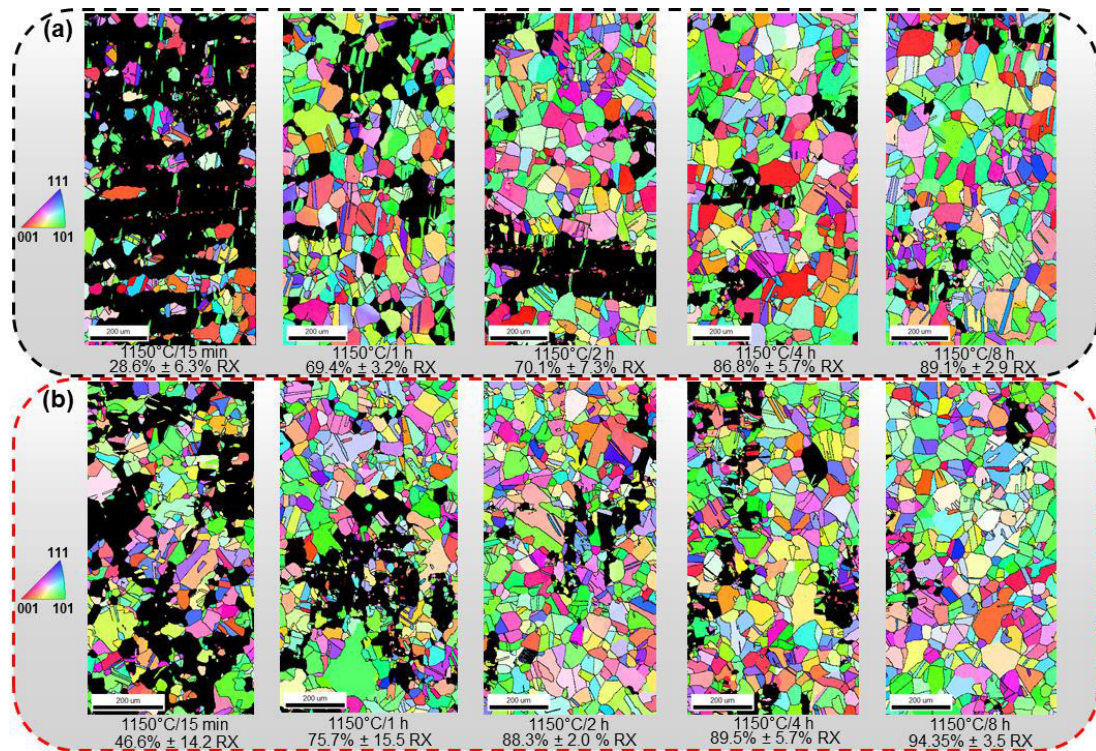
LABs are geometrically necessary boundaries and ensure a compatible deformation between regions with different plastic activity, i.e., subgrains (HUGHES; HANSEN; BAMMANN, 2003; KUHLMANN-WILSDORF; HANSEN, 1991). They also accommodate the deformation created by the mutual encountering of two solidification fronts, displaying slight different growth directions ($\theta < 15^\circ$). LABs show a higher GND density in the 90R sample (Figure 24d) compared to the samples processed under the 0R scanning strategy. LABs carrying more misorientation and higher GND densities in the 90R scan occurs probably due to: (1) the lower energy minimization created by the dislocation cells in this scanning strategy. (2) A higher misorientation between two meeting solidification fronts due to the less favorable directional growth when rotation is applied between layers. (3) A higher LAB fraction in the 0R scan (68.3% of all boundaries for the 0R scan whereas 59.3% for the 90R), where more LABs share the misorientations created upon solidification.

For LPBF specimens, the low energy dislocation structure theory predicts dislocation cells as the main strengthening mechanism when compared to the subgrains (bounded by LAB) due to their finer size (KUHLMANN-WILSDORF; HANSEN, 1991). This fact agrees with the existing experimental evidences on the dislocation cells as the main strengthening mechanism in LPBF alloys (HONG et al., 2021; LI et al., 2020; LI; HE; GUO, 2020; WANG et al., 2017). It must be stressed that GNDs are also found in incidental dislocation boundaries, creating low misorientations. However, the Burgers vector from dislocations located at each cell wall is mutually cancelled, i.e. the net Burgers vector is zero, resulting in a non-cumulative misorientation (HUGHES; HANSEN; BAMMANN, 2003).

5.2 – Annealed condition

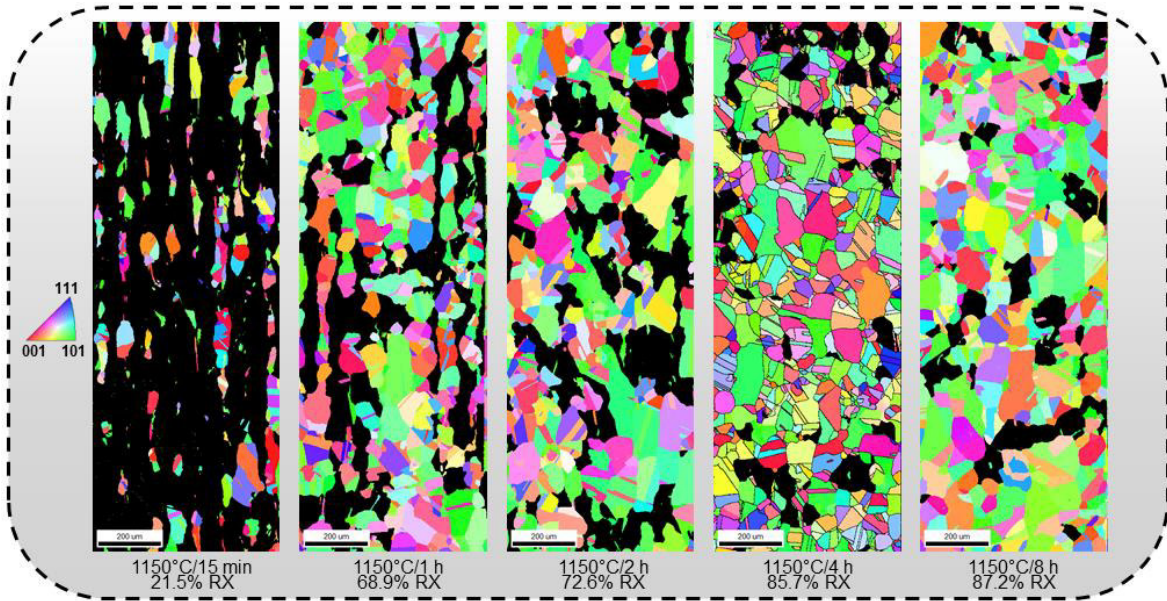
The evolution of primary recrystallization after isothermal annealing at 1150°C for different times is shown in Figure 32a for the unidirectional scan and Figure 32b for the 90°-rotation scan. Such grains were defined as those having grain orientation spread (GOS) values smaller or equal to 2°. In both cases, a non-uniform recrystallization is observed at 1150°C/15 min (Figure 32a and 33b). Recrystallized grains preferentially nucleate along $\langle 100 \rangle \parallel$ BD tracks, which present the highest KAM, and, therefore, the higher GND density as depicted in Figure 20b. A sluggish recrystallization kinetics is observed for both cases as indicated by the recrystallized volume percentage shown below each map in Figure 32. The IPF map from other cross sections is shown in Figures 34 and 35 for the 0R specimen and Figure 35 for the 90°-rotation scan. A remarkable difference in kinetics can be noticed by using different scanning strategies as the unidirectional scan present the most sluggish kinetics.

Figure 32 – IPF maps for the recrystallized grains in (a) unidirectional and (b) 90° rotation scans for different annealing times at 1150°C. Recrystallized grains are defined here to have a grain orientation spread (GOS) smaller or equal to 2°. The volume fraction of recrystallized grains is also shown. These values are calculated based on the average values from all investigated cross sections (3 for the unidirectional scan and 2 for 90°-rotation).



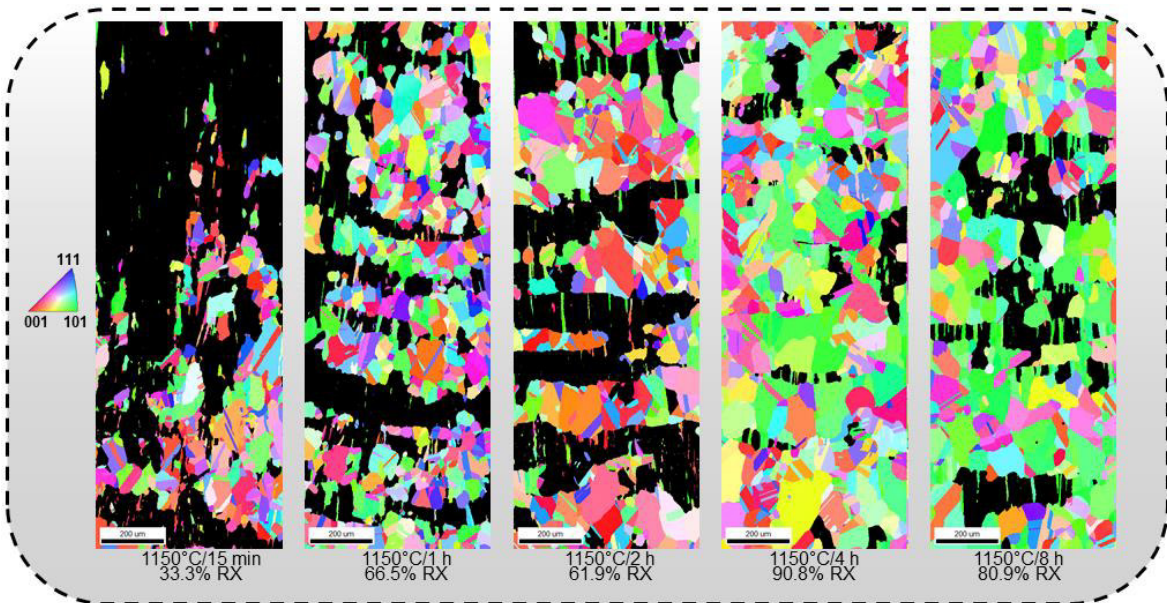
Source: Author

Figure 33 – IPF from the BD x TD cross section for the unidirectional scan at different annealing times (1150°C).



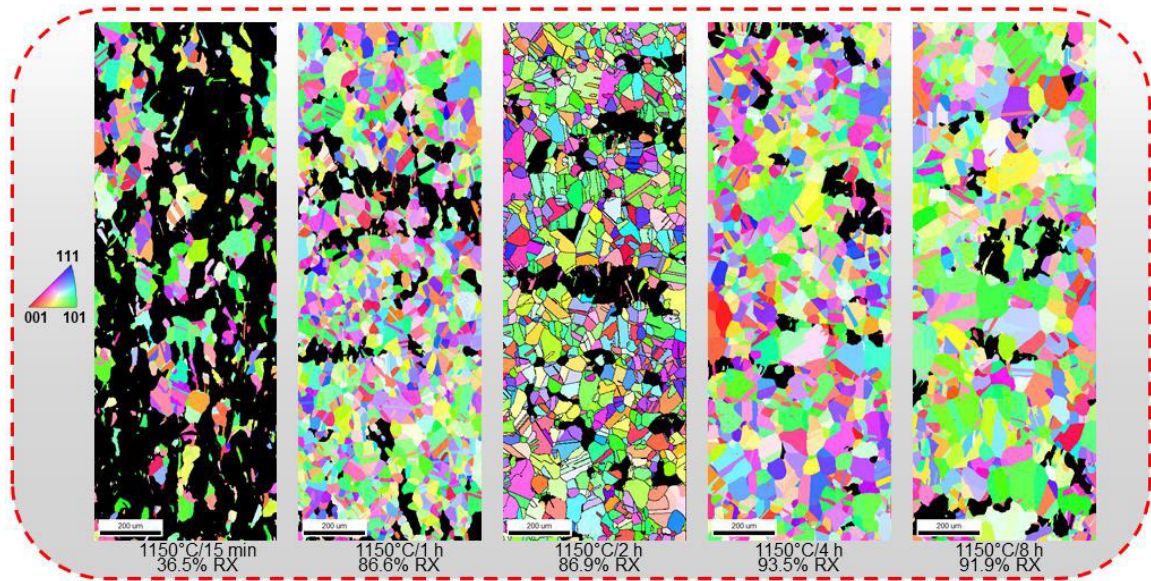
Source: Author

Figure 34 – IPF for the BD x SD cross section for the unidirectional scan at different annealing times (1150°C).



Source: Author

Figure 35 – IPF for the side cross section for the 90°-rotation sample annealed at 1150°C for different times.

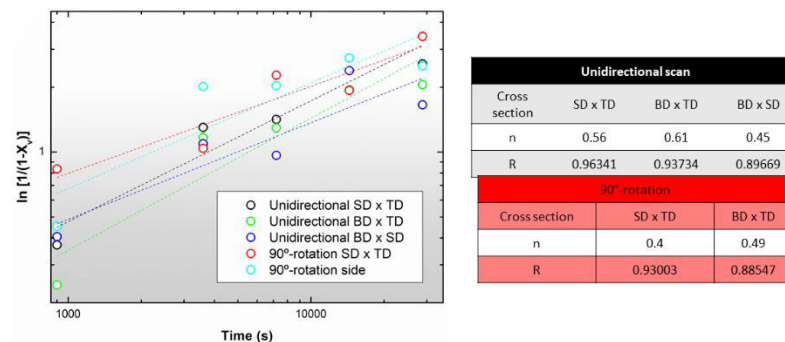


Source: Author

Aiming at quantifying the recrystallization kinetics, JMAK plots were obtained and the results are displayed in Figure 36. Low correlation coefficients ($R = 0.93248$ for the unidirectional scan and $R = 0.90778$ for the 90°-rotation scan) were obtained for both cases, indicating a poor description of the recrystallization kinetics. Besides, a low Avrami coefficient n is obtained for both conditions ($n = 0.54$ for the unidirectional scan and $n = 0.44$ for the 90°-rotation scan), indicating a deviation from the ideal conditions assumed by the classical JMAK model.

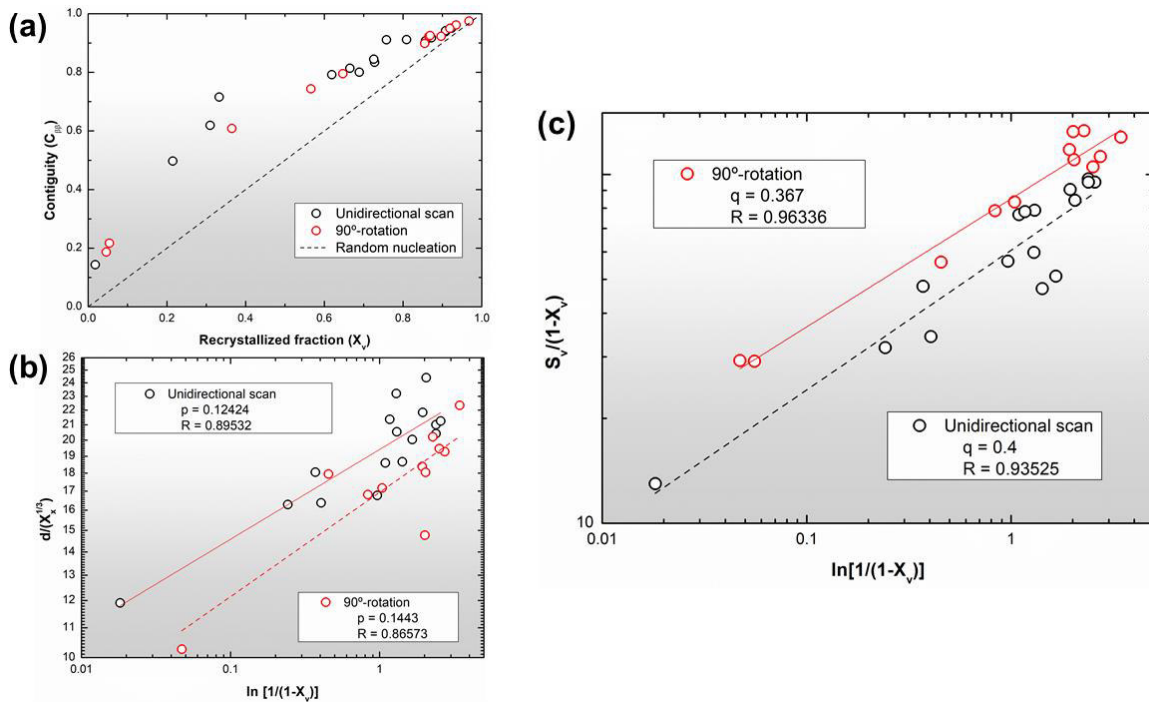
Grain contiguity, shown in Figure 37a, is defined as the fraction of the total grain boundary shared between recrystallized grains upon impingement (RIOS *et al.*, 2006). Random nucleation leads to the equality between the contiguity $C_{\beta\beta}$ and X_v , while positive deviations, such as the ones observed for both scanning strategies indicate clustering of recrystallized grains (VANDERMEER, 2005).

Figure 36 – JMAK plot for all cross sections from the unidirectional and 90°-rotation scans.



Source: Author

Figure 37 – (a) Grain contiguity, (b) p parameter and (c) q parameter from the microstructural path method indicating the clustering degree in recrystallization nuclei. All data was obtained from 3 different cross sections for the unidirectional scan, while 2 different cross sections were used for the 90° rotation.



Source: Author

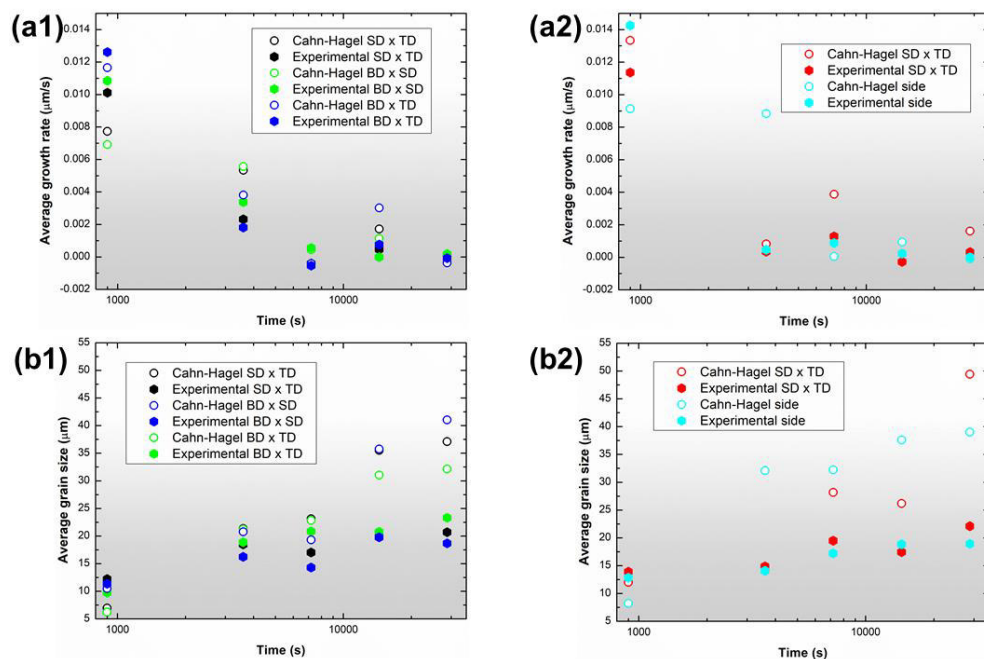
By applying the microstructural path method (MPM), two different parameters p and q are used to describe the extent of impingement of recrystallized grains (VANDERMEER, 2005; VANDERMEER; MASUMURA; RATH, 1991). Both parameters are shown in Figures 38b and 38c, respectively, for the two employed scan strategies after investigating several cross sections.

The p parameter indicates random nucleation, linear impingement and planar impingement for values equal to 0, 0.167 and 0.667, respectively. The q parameter, however, has values of 0.667, 0.5 and 0 for the same conditions, respectively. These parameters show a similar behavior as both scanning strategies lead to linear impingement, but the 90°-rotation scan values are farther from the theoretical value, indicating their deviation from this impingement pattern.

The average growth rate of all investigated cross sections was calculated based on the Cahn-Hagel method and compared to the experimental values for the unidirectional and the 90°-rotation scans in Figures 39a1 and 39a2, respectively. The average growth rate is roughly independent of the analyzed cross section except the initial 15 min. For all other annealing times, the standard deviation is around 10^{-4} $\mu\text{m/s}$.

The most striking feature for both scanning strategies is the recrystallized grain stagnation after 2 h annealing for both scanning strategies due to their mutual grain impingement. The 90°-rotation scan shows a slightly higher growth rate between 4-8 h. The average growth values for the present material are considerably lower than values reported on the literature for pure copper (LIN *et al.*, 2018; VANDERMEER; JENSEN, 1994, 1995) and an Al alloy (VANDERMEER; JUUL JENSEN, 2003) due to the occurrence of both orientation and Zener-Smith particle pinning in the studied alloy. The final grain sizes are also overestimated by the Cahn-Hagel method since they do not account for twinning events during recrystallization. Observing the experimental results, the recrystallized grain size expands with a sluggish kinetics.

Figure 38 - Average growth rate from experimental and Cahn-Hagel methods for the (a1) unidirectional scan and (a2) 90°-rotation. Average grain size obtained experimentally and estimated based on the Cahn-Hagel method for the (b1) unidirectional scan and (b2) 90°-rotation.



Source: Author

5.2.1 Differences in microstructure and recrystallization kinetics

Using a unidirectional scan (Figure 20a) and applying a 90°-rotation between layers (Figure 21a) create distinct patterned microstructures. Upon annealing, significant differences in the recrystallization behavior are found depending on the initial as-built microstructure. For example, the distribution of recrystallization nuclei is rather heterogeneous for the unidirectional scan and coincides with regions with initially higher GND density values, as noticed when one compares Figures 20b1 and 28a1.

The determination of the recrystallization kinetics using the JMAK theory fails since it assumes idealistic assumptions such as homogeneous (random) nucleation, constant boundary migration velocity and isotropic growth (HUMPHREYS; HATHERLY, 2004a). For real materials, these assumptions are not fulfilled (JÄGLE; MITTEMEIJER, 2011), and the problem is intensified in complex microstructures. This theory uses only one microstructural descriptor, i.e., the recrystallized volume fraction (X_v).

A better description can be provided by using the microstructural path method (MPM) (VANDERMEER; MASUMURA, 1992; VANDERMEER; MASUMURA; RATH, 1991) based on two microstructural descriptors, namely the recrystallized volume fraction (X_v) and the density of boundaries separating recrystallized from non-recrystallized grains (S_v) (VANDERMEER, 2005). Although the initial MPM model assumed random nucleation (HUMPHREYS; HATHERLY, 2004a), new partial path functions have been evolved to better describe the grain impingement pattern, such as the q and p parameters calculated as described in refs. (VANDERMEER, 2005; VANDERMEER; MASUMURA; RATH, 1991).

As noticed in Figures 38b and 38c, the p parameter shows a lower correlation coefficient than the q parameter. Comparing to the microstructures from Figures 33a and 33b, the p parameter contradicts the observed trend since this parameter indicates a stronger tendency for linear grain impingement when employing a 90°-rotation. In this case, we suggest the q parameter for a more precise microstructural description in such complex microstructure since it is based on two microstructural descriptors: S_v and X_v while the p parameter is based solely on X_v .

The q and p parameters obtained for 3 different cross sections (each for a different plane) for the unidirectional scan and for 2 different cross section (from BD x TD and SD x TD planes) when employing a 90°-rotation scan reveal a similar trend for both cases, i.e., linear impingement of recrystallized grains. As discussed previously, the q parameter better describes the impingement pattern. From this parameter, although both scanning strategies display linear impingement, the 90°-rotation results in values farther from the ideal value for such impingement pattern (0.4 for the unidirectional scan and 0.367 for the 90° rotation vs. the ideal 0.5).

By observing the recrystallized microstructures in Figure 32a and Figures 34 and 35, an apparently planar impingement along the initially $\langle 100 \rangle \parallel$ BD grains with higher GND density can be inferred due to the linear streak in both views. However, the linear strings are more constant on the SD x TD than in the BD x TD plane which would create a grain linear impingement before a (2-D) planar impingement. In fact, the values of the q parameter indicate a linear impingement tending to a planar impingement. A more continuous linear impingement along a single track is expected due to the more intense variation in process conditions along several layers as observed in the BD x TD cross section.

This could be induced by local stochastic variation in powder spreading (CHEN *et al.*, 2019a), powder-bed denudation (BIDARE *et al.*, 2018), or melt pool flow (KHAIRALLAH *et al.*, 2016), as well as the inherent heat accumulation (ROMANO *et al.*, 2015), and orientation gradient building (POLONSKY *et al.*, 2020) during processing.

All these factors lead to a more heterogeneous microstructure along the BD (ZINOVIEVA *et al.*, 2020), which would create less defined impingement patterns for recrystallized grains than in the SD x TD cross section, explaining the tendency of linear patterning for unidirectional scan rather than a planar impingement. The linear impingement persists during the initial moments and the planar impingement occurs afterwards consuming the high GND density $\langle 110 \rangle \parallel$ BD grains.

The linear pattern created by the impingement restrains the final grain size along the SD. Following the initial impingement, those grains grow laterally along TD until they impinge with each other. As a result, the recrystallized microstructure remains with a linear pattern, as seen in Figure 32a (1150°C/8 h), since the driving pressure is not large enough to trigger grain growth at such temperature and in the presence of strong orientation and particle pinning.

For the 90°-rotation scan, a weaker tendency for linear impingement is found due to the chessboard pattern of grains containing higher GND densities. Yet, the p parameter mostly indicates a linear impingement pattern. This trend follows the one observed in the unidirectional scan. In each layer, recrystallized grains nucleate and preferentially sweep the centerline of the melt pools composed of $\langle 100 \rangle$ || BD grains along the SD for that layer, leading to linear impingement along these tracks. In that scenario, tracks rotated by 90° inherited from the previous layer show a weaker pattern formation regarding recrystallization. Therefore, many linear impingements form along a single layer in such a way that they are rotated by 90° between layers, resulting in more uniform microstructures.

After the initial linear impingement, the recrystallized grains sweep the remaining microstructure. Differently from the unidirectional scan, the larger number of recrystallization nuclei and its more uniform disposition leads to a finer grain size, as seen in Figure 38, since a smaller distance is available for the growing recrystallized grains until grain impingement. This more uniform distribution of recrystallization nuclei is responsible for accelerating the recrystallization kinetics and yielding a more uniform (non-patterned) recrystallization microstructure.

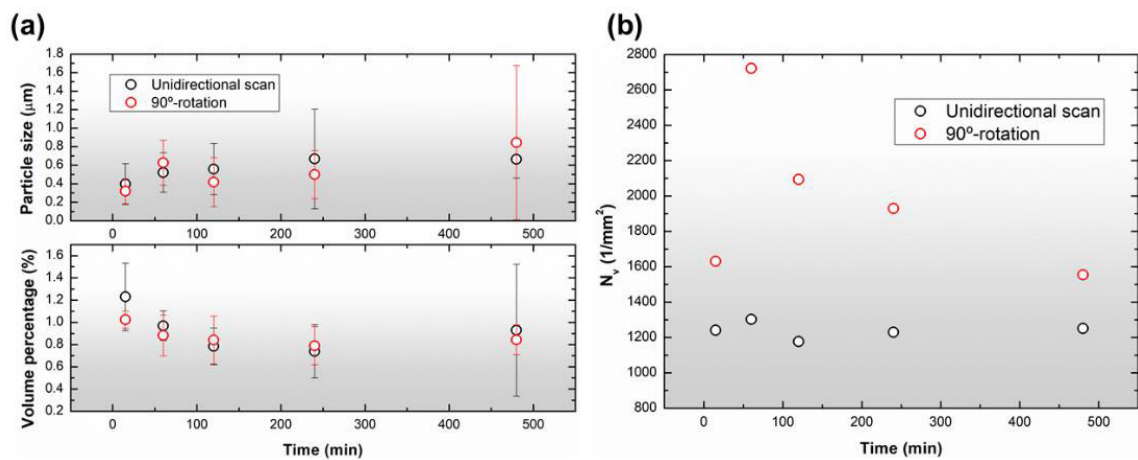
5.2.2 Factors influencing the recrystallization kinetics

Changing the scanning strategy directly affects the recrystallization kinetics. Considering the recrystallized fraction for each annealing time, the mean recrystallization rate is 0.84%/min for the unidirectional scan compared to 1.13%/min for the 90°-rotation scan. As shown in Figures 33a and 33b, the recrystallized volume fraction evolves significantly faster when applying a 90°-rotation between layers. Several factors could affect the annealing behavior in such a complex microstructure, including the presence of dispersed particles, dislocation density, recrystallization nuclei density, solute drag, and texture.

The particle size distribution and volume fraction are similar for both conditions during annealing, as shown in Figure 39a. Therefore, Zener-Smith particle pinning could not explain the dissimilar behavior on the kinetics alone. The 90°-rotation scan strategy allows for a higher recrystallization nuclei number density, as shown in Figure 39b.

Another remarkable difference is the evolution of recrystallization nuclei density during annealing. While the unidirectional scan generates a lower number of nuclei that remains constant during annealing (site saturation), the 90°-rotation scan leads to a higher density of nuclei. In the latter, grains are consumed during further annealing due to the larger driving pressure for normal grain growth (HILLERT, 1965).

Figure 39 - (a) Size and volume percentage of oxide particles and (b) Recrystallization grains density for both scanning strategies, unidirectional and 90°-rotation scans. The values from (b) are the average from 3 cross sections for the unidirectional scan, while 2 cross sections were analyzed for the 90°-rotation.



Source: Author

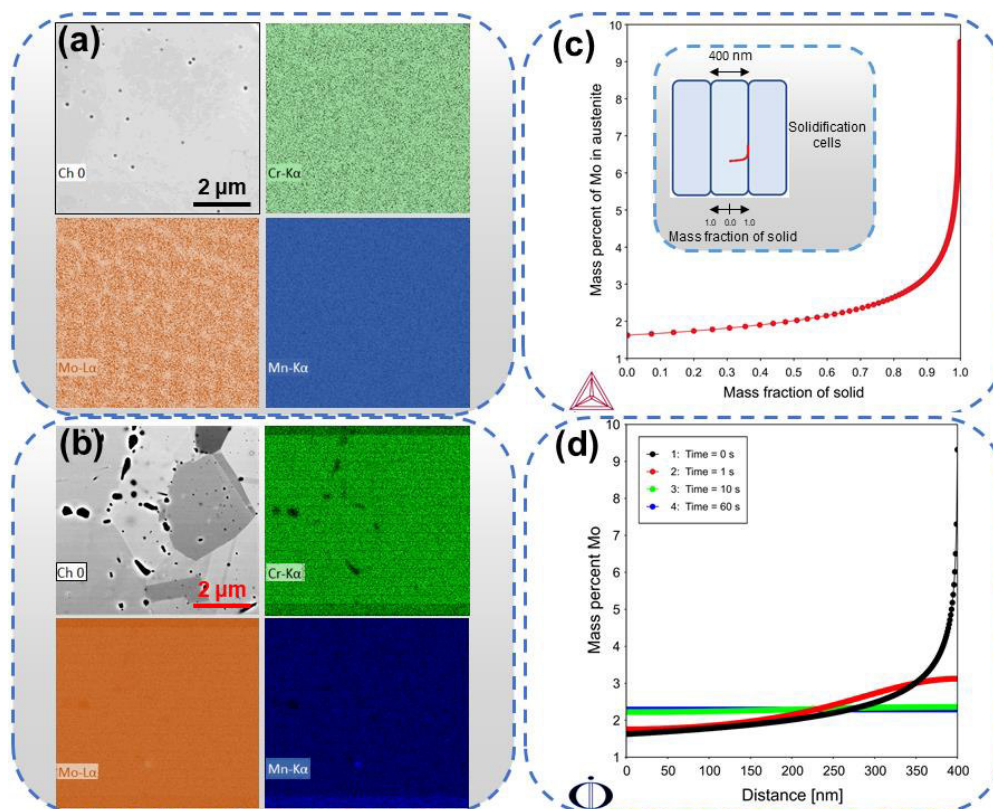
Solute drag also delays the recrystallization (LE GALL; JONAS, 1999). To investigate this hypothesis, EDS measurements were coupled with thermodynamic and kinetics simulations. As observed in Figure 40a, the initial as-built structure shows segregation of molybdenum along the cell walls. This strong microsegregation of molybdenum resulting from cellular solidification is expected and its extent was calculated using the Scheil-Gulliver model, the result of which is shown in Figure 40c. As the high cooling rates involved in the LPBF process promote a large undercooling of the melt, the solidification mode becomes austenitic (mode A), resulting in the absence of delta ferrite in the microstructure. For this reason, the BCC phase was set as dormant during the thermodynamic calculation.

The mass percentage of molybdenum in the austenite increases from 1.8%, in the first solid, to 9.7% in the last solidified regions, which become the cell walls. Assuming that solute segregation could affect the recrystallization kinetics up to 15 min, for example, this microsegregation profile was inputted into a DICTRA kinetic simulation.

A 400 nm linear region was created to simulate a solidification cell, as schematically represented in Figure 40c. The EDS analysis showed that all other metallic alloying elements (Cr, Mn, for example) are rather homogeneously distributed throughout the matrix, while Si, Al and O form the particle dispersion, therefore the cell chemical composition was defined according to Table 1, except for the Mo concentration.

As shown in Figure 40d, a chemically homogeneous matrix is obtained after annealing for about only 10 s. After annealing at 1150°C/15 min, results of EDS measurements show no chemical segregation in the austenitic matrix, as shown in Figure 41b. As expected from the kinetic simulation, the solute segregation inherited from the solidification (Figure 41a) disappears after annealing at 1150°C for 15 min. Therefore, solute drag due to a heterogeneous distribution of certain chemical species, particularly molybdenum, cannot explain the sluggish recrystallization kinetics at longer times.

Figure 40 - EDS elemental maps from the (a) as-built condition showing Mo segregation. (b) EDS after annealing at 1150°C/15 min showing no signs of elemental segregation in the austenite. (c) Scheil-Gulliver simulation showing the Mo microsegregation profile inside a solidification cell. The schematic representing the solidification cells is given with its size. The red curve in the inset represents the calculated Mo microsegregation profile (d) DICTRA simulation showing the Mo segregation profile after different annealing times at 1150°C.



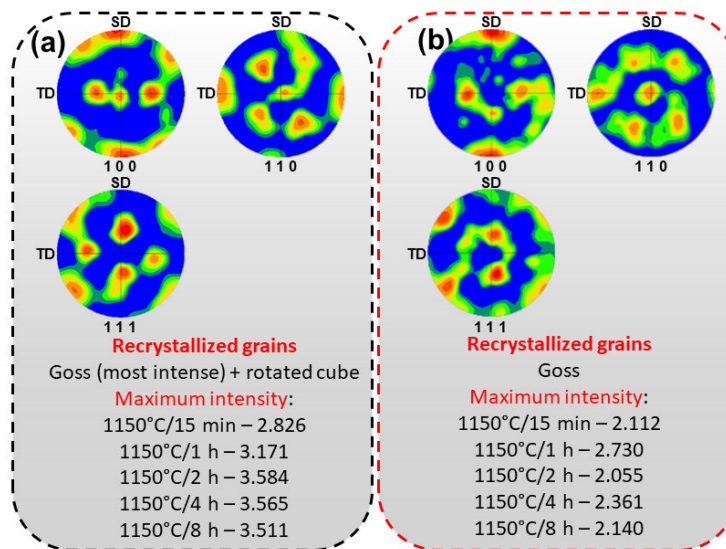
Source: Author

Comparing the initial dislocation densities, very similar values are found. In fact, the dislocation density measured by ECCI for the unidirectional scan is $5.7 \times 10^{14} \text{ m}^{-2}$ against $3.3 \times 10^{14} \text{ m}^{-2}$ for the 90° -rotation. This is controversial to the faster recrystallization kinetics found in the sample printed with a 90° -rotation scan, since a higher dislocation density increases the driving pressure for recrystallization (MOHAMED; BACROIX, 2000). Therefore, the difference in recrystallization behavior cannot be explained solely on a thermodynamics basis; rather, a kinetics factor plays a major role.

A significant difference in texture is noticed for both cases. The initial texture from Figures 23a and 23b reveal a remarkably stronger texture for the unidirectional scan in the as-built condition (11.402 for the unidirectional scan vs 4.641 for the 90° -rotation scan) Figure 41a and Figure 41b show pole figures for the recrystallized grains from unidirectional scan and the 90° rotation scan, respectively.

An overall texture weakening resulting from annealing twins (CHOWDHURY *et al.*, 2006) for both cases as the annealing proceeds. The unidirectional scan creates Goss $\{110\}\langle 100\rangle$ and Rotated Cube $\{100\}\langle 110\rangle$ texture components (maximum intensity 3.511), while the 90° -rotation scan creates a weaker Goss $\{110\}\langle 100\rangle$ texture component (maximum intensity 2.140). The presence of a stronger texture in the as-built condition and during further annealing for the unidirectional scan delays the recrystallization evolution due to orientation pinning. Therefore, lower recrystallization nuclei number density is the main factor dictating the difference in recrystallization kinetics between the unidirectional and the 90° -rotation scans.

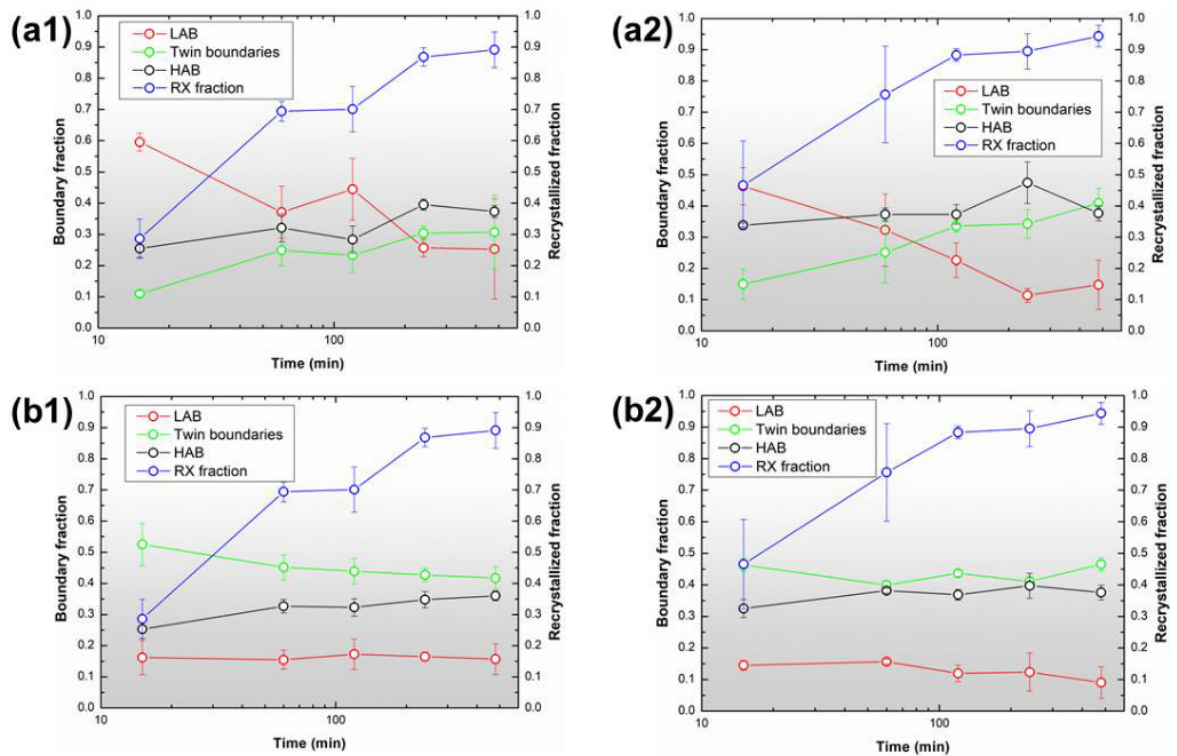
Figure 41 - Pole figures for the recrystallized grains in the (a) unidirectional scan and (b) 90°-rotation scan.



Source: Author

Observing Figure 42a2, for the 90°-rotation scan, it can be noticed a final recrystallized fraction equal to 0.95 and a number fraction of 0.41 of twin boundaries, a value similar to the grain-boundary-engineered AISI 316L stainless steel also processed by LPBF (GAO *et al.*, 2020), although no post-processing deformation was applied in our study. When comparing Figures 44b1 and 44b2, the recrystallized partition from unidirectional and 90°-rotation scans, respectively, the fraction of twin boundaries is initially higher for the unidirectional scan due to the multiple twinning events during the early stages of annealing, as shown in the twinning mechanism proposed below. However, as the recrystallized grains impinge themselves, more high angle boundaries form, reducing the twin boundary fraction. The high fraction of low angle boundaries between recrystallized grains (0.15) is caused by orientation pinning in the unidirectional scan, as shown in Figure 42a2. As seen in Figure 38a1, recrystallized grains expand through the matrix and grow until they impinge other grains after 2 h annealing. From this time on, the driving pressure for normal grain growth is marginally low due to the coarser grain size, as shown in Figure 38b. In contrast, the 90°-rotation scan yields a higher number of recrystallized grains, as seen in Figure 40b, due to the higher number of nucleation sites from the chessboard pattern. An initially higher high angle boundary fraction, as seen in Figure 42a2, than the unidirectional scan in Figure 42a1, provides a higher number of nucleation sites, as shown in Figure 40b.

Figure 42 – Grain boundary character distribution and recrystallized fraction for the (a1) unidirectional scan, (a2) 90°-rotation scan and the grain boundary character distribution considering only the recrystallized partition for the (b1) unidirectional scan and the (b2) 90°-rotation scan.



Source: Author

5.2.3 Recrystallization mechanisms

From the pole figures displayed in Figure 41, it can be noticed a common aspect for both conditions: texture weakening during the first 15 min of annealing. The reason for such condition is the abundant number of twinning events during the beginning of recrystallization, as shown in Figure 43a.

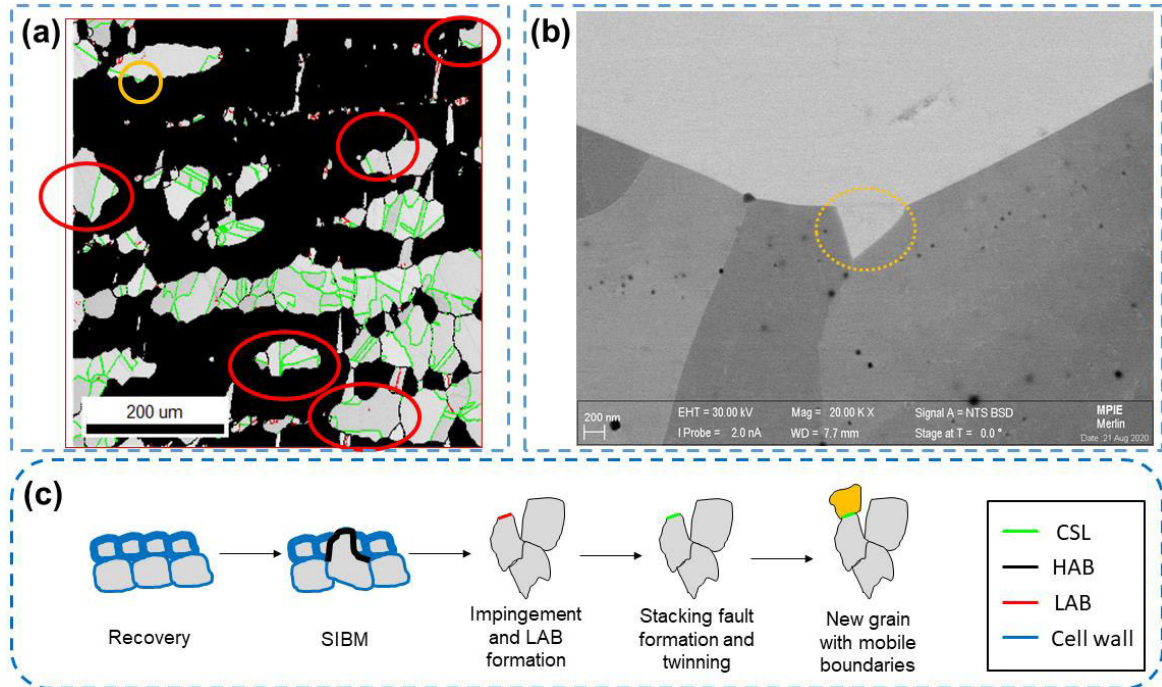
Recrystallized grains nucleate along the $\langle 100 \rangle$ || BD tracks or at their vicinities where the high dislocation density favors recrystallization kinetics. Although not investigated in our work, strain induced boundary migration (SIBM) is likely the main recrystallization nucleation mechanism, as observed in another study about recrystallization in LPBF-processed materials (ARIASETA *et al.*, 2020). Dislocations rearrange themselves at 1150°C, and form low energy dislocation structures (KUHLMANN-WILSDORF, 1999a), as shown in Figure 44a. Recovery precedes recrystallization by creating crystallites with low internal dislocation density bounded by a mobile high angle boundary (YU; HANSEN; HUANG, 2013). Following nucleation, the near defect-free grains sweep the deformed matrix.

Considering the pole figures in Figure 41 and the high KAM regions along $\langle 100 \rangle \parallel$ BD tracks in Figures 20b and 21b, recrystallization is nucleated at $\langle 110 \rangle \parallel$ BD grains at the vicinity of $\langle 100 \rangle \parallel$ BD. The high dislocation density along the latter grains provides the driving pressure for grain boundary bulging into the centerlines and the formation of low dislocation density crystallites in the $\langle 110 \rangle \parallel$ BD grains, i.e., strain-induced boundary migration (SIBM).

Obstacles for recrystallization evolution arise from two kinetic reasons: orientation and particle pinning. Twinning provides new grains with high angle relationships to the deformed matrix due to the formation of stacking faults at pinned low-mobility boundaries, as already reported by Field *et al* (2007). Twinning is facilitated when stacking faults are thoroughly present in the deformed matrix (FIELD *et al.*, 2007), which is commonly observed in cell walls from LPBF AISI 316L stainless steel (VOISIN *et al.*, 2021). When the recrystallized grains becomes stagnant due to orientation pinning, low angle boundaries may nucleate twins (BEYERLEIN; MCCABE; TOME, 2011) due to the decomposition of boundary dislocation into stacking faults (PENG *et al.*, 2019). The new twin boundary reacts and creates mobile boundaries (RANDLE, 1999). When particle pinning stops grain boundary migration, twins may be formed by dissociation reactions from grain boundaries (KUMAR; SCHWARTZ; KING, 2002; MEYERS; MURR, 1978).

In both cases, the coherent twin boundary is stagnant due to its low mobility, which is the reason why it is left behind, as seen in Figure 41a. Therefore, the other mobile grain boundary formed during the decomposition or grain boundary reaction sweeps the deformed matrix due to their high mobility. The mechanism for nucleation and evolution of recrystallization based on twinning is illustrated in Figure 44c. This mechanism is supported by the initial high twin boundary fraction between recrystallized grains in the unidirectional scan (0.52) during the initial 15 min of annealing at 1150°C, as seen in Figure 42b1. For this scanning strategy, orientation pinning is stronger and the need for twinning events to create grains with more mobile orientations is more intensive in the early stages of annealing to overcome the low net driving pressure for recrystallization, as suggested by Field *et al.* (2007).

Figure 43 - (a) Image quality map interposed with boundaries. Red circles indicate regions where twinning occurred to create grains with new mobile boundaries. (b) ECCI from a twinning event from the orange circle in (a) highlighted by an orange circle. (c) Suggested mechanism for recrystallization starting at recovery to SIBM and twinning to create more boundaries with high mobility. In (c), bold blue lines represent less recovered cell walls compared to the thin lines.



Source: Author

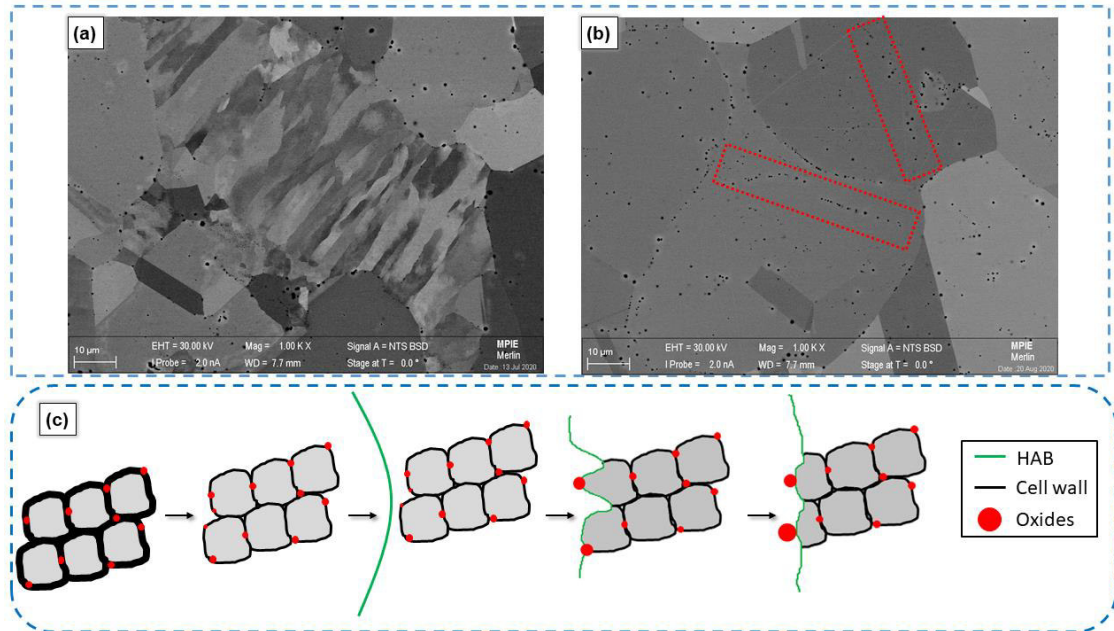
For all investigated samples, recrystallization is incomplete even after annealing at 1150°C for 8 h, as depicted in Figure 32. First, quick recovery takes place at such high annealing temperature, which allows for a high mobility for dislocations to rearrange and annihilate themselves, thereby reducing the driving pressure for recrystallization (SALLEZ *et al.*, 2015). The as-built dislocation density is reduced to $3 \times 10^{12} \text{ m}^{-2}$ in recovered areas for both scanning strategies after 1 h of annealing and remains almost constant for longer annealing times. Second, a high volume fraction of oxide particles is observed following annealing, as seen in Figure 40b. Such oxide particles coarsen during annealing (Ostwald ripening) mechanism (PHILIPPE; VOORHEES, 2013). Figure 44a shows a non-uniform spatial and size distribution of particles dispersed in the microstructure. Coarser oxide particles are found within recrystallized grains and decorating their grain boundaries, while finer particles are observed dispersed on the recovered matrix. For example, the average particle size for the coarser group is 850 nm while the fine particles within recovered grains is only 50 nm for both scanning strategies.

We suggest that oxide particles coarsen because of the enhanced diffusion along grain boundaries compared to the bulk diffusion (DAS *et al.*, 2014), since at the beginning the largest particles are around 250 nm. Within recovered grains, where particles are coarsened by bulk or pipe diffusion, such particles coarsen slowly, reaching a maximum average value of around 300 nm for both cases, whereas they reach up to 1.8 μm when localized within recrystallized grains due to the importance of grain boundary diffusion for particle coarsening.

Oxide particles accumulate along the moving grain boundary and a higher volume fraction is found along these boundaries compared to the bulk. When a critical fraction of particles pins a certain boundary, the movement ceases. Then, particles are rapidly coarsened by grain boundary diffusion via Ostwald ripening. After sufficient coarsening, which diminishes the Zener-Smith pinning force (NES; RYUM; HUNDERI, 1985) by reducing the number density of particles pinning the boundary, the grain boundary is unpinned and moves again, leaving the coarse particles within the recrystallized grains in a well-patterned distribution regarding the previous boundary position, as shown in Figure 44b. Therefore, a stop-and-go boundary migration occurs, as shown in Figure 44c, delaying recrystallization.

Therefore, orientation pinning is the main factor responsible for the noticed difference in recrystallization kinetics between the employed scanning strategies, while in both cases the stop-and-go migration of grain boundaries caused by particle pinning contributes to the sluggish kinetics. Particle pinning and the related stop-and-go mechanism is expected to delay the recrystallization kinetics in all additively manufactured materials due to the inherent in-situ formation of oxides in alloys processed by this technique (DE LUCA *et al.*, 2021; LIN *et al.*, 2020b; TANG; PISTORIUS, 2017; YAN *et al.*, 2018). Our study shows the possibility of creating engineered microstructures by LPBF and upon further post-processing annealing, where non uniform microstructures are created due to the linear impingement of recrystallized grains. The recrystallization kinetics is deeply affected by the employed scanning strategy, where the orientation pinning is the main factor for such difference. Particle pinning and the related stop-and-go mechanism are expected to delay the recrystallization kinetics in all additively-manufactured materials due to the inherent in-situ formation of oxides in LPBF-processed alloys (DE LUCA *et al.*, 2021; LIN *et al.*, 2020b; TANG; PISTORIUS, 2017; YAN *et al.*, 2018).

Figure 44 - (a) ECCI image showing heterogeneous particle size and spatial distribution; (b) ECCI image showing the alignment of particles (within the red rectangle) due to a boundary decoration. When Zener pinning decreases by particle coarsening, the boundary continues to move and leaves behind a well-patterned distribution of previously boundary-pinned particles; (c) Stop-and-go mechanism caused by the pinning and subsequent coarsening of particles (red) until the moving boundary (green) is released. In (c), bold black lines represent thicker cell walls, while thinner black lines represent recovered cell walls. Note the disappearance of finer oxides due to the Ostwald ripening mechanism.

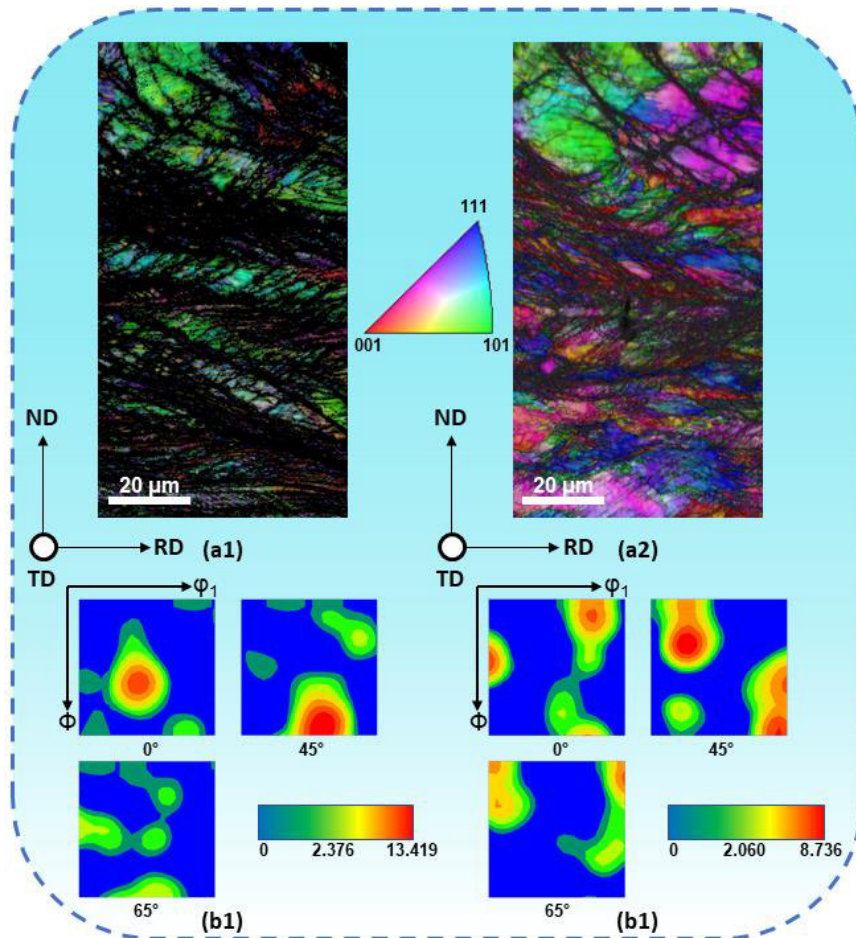


Source: Author

5.3 Cold rolling after LPBF processing

Cold-rolled specimens were obtained by rolling (63% reduction) along the scanning direction (RD || SD) and ND || BD, as indicated in Figure 1b. The resulting microstructure consisted of a heavily twinned and fragmented microstructure, as indicated by Figures 4471 and 47a2 for specimens 0R and 90R, respectively. For both conditions, many bands are observed coinciding with low-indexed regions. The resulting textures are shown in Figures 47b1 and 47b2 for the 0R and 90R specimens, respectively. For the 0R specimen, a characteristic and strong Brass texture $\{110\}\langle 112 \rangle$ is found due to the intense twinning during deformation (RAVI KUMAR *et al.*, 2005). For the 90R specimen, the most intense Brass texture $\{110\}\langle 112 \rangle$ is accompanied by a Goss $\{110\}\langle 100 \rangle$ and twin-Cu $\{552\}\langle 115 \rangle$ textures. Goss and twin-Cu textures are intensified during cold rolling as more twinning events occur (CHOWDHURY; DAS; DE, 2005).

Figure 45 – Inverse pole figure (IPF) from the longitudinal cross section (RD x ND) for the (a1) 0R and (a2) 90R samples. The orientations shown by the IPF are related to the rolling direction (\parallel RD). ODF figures for the (b1) 0R and (b2) 90R samples.



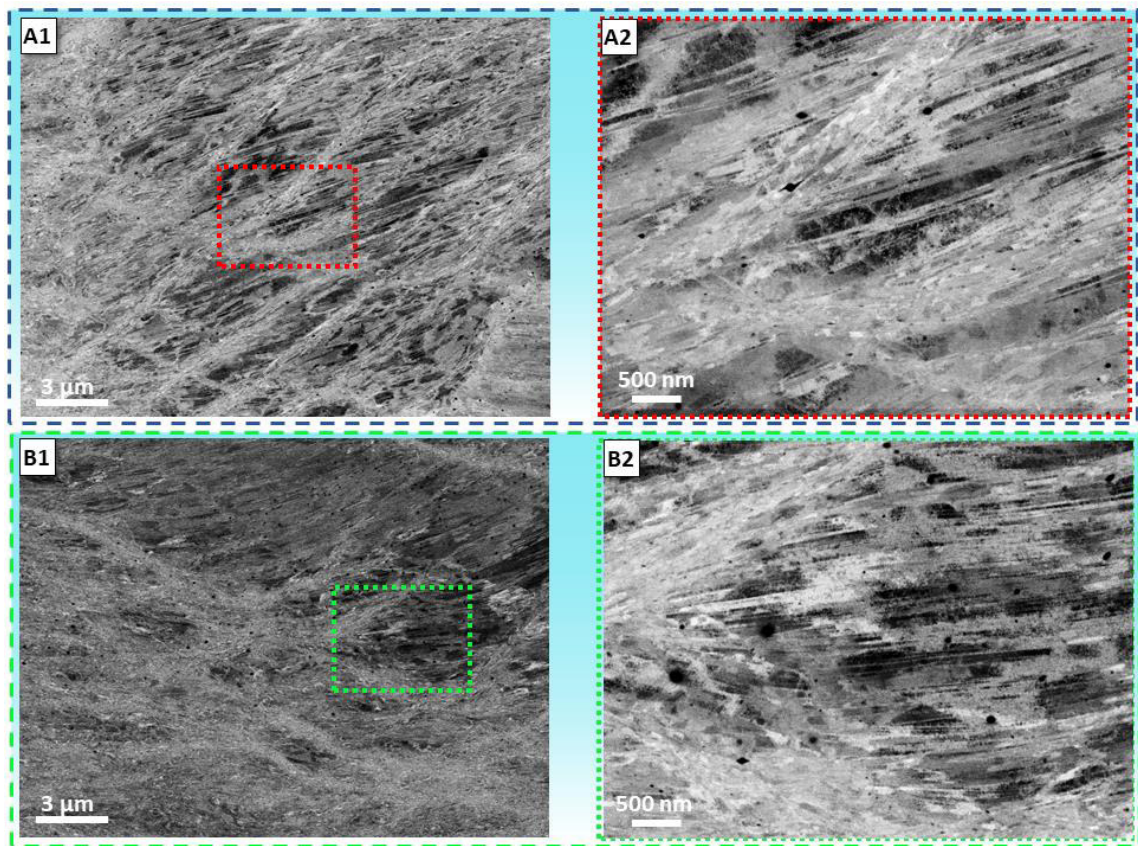
Source: Author

The fine substructure formed during cold rolling is visualized in more details in Figure 46 by ECCI. Comparing Figures 48a and 48b, the presence of shear bands is frequently observed for both specimens. In both cases, several fine twins are observed, as well as a high dislocation density. However, the high population of defects hinders the quantification of such lattice defects by ECCI. For this end, we used XRD to quantify the dislocation density as well as the stacking fault probability based on the Warren and Popa + Williamson-Smallman method, respectively, given in Table 4. For both conditions, a similar behavior regarding the defect population is found. The dislocation density increases by around 1 order of magnitude after cold-rolling, mainly due to dislocation slip along shear bands. The stacking fault and twinning probabilities are also similar for both conditions despite the difference in the initial microstructure, indicating intense twinning and slip of partial dislocations during cold rolling.

Table 4 - Dislocation density for 0R and 90R samples as measured by ECCI and XRD (Williamson-Smallman method). Stacking faults (intrinsic and extrinsic) and twinning probabilities are obtained from XRD data based on the Warren method.

	LPBF		LPBF + CR (63CR)	
	0R	90R	63CR-0R	63CR-90R
Dislocation density (m^{-2})	1.6×10^{15}	8.8×10^{14}	1×10^{16}	2.5×10^{16}
Intrinsic SF probability	2.3×10^{-6}	1.4×10^{-9}	4.2×10^{-3}	6.0×10^{-3}
Extrinsic SF probability	1.7×10^{-6}	1.1×10^{-9}	4.6×10^{-4}	2.4×10^{-4}
Twinning probability	2.8×10^{-6}	3.5×10^{-6}	2.3×10^{-3}	2.0×10^{-3}

Figure 46 - Defect population and substructure created by cold-rolling in LPBF AISI 316L specimens employing the (a) 0R and (b) 90R scanning strategies. Figures A2 and B2 are magnifications from the marked area by red and green in Figure A1 and Figure B1, respectively. Note the intense shearing and twinning.



Source: Author

5.3.1 The influence of two different starting microstructures obtained by LPBF in cold rolling

The unique microstructures obtained from the LPBF process was little explored in terms of post processing via further cold rolling. Only exploratory studies on the possibility of mechanical properties optimization (LIN *et al.*, 2020a) and grain boundary engineering (GAO *et al.*, 2020) were reported. In this case, cold rolling was used only as intermediate processing step and no microstructural characterization was carried in the deformed state. Although the microstructural evolution was not followed during cold rolling and only one true strain ($\epsilon = 1$) was studied, the active deformation mechanisms up to this stage are identified. In Figure 46, twins and shear bands are observed for both cases. The morphological features in Figure 46 indicate that sample deformed initially by slip. The slip of partial dislocations gives rise to intense twinning (STEINMETZ *et al.*, 2013).

When a critical point is reached, plastic instabilities arise and concentrated slip along shear bands are developed as alternative deformation mechanism due to the high interface and defect density in the matrix. Shear bands are not crystallographic and grow across several grains, as seen in Figure 44a. Two main sets of shear bands are formed during deformation. Due to the disturbance created by the second set of shear bands on the first set, it is possible to identify which set appeared before, as shown in Figure 47a. This deformation sequence is schematically shown in Figure 47b.

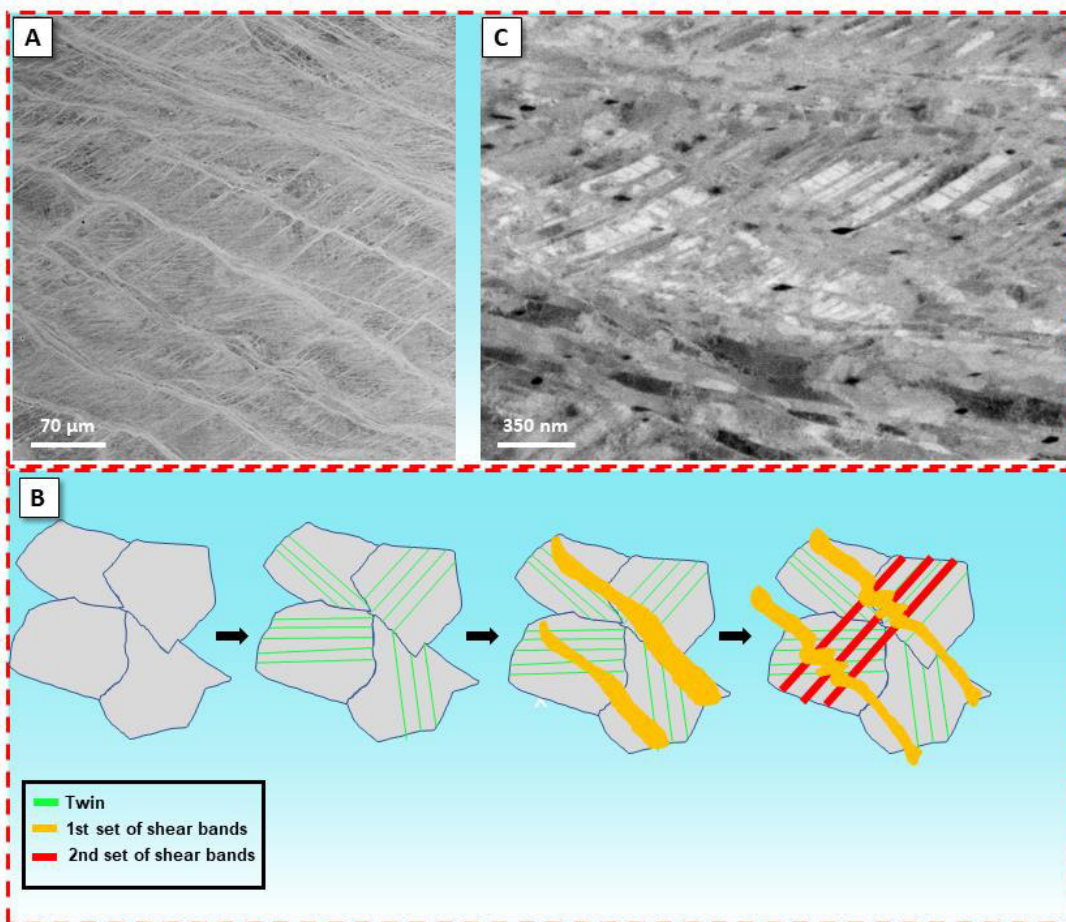
The substructure of these shear bands is composed of fine lath subgrains, as shown in Figure 47c, similar to the shear bands observed in conventionally-processed or LPBF-processed AISI 316L under shear tests (WEAVER; LIVESCU; MARA, 2020). The fine subgrain structure is formed due to localized slip along these plastic instabilities regions and concurrent dynamic recovery (XUE; CERRETA; GRAY, 2007; XUE; GRAY, 2006b). The shear regions are not well indexed in EBSD due to the highly fragmented substructure, but they are expected to create a $\langle 110 \rangle$ fiber texture (MEYERS *et al.*, 2003). Goss $\{110\}\langle 100 \rangle$, twin-Cu $\{552\}\langle 115 \rangle$, and Brass $\{110\}\langle 112 \rangle$ texture components are promoted by twinning and found in both studied samples (CHOWDHURY; DAS; DE, 2005).

The appearance of profuse shear bands is not observed in cold-rolled AISI 316L up to 63% of reduction (CHOWDHURY; DAS; DE, 2005; ODNOBOKOVA; BELYAKOV; KAIBYSHEV, 2015). Also, no presence of strain-induced martensite was observed in our case, differently from conventional AISI 316L following cold-rolling (NEZAKAT *et al.*, 2014; ODNOBOKOVA; BELYAKOV; KAIBYSHEV, 2015).

The initial high dislocation density inherited from LPBF combined to twinning during deformation increases the defect population in LPBF AISI 316L, as seen in Table 4. As a result, deformation becomes increasingly difficult to take place due to the work hardening created by such deformation mechanisms (HAASE *et al.*, 2014). At a critical point, deformation through further twinning and slip will be difficulted due to the fine defect substructure and the saturation of local dislocation density. Shear bands appear as an alternative deformation mechanism when a high stress concentration appears (MOHAMMED; EL-DANAF; RADWAN, 2007), shearing the twinned matrix and creating a heterogeneous and localized deformation, further reducing the work hardening rate (HAASE; BARRALES-MORA, 2018).

Besides the microstructural changes in the matrix, cold rolling induces changes in the shape of the oxide particles, as seen in Figure 47c. The plastic activity, mainly along shear bands, shears such particles resulting in their shape alteration compared to the spherical particles observed in the as-built condition, as shown in Figure 25. This induces differences in the particle size and spatial distribution after further annealing.

Figure 47 - (a) Disturbances in the first set of shear bands due to the growth of the second set of shear bands in cold-rolled LPBF AISI 316L stainless steel. (b) Deformation sequence schematics based on the experimental results. (c) Substructure details from the shear bands showing fine lath subgrains and a twinned matrix in between shear bands. Note the change in the oxide shape resulting from shear.



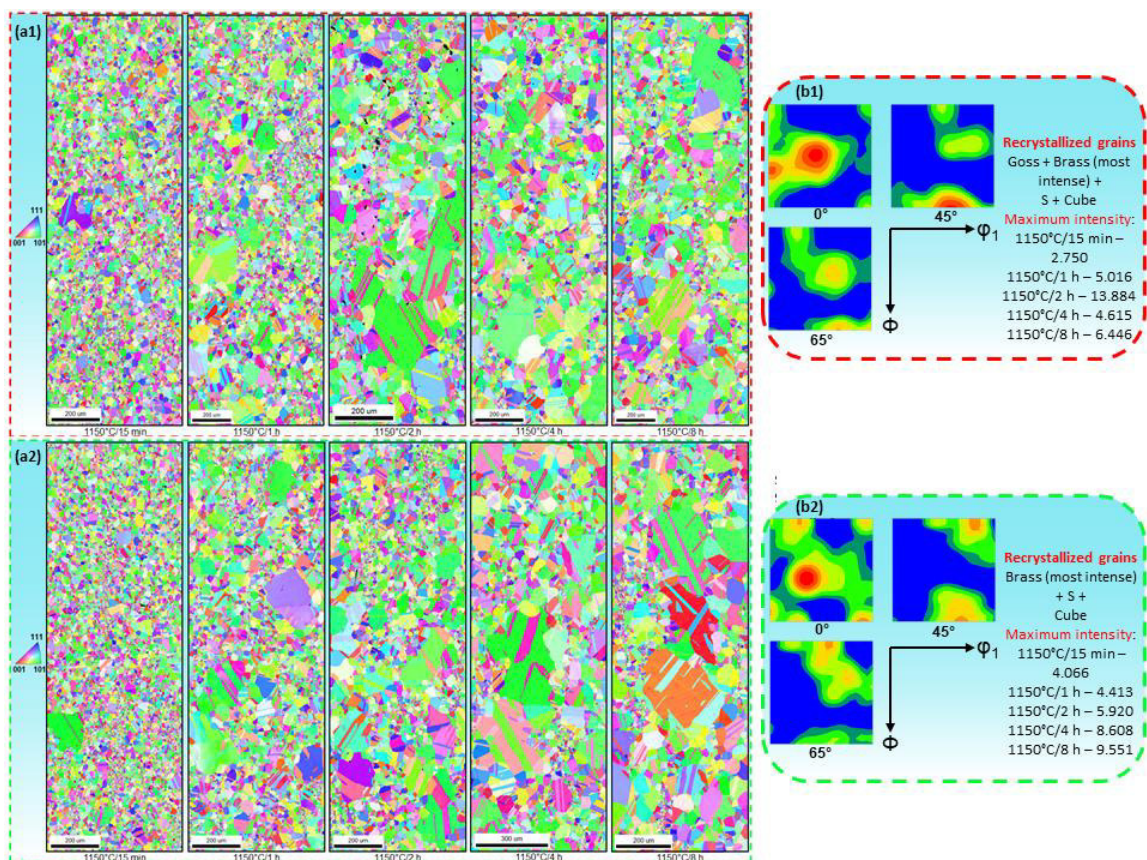
Source: Author

5.4 Annealing of cold-rolled AISI 316L

The microstructure evolution upon annealing for samples processed by LPBF followed by cold rolling is shown in Figure 48a1 for 0R specimens and Figure 48a2 for 90R specimens. Differently from samples annealed directly after LPBF, recrystallization is completed after 15 min at 1150°C because of the higher dislocation density. Observing Table 4 and Figure 46, the dislocation density increases up to 1 order of magnitude during cold rolling, besides the creation of a high number of twins and stacking faults. This increased defect density provides the driving force for recrystallization and many nucleation sites due to the formation of deformation-induced high angle boundaries (HUGHES; HANSEN, 1997), as seen in Figure 46.

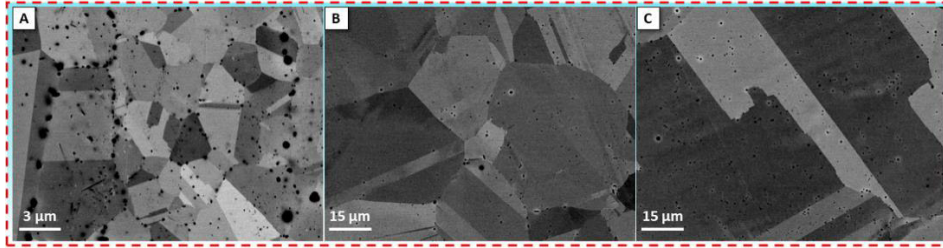
Figures 50a1 and 50a2 reveal the formation of three groups of grains regarding their size: a region of ultrafine grains (hereafter named “fine”), another for recrystallized grains (hereafter named “RX”) along with abnormally large grains (hereafter named “AGG”). Figures 50b1 and 50b2 show the ODFs for 0R and 90R samples, respectively. For both cases, the textures components behave similarly. From 15 min to 8 h at 1150°C, texture components do not change, although their intensity is strengthened. The main texture component is Brass $\{110\}\langle 112\rangle$ with a strong presence of $\langle 110\rangle \parallel \text{ND}$ in all conditions. Figure 49 shows ECCI images from all three different regions seen in Figure 8a, i.e., fine, RX and AGG grains. Comparing Figure 49a, for fine recrystallized grains, Figure 49b, for coarser RX grains and Figure 49c, for AGG grains, a remarkable trend is noticed. While AGG and RX grains present qualitatively similar particle spatial and size distribution, the fine fraction is characterized by a higher number of finer oxide particles mainly located along grain boundaries.

Figure 48 - IPF for the (a1) 63CR-0R and (a2) 63CR-90R specimens. Note the presence of abnormal grains, as well as recrystallized and fine grains. ODF for the (b1) 63CR-0R and (b2) 63CR-90R specimens.



Source: Author

Figure 49 – Micrographs showing the spatial distribution of particles and their size difference depending on the microstructural site for the (a) fine grains, (b) recrystallized grains and (c) abnormal grains.



Source: Author

5.4.1 Abnormal grain growth (AGG)

Abnormally-large grains are found for all cold-rolled and annealed LPBF AISI 316L specimens, while it is absent when cold rolling is not applied as an intermediate processing step. AGG is known to be caused by a growth advantage of a few grains (LIU; MILITZER; PEREZ, 2019b). In the following, we will discuss possibilities on the origin of abnormal grain growth in these specimens.

5.4.1.1 Roughening transition

Roughening transition consists in a change from faceted to rough boundaries as temperature increases (STRAUMAL *et al.*, 2015). While atomically faceted grain boundaries present low mobility due to the nucleation and growth of atomic steps, creating a stepwise movement, rough boundaries show higher mobility (HOLM; FOILES, 2010). At a given temperature, a certain fraction of boundaries are rough and this value increases for higher temperatures (JUNG; KANG, 2014). The roughening temperature is similar for crystallographically-close boundaries, although no relationship between misorientation and boundary energy was found (OLMSTED; HOLM; FOILES, 2009). AGG was reported in the literature for AISI 316L at 1100°C and accounted for the roughening transition (CHOI; YOON, 2001). However, other studies report the partial dissolution of precipitates as the main cause of AGG in austenitic stainless steels (PADILHA; PLAUT; RIOS, 2003).

To check the hypothesis of roughening transition, high-resolution transmission electron microscopy (HR-TEM) is necessary to image the interface in a near-atomic scale, which was not carried in our study.

However, the roughening transition is related to deeply influence grain growth behavior of high-purity metals (HOLM; FOILES, 2010), but its effect is surpassed by solute (KIM; PARK, 2008), precipitates (LU *et al.*, 2020), and orientation-dependent grain boundary mobility effects (SAITO *et al.*, 2021).

The studied alloys have all cited factors. While annealing of cold-rolled LPBF AISI 316L leads to AGG, when cold rolling is not applied, a sluggish recrystallization behavior is observed. If roughening transition is the main factor dictating mobility, then some boundaries of a given crystallography would grow faster and consume other recrystallized grains. It is unlikely that no boundary above the roughening transition temperature is present in all annealed (directly after LPBF) samples investigated. Thus, we discard the possibility of roughening transition as the main cause of AGG in this steel.

5.4.1.2 Second-phase particles

A heterogeneous distribution of particles could selectively pin certain boundaries, while allowing unpinned boundaries to grow freely (LU *et al.*, 2020). Therefore, we compare the particle size, volume fraction and nearest neighbor distance between the annealed LPBF material and the cold-rolled and annealed LPBF specimen, which is shown in Figure 50. The fine, recrystallized (RX), and abnormally large grains (AGG) fractions are sorted out. Data referring the annealed LPBF AISI 316L is considered in the RX fraction. First, the fine grains fraction shows a combination of higher volume percentage of particles, finer particle size and smaller nearest neighbor distance, as seen in Figures 52a, 52b and 52c, respectively. The heterogeneous spatial and size distribution of particles is created by the shear of such particles, as shown in Figure 47c.

Regions where particles undergo massive shearing, such as those at the intersection of two shear bands, are the most likely sites for this phenomenon. After shearing, such particles reorganize and grow during annealing, resulting in a fine dispersion. Recrystallized grains nucleating at these sites do not grow further due to the intense Zener-Smith pinning (HUMPHREYS; ARDAKANI, 1996).

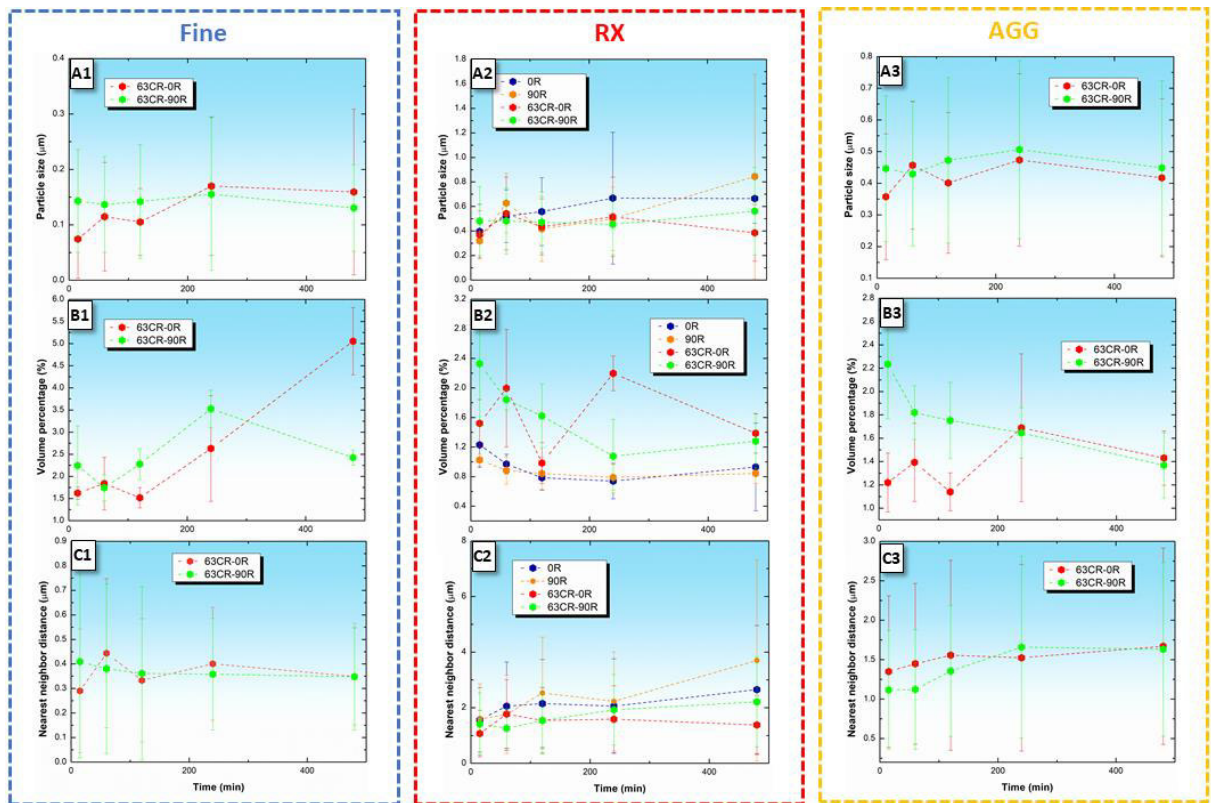
For the annealed LPBF specimen, a lower volume percentage of particles is found with coarser particles and higher nearest neighbor distances among all partitions, as seen in Figures 52a2, 52b2 and 52c2, respectively.

Cold-rolling probably favors the particle formation kinetics. For the cold-rolled and annealed specimens, the volume percentage tends to reach a similar value of around 1.4%, while particle size remains nearly constant and the distance between particles keeps constant for the recrystallized and the abnormal fraction. The similar behavior among these partitions occurs due to the consumption of recrystallized grains by abnormal grains. In this case, no indication of abnormal grains nucleating at a particle-poor regions and acquiring a size advantage was observed as reported in the literature (LU *et al.*, 2020).

Another issue is the shearing of particles during deformation. These particles are expected to be amorphous due to the high cooling rates (SAEIDI *et al.*, 2015a), so their change in morphology occurs due to the atomic mixing under high shear deformation (VO *et al.*, 2013), as indicated by the rough interfaces (not following a specific crystallographic relationship) in Figures 48a2 and 49c. The cutting of particles increases the Gibbs free energy due to the increase in interfacial energy.

As a result, these precipitates become thermodynamically unstable and dissolve (BEDNARCZYK *et al.*, 2021), while other grow due to the Ostwald ripening mechanism. The values of the RX fraction for the cold-rolled and annealed specimens were obtained from recrystallized grains in the vicinity of abnormal grains. If the heterogeneous distribution of particles was the main factor, abnormal grains would continue to consume the recrystallized grains in the surrounding. Therefore, from the exposed results, it is unlikely that the heterogeneous distribution of particles is the single main cause of AGG. Second-phase particles may be a prerequisite for abnormal grain growth and not the main factor (YANG; BAKER, 2020).

Figure 50 - (a) Average particle size, (b) volume percentage and (c) nearest neighbor distance for the second-phase particles found in (1) fine, (2) recrystallized and (3) abnormal grains. Values from the recrystallized grains were obtained in the vicinity of abnormal grains.



Source: Author

5.4.1.3 Texture

Texture is tightly related to grain boundaries. High-mobility grain boundaries are usually related to high misorientations ($\theta > 15^\circ$) (OLMSTED; HOLM; FOILES, 2009). A grain boundary is characterized by 5 parameters, where 3 of them are summarized in the misorientation angle and 2 of them define the grain boundary plane (RANDLE, 2001, 2006a, 2006b). Therefore, the same misorientation can show several energies and mobilities (OLMSTED; FOILES; HOLM, 2009; OLMSTED; HOLM; FOILES, 2009; SALAMA *et al.*, 2020). Besides the inherent variation in energy and mobility in grain boundaries depending on their misorientation and boundary plane, such interfaces may be also metastable, giving rise to more possibilities regarding such boundary properties (HAN; VITEK; SROLOVITZ, 2016).

Only three types of boundaries can be classified in terms of properties: LAB – low angle boundaries ($\theta \leq 15^\circ$), HAB – high angle boundaries ($\theta > 15^\circ$) and CT – coherent twins ($\Sigma 3$ $60^\circ \langle 111 \rangle$) (ZHANG *et al.*, 2020). Therefore, we consider LABs and CTs as low-energy and low-mobility boundaries, while HABs are considered as having high energy and mobilities. Considering the most usual texture components, and considering an angular deviation smaller than 10° , no preferential orientations were found. For example, about 25% of abnormal grains are from the Brass $\{110\} \langle 112 \rangle$ texture. However, many other orientations are found, mainly along the $\langle 110 \rangle \parallel$ ND fiber texture. This is clearly seen in Table 5, where the relative frequency of abnormal grains is shown for each fiber texture. The $\langle 11 \ 4 \ 11 \rangle \parallel$ ND and $\langle 407 \rangle \parallel$ ND fiber textures are located near the $\langle 110 \rangle \parallel$ ND fiber, where some overlap already occurs when the angular deviation is defined as smaller than 10° . If we consider all these fibers as $\langle 110 \rangle \parallel$ ND, where $\langle 11 \ 4 \ 11 \rangle \parallel$ ND and $\langle 407 \rangle \parallel$ ND are farther from the ideal $\langle 110 \rangle \parallel$ ND fiber, a total of 83.87% of abnormal grains for this fiber.

Table 5 – Relative frequency of abnormal grains from a determined fiber texture. The angular deviation from the ideal fiber is smaller than 10° .

	Fiber \parallel ND							
	$\langle 100 \rangle$	$\langle 110 \rangle$	$\langle 111 \rangle$	$\langle 112 \rangle$	$\langle 11 \ 4 \ 11 \rangle$	$\langle 4 \ 0 \ 7 \rangle$	$\langle 113 \rangle$	$\langle 5 \ 2 \ 21 \rangle$
Relative frequency (%)	1,61	54,84	1,61	6,45	17,74	11,29	4,84	1,61

Source: Author

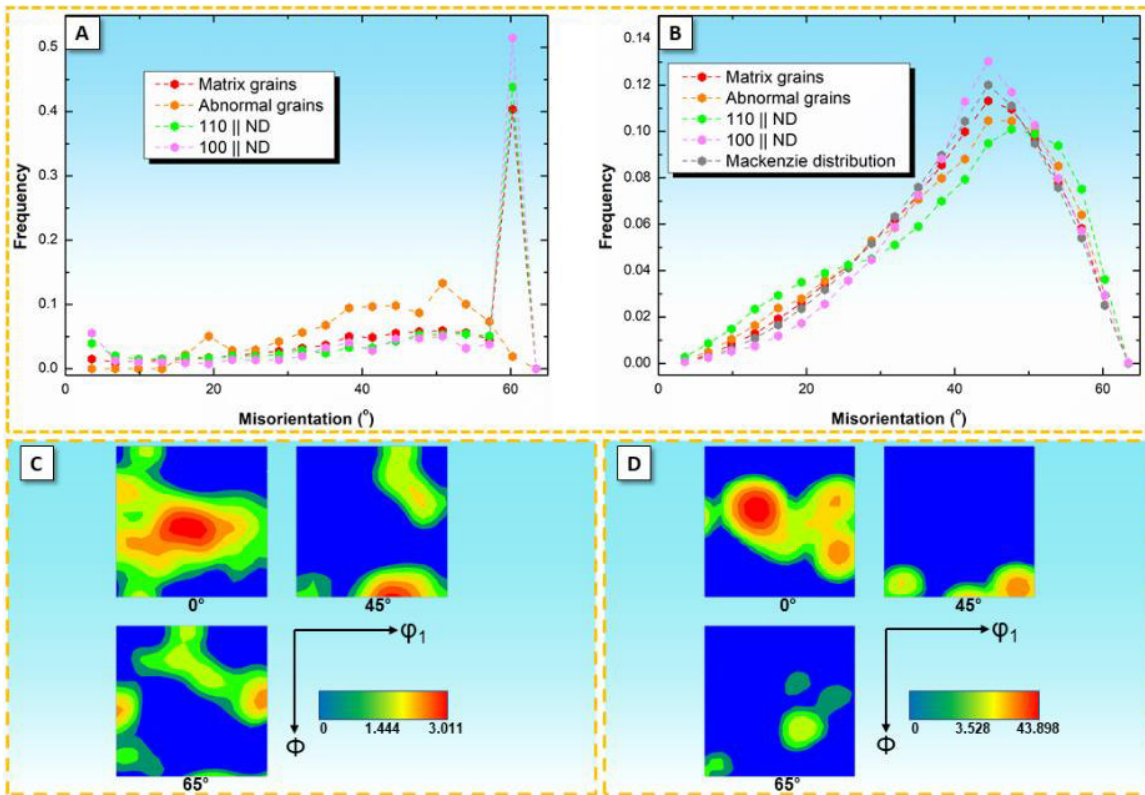
The preferential formation of abnormal grains from the $\langle 110 \rangle \parallel$ ND fiber texture was investigated in more detail. The growth advantage from certain orientations is related to the higher probability of finding high mobility grain boundaries with the recrystallized grains from the matrix (RIOS; GOTTSTEIN, 2001). Figure 51a shows the correlated misorientation angle distribution for grain boundaries between abnormal grains and the matrix, whereas Figure 51b shows the uncorrelated plots. The uncorrelated misorientation distribution is calculated based on the misorientation obtained from the orientation difference between a grain from the defined partition (abnormal grains or from a certain fiber texture) and all other grains from the other partition (recrystallized grains).

From Figure 51a, a similar correlated misorientation angle distribution is found for the matrix grains and both fiber textures, i.e., $100 \parallel \text{ND}$ and $110 \parallel \text{ND}$, with an intense peak at 60° due to twinning. Contrastingly, abnormal grains show a higher frequency of mobile high angle boundaries, while low angle boundaries are nearly absent, as well as twin boundaries. Figure 51b shows a similar uncorrelated misorientation angle distribution for all grains, independent on their size or orientation, following the classical Mackenzie distribution (MACKENZIE, 1957) for materials with cubic crystal symmetry and randomly-oriented grains. The nucleation of several grains and intense twinning (CHOWDHURY *et al.*, 2006) are responsible for a near-random texture, as shown by the matrix grains in Figure 51c. In Figure 51d, the orientation of abnormal grains is shown to occur mainly along the $\langle 110 \rangle \parallel \text{ND}$, which is the most common, although weak, texture for the matrix grains. As shown in Figure 51b, no growth advantage must arise for the $\langle 110 \rangle \parallel \text{ND}$ fiber or the abnormal grains due to their orientation, as all grains show near Mackenzie distribution due to the weak matrix texture. In other words, regarding the misorientation from grain boundaries, any grain from the matrix has a similar condition to grow, as indicated by Figure 51b. However, only grains near the $\langle 110 \rangle \parallel \text{ND}$ fiber are frequently found to have such growth advantage.

Rather than a growth advantage due to high mobility grain boundaries, abnormal grains result from an initial grain size advantage. Figure 52a reveals that $\langle 110 \rangle \parallel \text{ND}$ and fiber textures near the $\langle 110 \rangle \parallel \text{ND}$, such as $\langle 11\ 4\ 11 \rangle \parallel \text{ND}$ and $\langle 407 \rangle \parallel \text{ND}$ have a coarser grain size and are present in a higher volume fraction among the recrystallized grains from the matrix.

Grains near the $\langle 110 \rangle \parallel \text{ND}$ fiber may be favorably formed during recrystallization, as indicated by their larger grains and higher volume fraction. The $\langle 110 \rangle \parallel$ fiber texture expected along shear bands (MEYERS *et al.*, 2003) matches the same texture formed by the majority of abnormal grains upon annealing. As the shear bands are the regions with higher defect density, they are expected to recrystallize first. Recrystallized grains inherits the orientation from the shear bands (HUMPHREYS; HATHERLY, 2004b), the $\langle 110 \rangle \parallel \text{ND}$ fiber texture and evolve faster than other texture components. Oxides are sheared along shear bands, destabilizing them and promoting their dissolution (BEDNARCZYK *et al.*, 2021).

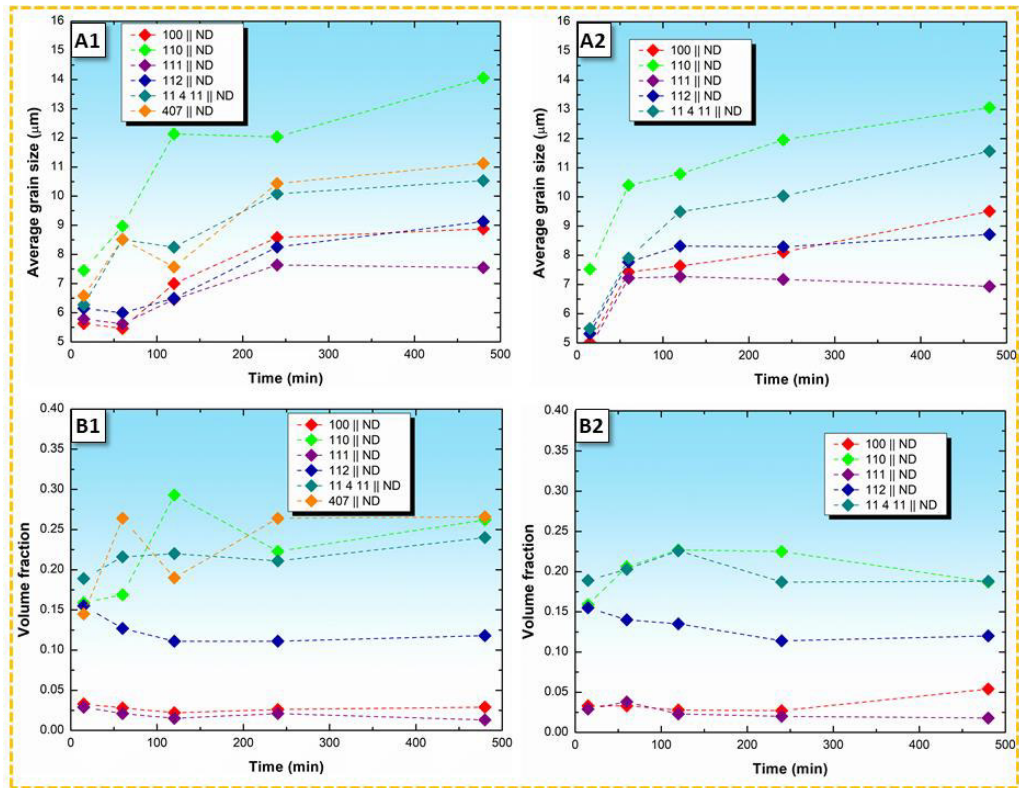
Figure 51 - (a) Correlated misorientation angle distribution and (b) uncorrelated misorientation angle distribution for abnormal and matrix grains, as well as for two fiber textures. ODF for the (c) matrix grains and (d) abnormal grains.



Source: Author

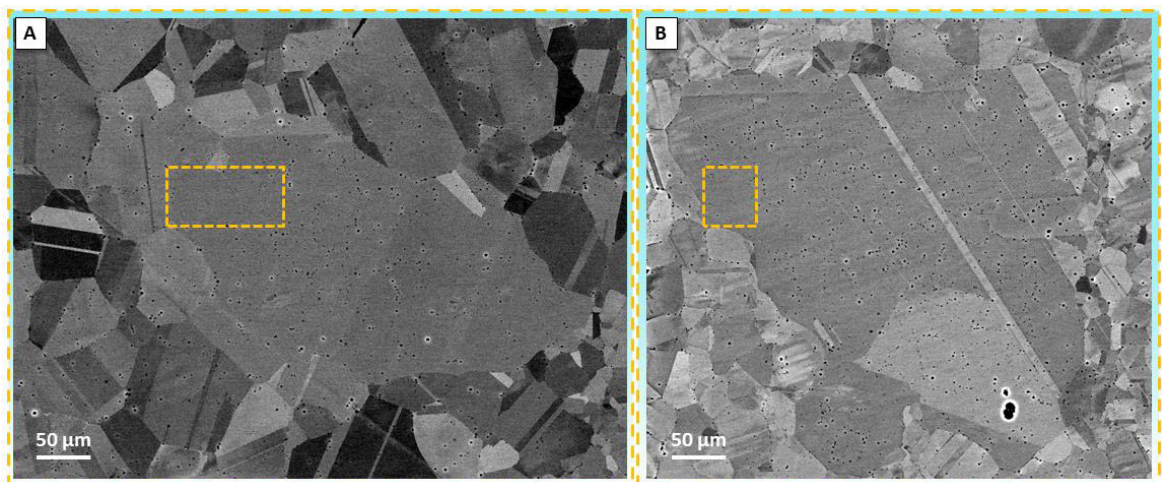
Therefore, $\langle 110 \rangle$ || ND grains acquire a size advantage due to earlier recrystallization in particle-depleted regions, as seen in Figure 53. It must be noted that a simple size advantage is not enough to allow for AGG (DECOST; HOLM, 2017; ZÖLLNER; RIOS, 2018). However, an initial grain size advantage may sustain abnormal grain growth when microstructural features cause boundary pinning (LIU; MILITZER; PEREZ, 2019b), such as particles and immobile boundaries. By combining the Smith-Zener pinning and the 3-D capillarity-driven grain growth, Lu *et al.* (2020) found a critical grain size for sustained abnormal growth when a selected grain has double the average grain size. This is applicable in systems with strongly-pinned grain boundaries, such as in the cold-rolled material. In Figure 51a, the grain size distribution is shown for different fiber textures, as well as the critical size for abnormal grain growth for the 63CR-90R sample annealed at 1150°C for 15 min. Fibers near $\langle 110 \rangle$ || ND (Figure 51a1) have a higher number fraction of grains above the critical value for AGG. In Figure 51a2, a few grains are above the critical grain size, but just a few of them grow abnormally, as seen in Table 5.

Figure 52 – Average grain size for different fiber textures in the (a1) 63CR-0R and (a2) 63CR-90R specimens. Volume fraction of fiber textures for the (b1) 63CR-0R and (b2) 63CR-90R specimens. Only recrystallized grains from the “matrix” were considered, i.e., abnormal and fine grains were not accounted in this quantification.



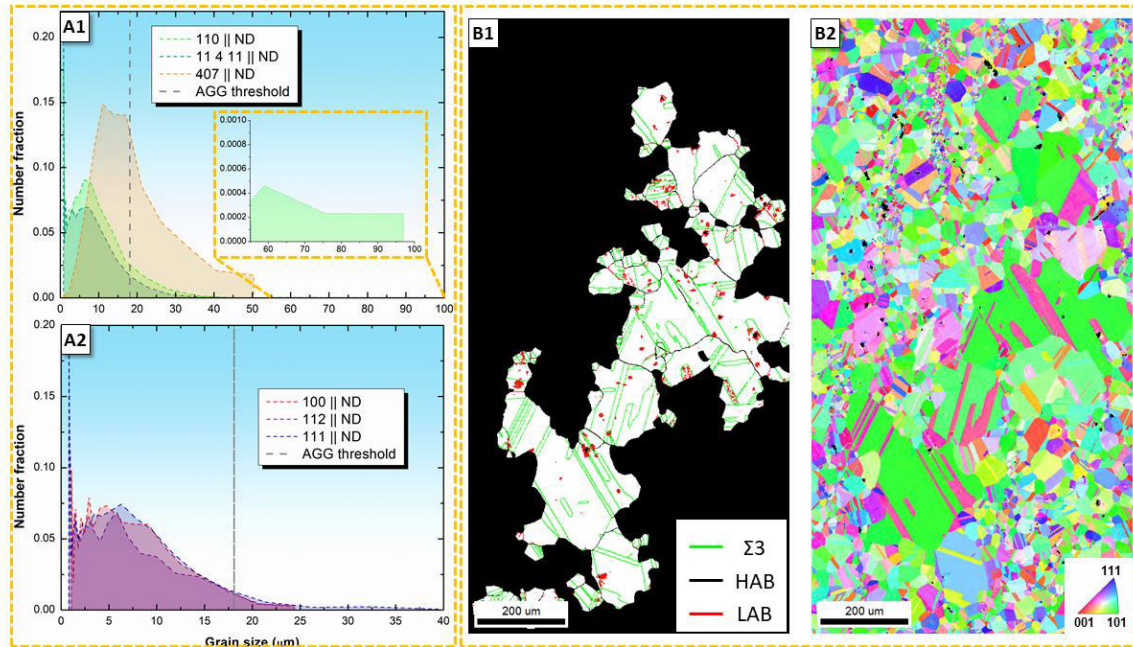
Source: Author

Figure 53 - Abnormal grains from sample (a) 63CR-0R annealed at 1150°C/1 h and (b) 63CR-90R annealed at 1150°C/15 min. The orange squares show regions with low particle density where AGG may have started.



Source: Author

Figure 54 - Grain size distribution for the (a1) for fiber textures usually forming abnormal grains. Note the inset showing the presence of a few extremely large $\langle 110 \rangle \parallel \text{ND}$ grains. (a2) fiber textures which rarely form abnormal grains. (b1) Boundaries and (b2) IPF map from the 63CR-0R sample annealed at $1150^\circ\text{C}/2 \text{ h}$ showing examples of abnormal grains, mainly from the $\langle 110 \rangle \parallel \text{ND}$ fiber.



Source: Author

Figure 54b shows examples of abnormal grains, highlighted in Figure 54b1, from the 63CR-0R sample annealed at 1150°C for 2 h. Note that most abnormal grains are oriented near $\langle 110 \rangle \parallel \text{ND}$.

Although a considerable number of grains is above the critical grain size, as shown in Figure 54, just a few of them outgrows the other grains. This is because the combined Zener-Smith pinning and 3-D curvature-driven grain growth model suggested by Lu *et al.* (2020) does not take into account the local microstructure environment for abnormal growth. In our case, there is a combination of a high volume fraction of precipitates pinning the boundaries and the presence of many immobile twin boundaries. Figure 55a shows the twin boundary fraction evolution for all samples, where a value higher than 0.49 is always found, while their spatial distribution is shown in Figure 55b1. Figure 55b2 shows the microstructure for the recrystallized grains.

Note many twin boundaries and some low angle boundaries connected in triple and quadruple points and separating recrystallized grains. Low mobility boundaries, such as LABs and twin boundaries, delay the growth of recrystallized grains.

When these boundaries are present along triple junctions, they reduce its energy and mobility (TANG; REED; KUMAR, 2012), stabilizing the grain boundary network and resulting in sluggish grain growth kinetics. In these cases, even with an initial size advantage, some grains do not grow due to kinetics reasons.

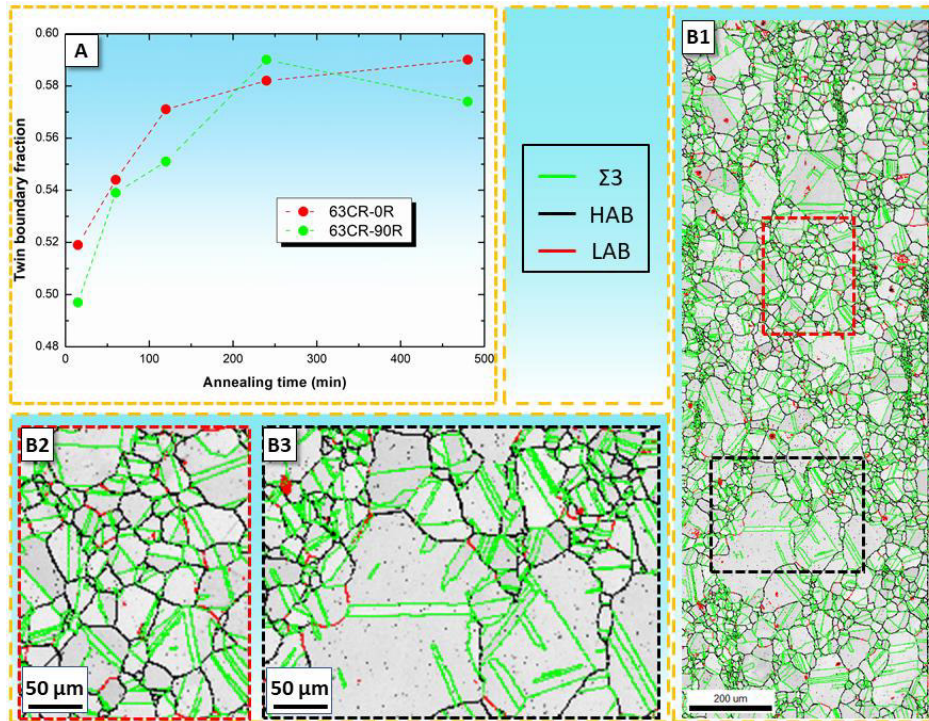
When grains above the critical size find a favorable microstructural environment, their abnormal growth is sustained, as shown in Figure 53b3. Due to the low mobility, twin boundaries are found as island grains in Figure 53b3. Most of the grain boundaries surrounding the abnormal grain has a high angle character due to its higher mobility. Low angle and twin boundaries are consumed or left behind during abnormal growth given their lower mobility. This results in the consumption of such boundaries and the consequent formation of island grains (BENNETT; KALU; ROLLETT, 2007).

In this Dissertation, the cold rolling behavior of AISI 316L stainless steel processed by LPBF and its subsequent annealing were conducted and compared to the as-built and directly annealed (following LPBF) counterparts. Cold rolling resulted in massive twinning after initial dislocation slip. The intense twinning and the related defect density facilitated the formation of early plastic instabilities, i.e., shear bands.

Upon annealing, the cold-rolled material underwent abnormal grain growth, while the directly annealed sample displayed recrystallization and limited normal grain growth. Although the directly annealed sample had a stronger texture, which would facilitate abnormal grain growth, this phenomenon did not take place due to incomplete recrystallization and low driving pressure for grain growth from recrystallized grains. In the cold-rolled material, the initial fine grain size allows for significant driving pressure for grain growth. An initial grain size advantage from $\langle 110 \rangle \parallel$ ND fiber grains due to their earlier recrystallization along particle-depleted regions in shear bands resulted in a majority of abnormal grains with this orientation.

A low critical grain size (about twice the average grain size) is required for the onset of abnormal grain growth (LU *et al.*, 2020). However, the surrounding microstructure avoids the development of abnormal grains due to the stability and low mobility of twin and low angle boundaries. To the best of our knowledge, this is the first investigation into the mechanisms of deformation of 3-D-printed parts during cold rolling followed by annealing, resulting in abnormal grain growth in LPBF-processed AISI 316L stainless steel.

Figure 55 - (a) Twin boundary fraction for cold-rolled and annealed AISI 316L processed by LPBF. (b1) Boundary maps for the 63CR-0R sample annealed at 1150°C for 4 h. Insets from figure (b1) are found as red square, showing (b2) recrystallized grains and black square showing (b3) abnormal grains. Note the formation of island grains in (b3).



Source: Author

6 Conclusions

The main conclusions from this Master's Dissertation are summarized as follows:

As-built condition

- A significant difference in dislocation density and residual stresses exist in different regions of the 3-D printed parts, indicating a direct dependence on the chosen scanning strategy.
- Dislocations nucleate to relieve residual stresses upon intrinsic heat treatment.
- Microstructure engineering is possible by selecting proper process parameters in LPBF, namely the scanning strategy, resulting in a chessboard-like pattern (90R) or in a lamellar microstructure (0R).
- Dislocation cells relieve residual stresses forming upon constrained thermal shrinkage and expansion. They also redistribute stresses and reduce the stored elastic energy, favoring further plastic deformation. This mechanism aids at maintaining the integrity of LPBF parts by avoiding high stress concentrations that could lead to cracking or delamination;
- Dislocation cells are formed by trapping of statistically stored dislocations at solidification cell walls characterized by oxide nanoparticles and segregated solute. Then, geometrically necessary dislocations redistribute stresses;
- Dislocation cells are incidental dislocation boundaries and show random fluctuation on the misorientation accumulation. Contrastingly, low angle boundaries are geometrically necessary boundaries and accumulate misorientation as the grain grows.

Annealed condition

- Recrystallization begins in clusters showing a linear impingement pattern along the scanning direction.
- Mechanisms of recrystallization are summarized as strain induced boundary migration (SIBM), twinning, and stop-and-go boundary migration.
- Recrystallization shows a sluggish kinetics due to strong particle pinning. The difference in kinetics between the 90R (faster) sample and 0R sample is explained based on orientation pinning.
- Partly-recrystallized engineered microstructures may be created, such as the lamellar microstructure from 0R specimen following annealing.

Cold-rolled and annealed conditions

- The deformation mechanisms in cold-rolled AISI 316L stainless steel are slip, twinning and shear banding, in this order, up to a true strain $\epsilon = 1$.
- During deformation, oxide particles are fragmented mostly by shear bands. Upon annealing, their distribution is non-uniform, resulting in regions interspersing fine-recrystallized and abnormal grains.
- Abnormal grains form mainly due to orientation advantage. Further investigation needs to be carried to clarify this mechanism, i.e., advantage due to earlier recrystallization or due to mobility advantage. The presence of twin boundaries and dispersed particles also play likely secondary roles.

References

AHMAD, B. et al. Residual stress evaluation in selective-laser-melting additively manufactured titanium (Ti-6Al-4V) and inconel 718 using the contour method and numerical simulation. **Additive Manufacturing**, v. 22, n. May, p. 571–582, 2018.

ALI, H.; GHADBEIGI, H.; MUMTAZ, K. Effect of scanning strategies on residual stress and mechanical properties of Selective Laser Melted Ti6Al4V. **Materials Science and Engineering A**, v. 712, n. November 2017, p. 175–187, 2018.

ANDREAU, O. et al. Texture control of 316L parts by modulation of the melt pool morphology in selective laser melting. **Journal of Materials Processing Technology**, v. 264, n. August 2018, p. 21–31, 2019.

ANTONY, K.; ARIVAZHAGAN, N.; SENTHILKUMARAN, K. Numerical and experimental investigations on laser melting of stainless steel 316L metal powders. **Journal of Manufacturing Processes**, v. 16, n. 3, p. 345–355, 2014.

AOTA, L. S. et al. Laser powder-bed fusion as an alloy development tool: Parameter selection for in-situ alloying using elemental powders. **Materials**, v. 13, n. 18, p. 1–17, 2020.

ARIASETA, A. et al. Characterization of Recrystallization and Second-Phase Particles in Solution-Treated Additively Manufactured Alloy 718. **Metallurgical and Materials Transactions A: Physical Metallurgy and Materials Science**, v. 51, n. 2, p. 973–981, 2020.

BADDOO, N. R. Stainless steel in construction: A review of research, applications, challenges and opportunities. **Journal of Constructional Steel Research**, v. 64, n. 11, p. 1199–1206, 2008.

BAHL, S. et al. Non-equilibrium microstructure, crystallographic texture and morphological texture synergistically result in unusual mechanical properties of 3D printed 316L stainless steel. **Additive Manufacturing**, v. 28, n. December 2018, p. 65–77, 2019.

BAI, Y. et al. Influence mechanism of parameters process and mechanical

properties evolution mechanism of maraging steel 300 by selective laser melting. **Materials Science and Engineering A**, v. 703, n. June, p. 116–123, 2017.

BARTLETT, J. L. et al. Revealing mechanisms of residual stress development in additive manufacturing via digital image correlation. **Additive Manufacturing**, v. 22, n. April, p. 1–12, 2018.

BARTLETT, J. L.; LI, X. An overview of residual stresses in metal powder bed fusion. **Additive Manufacturing**, v. 27, n. January, p. 131–149, 2019.

BEDNARCZYK, W. et al. Abnormal grain growth in a Zn-0.8Ag alloy after processing by high-pressure torsion. **Acta Materialia**, v. 207, p. 116667, 2021.

BENNETT, T. A.; KALU, P. N.; ROLLETT, A. D. On the character of host-island grain interfaces in Fe-1%Si alloy. **Scripta Materialia**, v. 57, n. 1, p. 41–44, 2007.

BERTSCH, K. M. et al. Origin of dislocation structures in an additively manufactured austenitic stainless steel 316L. **Acta Materialia**, v. 199, p. 19–33, 2020.

BEYERLEIN, I. J.; MCCABE, R. J.; TOME, C. N. Effect of microstructure on the nucleation of deformation twins in polycrystalline high-purity magnesium: A multi-scale modeling study. **Journal of the Mechanics and Physics of Solids**, v. 59, p. 988–1003, 2011.

BIDARE, P. et al. Fluid and particle dynamics in laser powder bed fusion. **Acta Materialia**, v. 142, p. 107–120, 2018.

BIRNBAUM, A. J. et al. Intrinsic strain aging, $\Sigma 3$ boundaries, and origins of cellular substructure in additively manufactured 316L. **Additive Manufacturing**, v. 29, n. June, p. 100784, 2019.

BISWAS, A. et al. Influence of Microstructural Features on the Strain Hardening Behavior of Additively Manufactured Metallic Components. **Advanced Engineering Materials**, v. 21, n. 7, p. 1–15, 2019.

BLINN, B. et al. An investigation of the microstructure and fatigue behavior of additively manufactured AISI 316L stainless steel with regard to the influence of heat treatment. **Metals**, v. 8, n. 4, 2018.

BOES, J. et al. Processing of gas-nitrided AISI 316L steel powder by laser powder bed fusion – Microstructure and properties. **Additive Manufacturing**, v. 30, n. June, p. 100836, 2019.

BRITTON, T. B.; WILKINSON, A. J. High resolution electron backscatter diffraction measurements of elastic strain variations in the presence of larger lattice rotations. **Ultramicroscopy**, v. 114, p. 82–95, 2012.

CARLTON, H. D. et al. Damage evolution and failure mechanisms in additively manufactured stainless steel. **Materials Science and Engineering A**, v. 651, p. 406–414, 2016.

CARTER, L. N. et al. Process optimisation of selective laser melting using energy density model for nickel based superalloys. **Materials Science and Technology**, v. 0836, n. October 2017, p. 1–5, 2016.

CASATI, R.; LEMKE, J.; VEDANI, M. Microstructure and Fracture Behavior of 316L Austenitic Stainless Steel Produced by Selective Laser Melting. **Journal of Materials Science and Technology**, v. 32, n. 8, p. 738–744, 2016.

CHAUVET, E. et al. Hot cracking mechanism affecting a non-weldable Ni-based superalloy produced by selective electron Beam Melting. **Acta Materialia**, v. 142, p. 82–94, 2018.

CHEN, H. et al. Powder-spreading mechanisms in powder-bed-based additive manufacturing: Experiments and computational modeling. **Acta Materialia**, v. 179, p. 158–171, 2019a.

CHEN, N. et al. Enhancement of an additive-manufactured austenitic stainless steel by post-manufacture heat-treatment. **Materials Science and Engineering A**, v. 759, n. January, p. 65–69, 2019b.

CHEN, W. et al. Microscale residual stresses in additively manufactured stainless steel. **Nature Communications**, v. 10, n. 1, p. 1–12, 2019c.

CHEN, Y. et al. Dendritic microstructure and hot cracking of laser additive manufactured Inconel 718 under improved base cooling. **Journal of Alloys and**

Compounds, v. 670, p. 312–321, 2016.

CHERRY, J. A. et al. Investigation into the effect of process parameters on microstructural and physical properties of 316L stainless steel parts by selective laser melting. **International Journal of Advanced Manufacturing Technology**, v. 76, n. 5–8, p. 869–879, 2014.

CHOI, J. S.; YOON, D. Y. The temperature dependence of abnormal grain growth and grain boundary faceting in 316L stainless steel. **ISIJ International**, v. 41, n. 5, p. 478–483, 2001.

CHOO, H. et al. Effect of laser power on defect, texture, and microstructure of a laser powder bed fusion processed 316L stainless steel. **Materials and Design**, v. 164, p. 107534, 2019.

CHOWDHURY, S. G. et al. Twinning-induced sluggish evolution of texture during recrystallization in AISI 316L stainless steel after cold rolling. **Metallurgical and Materials Transactions A: Physical Metallurgy and Materials Science**, v. 37, n. 8, p. 2349–2359, 2006.

CHOWDHURY, S. G.; DAS, S.; DE, P. K. Cold rolling behaviour and textural evolution in AISI 316L austenitic stainless steel. **Acta Materialia**, v. 53, n. 14, p. 3951–3959, 2005.

CIZEK, P. et al. EBSD and TEM investigation of the hot deformation substructure characteristics of a type 316L austenitic stainless steel. **Journal of Microscopy**, v. 213, n. 3, p. 285–295, 2004.

COLLINS, P. C. et al. Microstructural Control of Additively Manufactured Metallic Materials. **Annual Review of Materials Research**, v. 46, n. 1, p. 63–91, 2016.

DAI, D. et al. Influence of scan strategy and molten pool configuration on microstructures and tensile properties of selective laser melting additive manufactured aluminum based parts. **Optics and Laser Technology**, v. 99, p. 91–100, 2018.

DAS, S. K. et al. Grain boundary diffusion of Al in Mg. **Scripta Materialia**, v. 80, p.

41–44, 2014.

DE LUCA, A. et al. Microstructure and defects in a Ni-Cr-Al-Ti γ/γ' model superalloy processed by laser powder bed fusion. **Materials & Design**, v. 201, p. 109531, 2021.

DEBROY, T. et al. Additive manufacturing of metallic components – Process, structure and properties. **Progress in Materials Science**, v. 92, p. 112–224, 2018.

DECOST, B. L.; HOLM, E. A. Phenomenology of Abnormal Grain Growth in Systems with Nonuniform Grain Boundary Mobility. **Metallurgical and Materials Transactions A: Physical Metallurgy and Materials Science**, v. 48, n. 6, p. 2771–2780, 2017.

DEHOFF, R. R. et al. Site specific control of crystallographic grain orientation through electron beam additive manufacturing. **Materials Science and Technology**, v. 31, n. 8, p. 931–938, 2015.

DILLAMORE, I. L.; KATOH, H. The Mechanisms of Recrystallization in Cubic Metals with Particular Reference to Their Orientation-Dependence. **Metal Science**, v. 8, n. 1, p. 73–83, 1974.

EL-DANAF, E. et al. Deformation texture transition in brass: critical role of micro-scale shear bands. **Acta Materialia**, v. 48, n. 10, p. 2665–2673, 2000.

EL-DANAF, E.; KALIDINDI, S. R.; DOHERTY, R. D. Influence of grain size and stacking-fault energy on deformation twinning in fcc metals. **Metallurgical and Materials Transactions A: Physical Metallurgy and Materials Science**, v. 30, n. 5, p. 1223–1233, 1999.

ENGELI, R. et al. Processability of different IN738LC powder batches by selective laser melting. **Journal of Materials Processing Technology**, v. 229, p. 484–491, 2016.

ENGLER, O. On the influence of orientation pinning on growth selection of recrystallisation. **Acta Materialia**, v. 46, n. 5, p. 1555–1568, 1998.

FIELD, D. P. et al. The role of annealing twins during recrystallization of Cu. **Acta**

Materialia, v. 55, n. 12, p. 4233–4241, 2007.

GANERIWALA, R. K. et al. Evaluation of a thermomechanical model for prediction of residual stress during laser powder bed fusion of Ti-6Al-4V. **Additive Manufacturing**, v. 27, n. December 2018, p. 489–502, 2019.

GAO, S. et al. Recrystallization-based grain boundary engineering of 316L stainless steel produced via selective laser melting. **Acta Materialia**, v. 200, p. 366–377, 2020.

GE, C. et al. Progress of Research on P/M and Spray-Formed Superalloy in ISCPM, USTB. In: **Superalloys 2012**. [s.l: s.n.]. p. 557–562.

GIBSON, I.; ROSEN, D.; STUCKER, B. **Additive Manufacturing Technologies**. 2 edition ed. New York: Springer-Verlag, 2015.

GRAY, G. T. et al. Structure/property (constitutive and spallation response) of additively manufactured 316L stainless steel. **Acta Materialia**, v. 138, p. 140–149, 2017.

GRIGORIEV, A. et al. In-situ synthesis of Ti₂AlNb-based intermetallic alloy by selective laser melting. **Journal of Alloys and Compounds**, v. 704, p. 434–442, 2017.

GU, D. D. et al. Laser additive manufacturing of metallic components: materials, processes and mechanisms. **International Materials Reviews**, v. 57, n. 3, p. 133–164, 2012.

GUPTA, R. K.; BIRBILIS, N. The influence of nanocrystalline structure and processing route on corrosion of stainless steel: A review. **Corrosion Science**, v. 92, p. 1–15, 2015.

GUSAROV, A. V. et al. Model of Radiation and Heat Transfer in Laser-Powder Interaction Zone at Selective Laser Melting. **Journal of Heat Transfer**, v. 131, n. 7, p. 072101, 2009.

GUSAROV, A. V.; KRUTH, J. P. Modelling of radiation transfer in metallic powders at laser treatment. **International Journal of Heat and Mass Transfer**, v. 48, n. 16,

p. 3423–3434, 2005.

HAASE, C. et al. Applying the texture analysis for optimizing thermomechanical treatment of high manganese twinning-induced plasticity steel. **Acta Materialia**, v. 80, p. 327–340, 2014.

HAASE, C.; BARRALES-MORA, L. A. Influence of deformation and annealing twinning on the microstructure and texture evolution of face-centered cubic high-entropy alloys. **Acta Materialia**, v. 150, p. 88–103, 2018.

HAN, J.; VITEK, V.; SROLOVITZ, D. J. Grain-boundary metastability and its statistical properties. **Acta Materialia**, v. 104, p. 259–273, 2016.

HANSEN, N. Polycrystalline strengthening. **Metallurgical Transactions A**, v. 16, n. 12, p. 2167–2190, 1985.

HANSEN, N. Cold deformation microstructures. **Materials Science and Technology (United Kingdom)**, v. 6, n. 11, p. 1039–1047, 1990.

HAYAKAWA, Y.; SZPUNAR, J. A. The role of grain boundary character distribution in secondary recrystallization of electrical steels. **Acta Materialia**, v. 45, n. 3, p. 1285–1295, 1997.

HAYES, B. J. et al. Invited review: Genomic selection in dairy cattle: Progress and challenges. **Journal of Dairy Science**, v. 92, n. 2, p. 433–443, 2009.

HEELING, T.; CLOOTS, M.; WEGENER, K. Melt pool simulation for the evaluation of process parameters in selective laser melting. **Additive Manufacturing**, v. 14, p. 116–125, 2017.

HERZOG, D. et al. Additive manufacturing of metals. **Acta Materialia**, v. 117, p. 371–392, 2016.

HILLERT, M. On the theory of normal and abnormal grain growth. **Acta Metallurgica**, v. 13, n. 3, p. 227–238, 1965.

HIRSCH, J.; LÜCKE, K.; HATHERLY, M. Overview No. 76. Mechanism of deformation and development of rolling textures in polycrystalline f.c.c. Metals-III.

The influence of slip inhomogeneities and twinning. **Acta Metallurgica**, v. 36, n. 11, p. 2905–2927, 1988.

HOLM, E. A.; FOILES, S. M. How grain growth stops: A mechanism for grain-growth stagnation in pure materials. **Science**, v. 328, n. 5982, p. 1138–1141, 2010.

HONG, Y. et al. The cellular boundary with high density of dislocations governed the strengthening mechanism in selective laser melted 316L stainless steel. **Materials Science and Engineering A**, v. 799, n. May 2020, p. 140279, 2021.

HUA, T. et al. Microstructure and Mechanical Properties of Laser Solid Formed Ti-6Al-4V from Blended Elemental Powders. **Rare Metal Materials and Engineering**, v. 38, n. 4, p. 574–578, 2009.

HUGHES, D. A.; HANSEN, N. High angle boundaries formed by grain subdivision mechanisms. **Acta Materialia**, v. 45, n. 9, p. 3871–3886, 1997.

HUGHES, D. A.; HANSEN, N.; BAMMANN, D. J. Geometrically necessary boundaries, incidental dislocation boundaries and geometrically necessary dislocations. **Scripta Materialia**, v. 48, n. 2, p. 147–153, 2003.

HUMPHREYS, F. J.; ARDAKANI, M. G. Grain boundary migration and zener pinning in particle-containing copper crystals. **Acta Materialia**, v. 44, n. 7, p. 2717–2727, 1996.

HUMPHREYS, F. J.; HATHERLY, M. **Recrystallization and Related Annealing phenomena**. [s.l.] Elsevier Ltd, 2004a.

HUMPHREYS, F. J.; HATHERLY, M. **Recrystallization and Related Annealing Phenomena**. 2nd. ed. Pittsburgh, USA: Elsevier, 2004b.

HUTCHINSON, W. B. Recrystallisation textures in iron resulting from nucleation at grain boundaries. **Acta Metallurgica**, v. 37, n. 4, p. 1047–1056, 1989.

JÄGLE, E. A.; MITTEMEIJER, E. J. The kinetics of grain-boundary nucleated phase transformations: Simulations and modelling. **Acta Materialia**, v. 59, n. 14, p. 5775–5786, 2011.

JIANG, J.; BRITTON, T. B.; WILKINSON, A. J. Measurement of geometrically necessary dislocation density with high resolution electron backscatter diffraction: Effects of detector binning and step size. **Ultramicroscopy**, v. 125, p. 1–9, 2013.

JUNG, S. H.; KANG, S. J. L. Repetitive grain growth behavior with increasing temperature and grain boundary roughening in a model nickel system. **Acta Materialia**, v. 69, p. 283–291, 2014.

JUUL JENSEN, D. Growth rates and misorientation relationships between growing nuclei/grains and the surrounding deformed matrix during recrystallization. **Acta Metallurgica Et Materialia**, v. 43, n. 11, p. 4117–4129, 1995.

KARLSSON, J. et al. Characterization and comparison of materials produced by Electron Beam Melting (EBM) of two different Ti-6Al-4V powder fractions. **Journal of Materials Processing Technology**, v. 213, n. 12, p. 2109–2118, 2013.

KHAIRALLAH, S. A. et al. Laser powder-bed fusion additive manufacturing: Physics of complex melt flow and formation mechanisms of pores, spatter, and denudation zones. **Acta Materialia**, v. 108, p. 36–45, 2016.

KHAIRALLAH, S. A.; ANDERSON, A. Mesoscopic simulation model of selective laser melting of stainless steel powder. **Journal of Materials Processing Technology**, v. 214, n. 11, p. 2627–2636, 2014.

KIM, S. G.; PARK, Y. B. Grain boundary segregation, solute drag and abnormal grain growth. **Acta Materialia**, v. 56, n. 15, p. 3739–3753, 2008.

KONG, D. et al. Heat treatment effect on the microstructure and corrosion behavior of 316L stainless steel fabricated by selective laser melting for proton exchange membrane fuel cells. **Electrochimica Acta**, v. 276, p. 293–303, 2018.

KRAKHMALIEV, P. et al. Microstructure, solidification texture, and thermal stability of 316 L stainless steel manufactured by laser powder bed fusion. **Metals**, v. 8, n. 8, 2018.

KRUTH, J.-P. et al. Assessing and comparing influencing factors of residual stresses in selective laser melting using a novel analysis method. **Proceedings of**

the Institution of Mechanical Engineers, Part B: Journal of Engineering Manufacture, v. 226, n. 6, p. 980–991, 2012.

KRUTH, J. P. et al. Selective laser melting of iron-based powder. **Journal of Materials Processing Technology**, v. 149, n. 1–3, p. 616–622, 2004.

KUHLMANN-WILSDORF, D. Overview No. 131: “regular” deformation bands (DBs) and the leds hypothesis. **Acta Materialia**, v. 47, n. 6, p. 1697–1712, 1999a.

KUHLMANN-WILSDORF, D. Deformation bands, the LEDS theory, and their importance in texture development: Part I. Previous evidence and new observations. **Metallurgical and Materials Transactions A: Physical Metallurgy and Materials Science**, v. 30, n. 9, p. 2391–2401, 1999b.

KUHLMANN-WILSDORF, D.; HANSEN, N. Geometrically necessary, incidental and subgrain boundaries. **Scripta Metallurgica et Materialia**, v. 25, n. 7, p. 1557–1562, 1991.

KUMAR, M.; SCHWARTZ, A. J.; KING, W. E. Microstructural evolution during grain boundary engineering of low to medium stacking fault energy fcc materials. **Acta Materialia**, v. 50, n. 10, p. 2599–2612, 2002.

KÜRNSTEINER, P. et al. Massive nanoprecipitation in an Fe-19Ni-xAl maraging steel triggered by the intrinsic heat treatment during laser metal deposition. **Acta Materialia**, v. 129, p. 52–60, 2017.

LALEH, M. et al. On the unusual intergranular corrosion resistance of 316L stainless steel additively manufactured by selective laser melting. **Corrosion Science**, v. 161, n. August, p. 108189, 2019.

LE GALL, R.; JONAS, J. J. Solute drag effects during the dynamic recrystallization of nickel. **Acta Materialia**, v. 47, n. 17, p. 4365–4374, 1999.

LEE, D. N. The evolution of recrystallization textures from deformation textures. **Scripta Metallurgica et Materialia**, v. 32, n. 10, p. 1689–1694, 1995.

LEUNG, C. L. A. et al. The effect of powder oxidation on defect formation in laser additive manufacturing. **Acta Materialia**, v. 166, p. 294–305, 2019.

LI, J. et al. Fine-grain-embedded dislocation-cell structures for high strength and ductility in additively manufactured steels. **Materials Science and Engineering A**, v. 790, n. June, p. 139736, 2020.

LI, Z.; HE, B.; GUO, Q. Strengthening and hardening mechanisms of additively manufactured stainless steels: The role of cell sizes. **Scripta Materialia**, v. 177, p. 17–21, 2020.

LIN, D. et al. A strong, ductile, high-entropy FeCoCrNi alloy with fine grains fabricated via additive manufacturing and a single cold deformation and annealing cycle. **Additive Manufacturing**, v. 36, n. August, p. 101591, 2020a.

LIN, F. et al. Importance of Non-uniform Boundary Migration for Recrystallization Kinetics. **Metallurgical and Materials Transactions A: Physical Metallurgy and Materials Science**, v. 49, n. 11, p. 5246–5258, 2018.

LIN, W. C. et al. Microstructure and tensile property of a precipitation strengthened high entropy alloy processed by selective laser melting and post heat treatment. **Additive Manufacturing**, v. 36, 2020b.

LIU, P. et al. Insight into the mechanisms of columnar to equiaxed grain transition during metallic additive manufacturing. **Additive Manufacturing**, v. 26, n. December 2018, p. 22–29, 2019.

LIU, Y.; MILITZER, M.; PEREZ, M. Phase Field Modelling of Abnormal Grain Growth. **Materials**, v. 12, p. 4048–4068, 2019a.

LIU, Y.; MILITZER, M.; PEREZ, M. Phase field modelling of abnormal grain growth. **Materials**, v. 12, n. 24, 2019b.

LIVERANI, E. et al. Effect of selective laser melting (SLM) process parameters on microstructure and mechanical properties of 316L austenitic stainless steel. **Journal of Materials Processing Technology**, v. 249, n. June, p. 255–263, 2017.

LO, K. H.; SHEK, C. H.; LAI, J. K. L. Recent developments in stainless steels. v. 65, p. 39–104, 2009.

LOU, X.; ANDRESEN, P. L.; REBAK, R. B. Oxide inclusions in laser additive

manufactured stainless steel and their effects on impact toughness and stress corrosion cracking behavior. **Journal of Nuclear Materials**, v. 499, p. 182–190, 2018.

LU, N. et al. Dynamics of particle-assisted abnormal grain growth revealed through integrated three-dimensional microanalysis. **Acta Materialia**, v. 195, p. 1–12, 2020.

LUTTEROTTI, L. **MAUD, version 2.038**.

LUTTEROTTI, L.; SCARDI, P. Simultaneous structure and size-strain refinement by the Rietveld method. **Journal of Applied Crystallography**, v. 23, n. 4, p. 246–252, 1990.

LY, S. et al. Metal vapor micro-jet controls material redistribution in laser powder bed fusion additive manufacturing. **Scientific Reports**, v. 7, n. 1, p. 1–12, 2017.

MACKENZIE, B. Y. J. K. SECOND PAPER ON STATISTICS ASSOCIATED WITH THE RANDOM DISORIENTATION OF CUBES. p. 229–240, 1957.

MAJUMDAR, J. D. et al. Microstructure characterisation and process optimization of laser assisted rapid fabrication of 316L stainless steel. **Applied Surface Science**, v. 247, n. 1–4, p. 320–327, 2005.

MARÉCHAL, D. Linkage between mechanical properties and phase transformations in a 301LN austenitic stainless steel. n. April, p. 228, 2011.

MARTIN, J. H. et al. 3D printing of high-strength aluminium alloys. **Nature**, v. 549, n. 7672, p. 365–369, 2017.

MEYERS, M. A. et al. Microstructural evolution in adiabatic shear localization in stainless steel. **Acta Materialia**, v. 51, n. 5, p. 1307–1325, 2003.

MEYERS, M. A.; MURR, L. E. A model for the formation of annealing twins in F.C.C. metals and alloys. **Acta Metallurgica**, v. 26, n. 6, p. 951–962, 1978.

MIRKOOHI, E. et al. Microstructure affected residual stress prediction based on mechanical threshold stress in direct metal deposition of Ti-6Al-4 V. **International Journal of Advanced Manufacturing Technology**, v. 112, n. 5–6, p. 1705–1712,

2021.

MISHRA, S.; NARASIMHAN, K.; SAMAJDAR, I. Deformation twinning in AISI 316L austenitic stainless steel: Role of strain and strain path. **Materials Science and Technology**, v. 23, n. 9, p. 1118–1126, 2007.

MISHUROVA, T. et al. An assessment of subsurface residual stress analysis in SLM Ti-6Al-4V. **Materials**, v. 10, n. 4, 2017.

MISHUROVA, T. et al. Exploring the correlation between subsurface residual stresses and manufacturing parameters in laser powder bed fused ti-6al-4v. **Metals**, v. 9, n. 2, 2019.

MOHAMED, G.; BACROIX, B. Role of stored energy in static recrystallization of cold rolled copper single and multicrystals. **Acta Materialia**, v. 48, n. 13, p. 3295–3302, 2000.

MOHAMMED, A. A. S.; EL-DANAF, E. A.; RADWAN, A. A. A criterion for shear banding localization in polycrystalline FCC metals and alloys and critical working conditions for different microstructural variables. **Journal of Materials Processing Technology**, v. 186, p. 14–21, 2007.

MONTEIRO, S. N. et al. Novel methods for dislocation density estimation in highly compacted tangles. **Journal of Materials Research and Technology**, v. 9, n. 2, p. 2072–2078, 2020.

MONTERO-SISTIAGA, M. L. et al. Microstructure evolution of 316L produced by HP-SLM (high power selective laser melting). **Additive Manufacturing**, v. 23, n. August, p. 402–410, 2018.

MORGAN, R.; SUTCLIFFE, C. J.; O'NEILL, W. Density analysis of direct metal laser re-melted 316L stainless steel cubic primitives. **Journal of Materials Science**, v. 39, n. 4, p. 1195–1205, 2004.

MOWER, T. M.; LONG, M. J. Mechanical behavior of additive manufactured, powder-bed laser-fused materials. **Materials Science and Engineering A**, v. 651, p. 198–213, 2016.

MUGHRABI, H. On the role of strain gradients and long-range internal stresses in the composite model of crystal plasticity. **Materials Science and Engineering A**, v. 317, n. 1–2, p. 171–180, 2001.

MUGHRABI, H. Dual role of deformation-induced geometrically necessary dislocations with respect to lattice plane misorientations and/or long-range internal stresses. **Acta Materialia**, v. 54, n. 13, p. 3417–3427, 2006.

MUGWAGWA, L. et al. Evaluation of the impact of scanning strategies on residual stresses in selective laser melting. **International Journal of Advanced Manufacturing Technology**, v. 102, n. 5–8, p. 2441–2450, 2019.

NADAMMAL, N. et al. Effect of hatch length on the development of microstructure, texture and residual stresses in selective laser melted superalloy Inconel 718. **Materials and Design**, v. 134, p. 139–150, 2017.

NES, E.; RYUM, N.; HUNDERI, O. On the Zener Drag. **Acta Materialia**, v. 33, n. 1, p. 11–22, 1985.

NEZAKAT, M. et al. Effect of thermo-mechanical processing on texture evolution in austenitic stainless steel 316L. **Materials Characterization**, v. 98, p. 10–17, 2014.

NIENDORF, T. et al. Highly anisotropic steel processed by selective laser melting. **Metallurgical and Materials Transactions B: Process Metallurgy and Materials Processing Science**, v. 44, n. 4, p. 794–796, 2013.

ODNOBOKOVA, M. et al. Annealing behavior of a 304L stainless steel processed by large strain cold and warm rolling. **Materials Science & Engineering A**, v. 689, n. October 2016, p. 370–383, 2017.

ODNOBOKOVA, M.; BELYAKOV, A.; KAIBYSHEV, R. Effect of Severe Cold or Warm Deformation on Microstructure Evolution and Tensile Behavior of a 316L Stainless Steel. **Advanced Engineering Materials**, v. 17, n. 12, p. 1812–1820, 2015.

OLMSTED, D. L.; FOILES, S. M.; HOLM, E. A. Survey of computed grain boundary properties in face-centered cubic metals: I. Grain boundary energy. **Acta Materialia**,

v. 57, n. 13, p. 3694–3703, 2009.

OLMSTED, D. L.; HOLM, E. A.; FOILES, S. M. Survey of computed grain boundary properties in face-centered cubic metals-II: Grain boundary mobility. **Acta Materialia**, v. 57, n. 13, p. 3704–3713, 2009.

PACE, M. L. et al. 3D additive manufactured 316L components microstructural features and changes induced by working life cycles. **Applied Surface Science**, v. 418, p. 437–445, 2017.

PADILHA, A. F. AÇOS : PERSPECTIVAS PARA OS PRÓXIMOS 10 ANOS. In: **Aços inoxidáveis: histórico e desenvolvimento**. [s.l: s.n.]. p. 129–138.

PADILHA, A. F.; PLAUT, R. L.; RIOS, P. R. Annealing of cold-worked austenitic stainless steels. **ISIJ International**, v. 43, n. 2, p. 135–143, 2003.

PADILHA, A. F.; RIOS, P. R. Decomposition of austenite in austenitic stainless steels. **ISIJ International**, v. 42, n. 4, p. 325–337, 2002.

PARRY, L. A.; ASHCROFT, I. A.; WILDMAN, R. D. Geometrical effects on residual stress in selective laser melting. **Additive Manufacturing**, v. 25, n. June 2018, p. 166–175, 2019.

PARRY, L.; ASHCROFT, I. A.; WILDMAN, R. D. Understanding the effect of laser scan strategy on residual stress in selective laser melting through thermo-mechanical simulation. **Additive Manufacturing**, v. 12, p. 1–15, 2016.

PAULY, S. et al. Experimental determination of cooling rates in selectively laser-melted eutectic Al-33Cu. **Additive Manufacturing**, v. 22, n. February, p. 753–757, 2018.

PENG, H. et al. Role of Annealing in Improving Shape Memory Effect of As-Cast Fe-Mn-Si-Cr-Ni Shape Memory Alloys. **Metallurgical and Materials Transactions A**, v. 50, n. 7, p. 3070–3079, 2019.

PHAM, M. S. et al. The role of side-branching in microstructure development in laser powder-bed fusion. **Nature Communications**, v. 11, n. 1, p. 1–12, 2020.

PHAM, M. S.; DOVGYY, B.; HOOPER, P. A. Twinning induced plasticity in austenitic stainless steel 316L made by additive manufacturing. **Materials Science and Engineering A**, v. 704, n. July, p. 102–111, 2017.

PHILIPPE, T.; VOORHEES, P. W. Ostwald ripening in multicomponent alloys. **Acta Materialia**, v. 61, n. 11, p. 4237–4244, 2013.

PINTO, F. C. **Avaliação da estabilidade microestrutural do aço inoxidável austenítico 316L processado por fusão seletiva a laser**. [s.l.] Universidade de São Paulo, 2019.

PINTO, F. C. et al. Defects in parts manufactured by selective laser melting caused by δ -ferrite in reused 316L steel powder feedstock. **Additive Manufacturing**, v. 31, n. June 2019, p. 100979, 2020.

POLONSKY, A. T. et al. Solidification-driven orientation gradients in additively manufactured stainless steel. **Acta Materialia**, v. 183, p. 249–260, 2020.

POPA, N. C. The (hkl) Dependence of Diffraction-Line Broadening Caused by Strain and Size for all Laue Groups in Rietveld Refinement. **Journal of Applied Crystallography**, v. 31, n. 2, p. 176–180, abr. 1998.

RAHIMI, R. et al. Influence of Al on the temperature dependence of strain hardening behavior and glide planarity in Fe-Cr-Ni-Mn-C austenitic stainless steels. **Materials Science and Engineering A**, v. 649, p. 301–312, 2016.

RANDLE, V. Mechanism of twinning-induced grain boundary engineering in low stacking-fault energy materials. **Acta Materialia**, v. 47, n. 15, p. 4187–4196, 1999.

RANDLE, V. The coincidence site lattice and the “sigma enigma”. **Materials Characterization**, v. 47, n. 5, p. 411–416, 2001.

RANDLE, V. “Special” boundaries and grain boundary plane engineering. **Scripta Materialia**, v. 54, n. 6, p. 1011–1015, 2006a.

RANDLE, V. “Five-parameter” analysis of grain boundary networks by electron backscatter diffraction. **Journal of Microscopy**, v. 222, n. 2, p. 69–75, 2006b.

RAVI KUMAR, B. et al. Comparison of rolling texture in low and medium stacking fault energy austenitic stainless steels. **Materials Science and Engineering A**, v. 394, n. 1–2, p. 296–301, 2005.

RIDHA, A. A.; HUTCHINSON, W. B. Recrystallisation mechanisms and the origin of cube texture in copper. **Acta Metallurgica**, v. 30, n. 10, p. 1929–1939, 1982.

RIEMER, A. et al. On the fatigue crack growth behavior in 316L stainless steel manufactured by selective laser melting. **Engineering Fracture Mechanics**, v. 120, p. 15–25, 2014.

RIOS, P. R. et al. Analytical expression for the evolution of interfacial area density between transformed grains during nucleation and growth transformations. **Scripta Materialia**, v. 54, n. 8, p. 1509–1513, 2006.

RIOS, P. R.; GOTTSTEIN, G. Texture evolution during normal and abnormal grain growth in an Al-1 wt% Mn alloy. **Acta Materialia**, v. 49, n. 13, p. 2511–2518, 2001.

ROBINSON, J. et al. Determination of the effect of scan strategy on residual stress in laser powder bed fusion additive manufacturing. **Additive Manufacturing**, v. 23, n. June, p. 13–24, 2018.

RODGERS, T. M.; MADISON, J. D.; TIKARE, V. Simulation of metal additive manufacturing microstructures using kinetic Monte Carlo. **Computational Materials Science**, v. 135, p. 78–89, 2017.

ROMANO, J. et al. Temperature distribution and melt geometry in laser and electron-beam melting processes - A comparison among common materials. **Additive Manufacturing**, v. 8, p. 1–11, 2015.

SABZI, H. E. et al. Grain refinement in laser powder bed fusion: The influence of dynamic recrystallization and recovery. **Materials and Design**, v. 196, 2020.

SAEDI, S. et al. On the effects of selective laser melting process parameters on microstructure and thermomechanical response of Ni-rich NiTi. **Acta Materialia**, v. 144, p. 552–560, 2018.

SAEIDI, K. et al. Hardened austenite steel with columnar sub-grain structure formed

by laser melting. **Materials Science and Engineering A**, v. 625, p. 221–229, 2015a.

SAEIDI, K. et al. Austenitic stainless steel strengthened by the in situ formation of oxide nanoinclusions. **RSC Adv.**, v. 5, n. 27, p. 20747–20750, 2015b.

SAITO, G. et al. In-situ observation of abnormal grain growth in a low-alloyed carbon steel using SEM-EBSD. **Materialia**, v. 15, n. September 2020, p. 100985, 2021.

SALAMA, H. et al. Role of inclination dependence of grain boundary energy on the microstructure evolution during grain growth. **Acta Materialia**, v. 188, p. 641–651, 2020.

SALLEZ, N. et al. In situ characterization of microstructural instabilities: Recovery, recrystallization and abnormal growth in nanoreinforced steel powder. **Acta Materialia**, v. 87, p. 377–389, 2015.

SALMAN, O. O. et al. Impact of the scanning strategy on the mechanical behavior of 316L steel synthesized by selective laser melting. **Journal of Manufacturing Processes**, v. 45, n. June, p. 255–261, 2019.

SCIPIONI BERTOLI, U. et al. On the limitations of Volumetric Energy Density as a design parameter for Selective Laser Melting. **Materials and Design**, v. 113, p. 331–340, 2017.

SERRANO-MUNOZ, I. et al. On the interplay of microstructure and residual stress in LPBF IN718. **Journal of Materials Science**, p. 5845–5867, 2020a.

SERRANO-MUNOZ, I. et al. The residual stress in as-built Laser Powder Bed Fusion IN718 alloy as a consequence of the scanning strategy induced microstructure. **Scientific Reports**, v. 10, n. 1, p. 1–15, 2020b.

SHEN, R. R.; EFSING, P. Overcoming the drawbacks of plastic strain estimation based on KAM. **Ultramicroscopy**, v. 184, p. 156–163, 2018.

SIMONELLI, M. et al. A Study on the Laser Spatter and the Oxidation Reactions During Selective Laser Melting of 316L Stainless Steel, Al-Si10-Mg, and Ti-6Al-4V. **Metallurgical and Materials Transactions A: Physical Metallurgy and Materials**

Science, v. 46, n. 9, p. 3842–3851, 2015.

SIMSON, T. et al. Residual stress measurements on AISI 316L samples manufactured by selective laser melting. **Additive Manufacturing**, v. 17, p. 183–189, 2017.

SMITH, T. R. et al. Strengthening mechanisms in directed energy deposited austenitic stainless steel. **Acta Materialia**, v. 164, p. 728–740, 2019.

SOUZA FILHO, I. R. et al. Strain hardening mechanisms during cold rolling of a high-Mn steel: Interplay between submicron defects and microtexture. **Materials Science and Engineering A**, v. 754, n. February, p. 636–649, 2019.

SPIERINGS, A. B.; LEVY, G. Comparison of density of stainless steel 316L parts produced with selective laser melting using different powder grades. **Solid Freeform Fabrication Proceedings**, n. January 2009, p. 342–353, 2009.

SPIESS, L. et al. **Moderne Röntgenbeugung**. 2. ed. [s.l.] Vieweg+Teubner, 2009.

STEINMETZ, D. R. et al. Revealing the strain-hardening behavior of twinning-induced plasticity steels: Theory, simulations, experiments. **Acta Materialia**, v. 61, n. 2, p. 494–510, 2013.

STRANTZA, M. et al. Directional and oscillating residual stress on the mesoscale in additively manufactured Ti-6Al-4V. **Acta Materialia**, v. 168, p. 299–308, 2019.

STRAUMAL, B. B. et al. Review: grain boundary faceting–roughening phenomena. **Journal of Materials Science**, v. 51, n. 1, p. 382–404, 2015.

SUN, S. H. et al. Excellent mechanical and corrosion properties of austenitic stainless steel with a unique crystallographic lamellar microstructure via selective laser melting. **Scripta Materialia**, v. 159, p. 89–93, 2019a.

SUN, S. H.; HAGIHARA, K.; NAKANO, T. Effect of scanning strategy on texture formation in Ni-25 at.%Mo alloys fabricated by selective laser melting. **Materials and Design**, v. 140, p. 307–316, 2018.

SUN, Z. et al. Simultaneously enhanced strength and ductility for 3D-printed

stainless steel 316L by selective laser melting. **NPG Asia Materials**, v. 10, n. 4, p. 127–136, 2018.

SUN, Z. et al. Revealing hot tearing mechanism for an additively manufactured high-entropy alloy via selective laser melting. **Scripta Materialia**, v. 168, p. 129–133, 2019b.

SUN, Z. et al. Reducing hot tearing by grain boundary segregation engineering in additive manufacturing: example of an Al_xCoCrFeNi high-entropy alloy. **Acta Materialia**, v. 204, p. 116505, 2021.

TANG, M.; PISTORIUS, P. C. Oxides, porosity and fatigue performance of AlSi10Mg parts produced by selective laser melting. **International Journal of Fatigue**, v. 94, p. 192–201, 2017.

TANG, M.; REED, B. W.; KUMAR, M. Coarsening kinetics of topologically highly correlated grain boundary networks. **Journal of Applied Physics**, v. 043505, n. March, 2012.

THIJS, L. et al. A study of the microstructural evolution during selective laser melting of Ti-6Al-4V. **Acta Materialia**, v. 58, n. 9, p. 3303–3312, 2010.

THIJS, L. et al. Strong morphological and crystallographic texture and resulting yield strength anisotropy in selective laser melted tantalum. **Acta Materialia**, v. 61, n. 12, p. 4657–4668, 2013.

ULBRICHT, A. et al. Separation of the formation mechanisms of residual stresses in lpbf 316l. **Metals**, v. 10, n. 9, p. 1–15, 2020.

VANDERMEER, R. A. Microstructural descriptors and the effects of nuclei clustering on recrystallization path kinetics. **Acta Materialia**, v. 53, n. 5, p. 1449–1457, 2005.

VANDERMEER, R. A.; JENSEN, D. J. On the estimation of cahn-hagel interface migration rates. **Scripta Metallurgica et Materiala**, v. 30, n. 12, p. 1575–1580, 1994.

VANDERMEER, R. A.; JENSEN, D. J. Quantifying recrystallization nucleation and growth kinetics of cold-worked copper by microstructural analysis. **Metallurgical**

and Materials Transactions A, v. 26, n. 9, p. 2227–2235, 1995.

VANDERMEER, R. A.; JUUL JENSEN, D. Recrystallization in hot vs cold deformed commercial aluminum: A microstructure path comparison. **Acta Materialia**, v. 51, n. 10, p. 3005–3018, 2003.

VANDERMEER, R. A.; MASUMURA, R. A. THE MICROSTRUCTURAL PATH OF GRAIN - BOUNDARY - NUCLEATED PHASE TRANSFORMATIONS. v. 40, n. 4, p. 877–886, 1992.

VANDERMEER, R. A.; MASUMURA, R. A.; RATH, B. B. Microstructural paths of shape-preserved nucleation and growth transformations. **Acta Metallurgica Et Materialia**, v. 39, n. 3, p. 383–389, 1991.

VO, N. Q. et al. Atomic mixing in metals under shear deformation. **Jom**, v. 65, n. 3, p. 382–389, 2013.

VOISIN, T. et al. New insights on cellular structures strengthening mechanisms and thermal stability of an austenitic stainless steel fabricated by laser powder-bed-fusion. **Acta Materialia**, v. 203, p. 116476, 2021.

VORA, P. et al. AlSi12 in-situ alloy formation and residual stress reduction using anchorless selective laser melting. **Additive Manufacturing**, v. 7, p. 12–19, 2015.

WANG, X. et al. Crystallographic-orientation-dependent tensile behaviours of stainless steel 316L fabricated by laser powder bed fusion. **Materials Science and Engineering A**, v. 766, n. June, p. 138395, 2019.

WANG, Y. M. et al. Additively manufactured hierarchical stainless steels with high strength and ductility. **Nature Materials**, n. October, 2017.

WANG, Z.; BEESE, A. M. Effect of chemistry on martensitic phase transformation kinetics and resulting properties of additively manufactured stainless steel. **Acta Materialia**, v. 131, p. 410–422, 2017.

WANG, Z.; PALMER, T. A.; BEESE, A. M. Effect of processing parameters on microstructure and tensile properties of austenitic stainless steel 304L made by directed energy deposition additive manufacturing. **Acta Materialia**, v. 110, p. 226–

235, 2016.

WARREN, B. E. **X-Ray diffraction**. [s.l.] Courier Corporation, 1990.

WARREN, B. E.; AVERBACH, B. L. The effect of cold-work distortion on x-ray patterns. **Journal of Applied Physics**, v. 21, n. 6, p. 595–599, 1950.

WEAVER, J. S.; LIVESCU, V.; MARA, N. A. A comparison of adiabatic shear bands in wrought and additively manufactured 316L stainless steel using nanoindentation and electron backscatter diffraction. **Journal of Materials Science**, v. 55, n. 4, p. 1738–1752, 2020.

WEI, H. L.; MAZUMDER, J.; DEBROY, T. Evolution of solidification texture during additive manufacturing. **Scientific Reports**, v. 5, p. 16446, 2015.

WELZEL, U. et al. Stress analysis of polycrystalline thin films and surface regions by X-ray diffraction. **Journal of Applied Crystallography**, v. 38, n. 1, p. 1–29, 2005.

WILLIAMSON, G. K.; SMALLMAN, R. E. III. Dislocation densities in some annealed and cold-worked metals from measurements on the X-ray Debye-Scherrer spectrum. **Philosophical Magazine**, v. 1, n. 1, p. 34–46, 1956.

WOO, W. et al. Stacking Fault Energy Analyses of Additively Manufactured Stainless Steel 316L and CrCoNi Medium Entropy Alloy Using In Situ Neutron Diffraction. **Scientific Reports**, p. 2–4, 2020.

XU, W. et al. In situ tailoring microstructure in additively manufactured Ti-6Al-4V for superior mechanical performance. **Acta Materialia**, v. 125, n. February, p. 390–400, 2017.

XUE, Q.; CERRETA, E. K.; GRAY, G. T. Microstructural characteristics of post-shear localization in cold-rolled 316L stainless steel. **Acta Materialia**, v. 55, n. 2, p. 691–704, 2007.

XUE, Q.; GRAY, I. T. Development of adiabatic shear bands in annealed 316L stainless steel: Part I. Correlation between evolving microstructure and mechanical behavior. **Metallurgical and Materials Transactions A: Physical Metallurgy and Materials Science**, v. 37, n. 8, p. 2435–2446, 2006a.

XUE, Q.; GRAY, I. T. Development of adiabatic shear bands in annealed 316L stainless steel: Part II. TEM studies of the evolution of microstructure during deformation localization. **Metallurgical and Materials Transactions A: Physical Metallurgy and Materials Science**, v. 37, n. 8, p. 2447–2458, 2006b.

XUE, Y. et al. Microporosity effects on cyclic plasticity and fatigue of LENSTM-processed steel. **Acta Materialia**, v. 58, n. 11, p. 4029–4038, 2010.

YADROITSEV, I.; YADROITSAVA, I. Evaluation of residual stress in stainless steel 316L and Ti6Al4V samples produced by selective laser melting. **Virtual and Physical Prototyping**, v. 10, n. 2, p. 67–76, 2015.

YAN, F. et al. Characterization of nano-scale oxides in austenitic stainless steel processed by powder bed fusion. **Scripta Materialia**, v. 155, p. 104–108, 2018.

YAN, F.; XIONG, W.; FAIERSON, E. Grain Structure Control of Additively Manufactured Metallic Materials. **Materials**, v. 10, n. 11, p. 1260, 2017.

YANG, C.; BAKER, I. Effect of soluble particles on microstructural evolution during directional recrystallization. **Acta Materialia**, v. 188, p. 288–301, 2020.

YANG, N. et al. Process-Structure-Property Relationships for 316L Stainless Steel Fabricated by Additive Manufacturing and Its Implication for Component Engineering. **Journal of Thermal Spray Technology**, v. 26, n. 4, p. 610–626, 2017.

YAP, C. Y. et al. Review of selective laser melting: Materials and applications. **Applied Physics Reviews**, v. 2, n. 4, 2015.

YIN, Y. J. et al. Mechanism of high yield strength and yield ratio of 316 L stainless steel by additive manufacturing. **Materials Science and Engineering A**, v. 744, n. December 2018, p. 773–777, 2019.

YU, T.; HANSEN, N.; HUANG, X. Linking recovery and recrystallization through triple junction motion in aluminum cold rolled to a large strain. **Acta Materialia**, v. 61, n. 17, p. 6577–6586, 2013.

ZHANG, J. et al. Grain boundary mobilities in polycrystals. **Acta Materialia**, v. 191, p. 211–220, 2020.

ZHANG, Y. B. et al. Three-dimensional local residual stress and orientation gradients near graphite nodules in ductile cast iron. **Acta Materialia**, v. 121, p. 173–180, 2016.

ZHAO, C. et al. Real-time monitoring of laser powder bed fusion process using high-speed X-ray imaging and diffraction. **Scientific Reports**, v. 7, n. 1, p. 1–11, 2017.

ZHONG, Y. et al. Intragranular cellular segregation network structure strengthening 316L stainless steel prepared by selective laser melting. **Journal of Nuclear Materials**, v. 470, p. 170–178, 2016.

ZHONG, Y. et al. Additive manufacturing of 316L stainless steel by electron beam melting for nuclear fusion applications. **Journal of Nuclear Materials**, v. 486, p. 234–245, 2017.

ZHOU, Z. et al. The effect of texture on the low cycle fatigue property of Inconel 718 by selective laser melting. **MATEC Web of Conferences**, v. 165, p. 0–3, 2018.

ZINOVIEVA, O. et al. Three-dimensional analysis of grain structure and texture of additively manufactured 316L austenitic stainless steel. **Additive Manufacturing**, v. 36, n. July, p. 101521, 2020.

ZÖLLNER, D.; RIOS, P. R. On the topology and size advantage of potentially abnormal grains. **Computational Materials Science**, v. 153, n. May, p. 382–391, 2018.